Journal of Solid State Electrochemistry (2023) 27:1547–1591
https://doi.org/10.1007/s10008-022-05338-0

REVIEW PAPER

The review of advances in interfacial electrochemistry in Estonia: electrochemical double layer and adsorption studies for the development of electrochemical devices

Piret Pikma[1] · Heigo Ers[1] · Liis Siinor[1] · Jinfeng Zhao[1] · Ove Oll[1] · Tavo Romann[1] · Vitali Grozovski[1] · Carolin Siimenson[1] · Mart Väärtnõu[1] · Maarja Paalo[1] · Riinu Härmas[1] · Karmen Lust[1] · Thomas Thomberg[1] · Alar Jänes[1] · Jaak Nerut[1] · Rutha Jäger[1] · Peeter Valk[1] · Indrek Kivi[1] · Martin Maide[1] · Priit Möller[1] · Rait Kanarbik[1] · Gunnar Nurk[1] · Enn Lust[1]

Received: 29 September 2022 / Revised: 8 November 2022 / Accepted: 13 November 2022 / Published online: 8 December 2022

Abstract

The electrochemistry nowadays has many faces and challenges. Although the focus has shifted from fundamental electrochemistry to applied electrochemistry, one needs to acknowledge that it is impossible to develop and design novel green energy transition devices without a comprehensive understanding of the electrochemical processes at the electrode and electrolyte interface that define the performance mechanisms. The review gives an overview of the systematic research in the field of electrochemistry in Estonia which reflects on the excellent collaboration between fundamental and applied electrochemistry.

Keywords Electrical double layer · Organic compound and ion adsorption · Porous carbon and complex oxides · Solid oxide fuel cells and polymer electrolyte fuel cells

Highlights

- Comprehensive analysis of electrical double layer structure, halide ion, and organic compound adsorption at sp-metal as well as carbon electrodes is given.
- The shape of *C vs E* curves and impedance data are characteristically affected by the sp-metal and carbon crystallographic orientation as well as porous carbon and complex oxides hierarchical porous structure.
- Similarities in capacitance and impedance values between ionic liquid, aqueous, and organic electrolytes for electrical double layer structure are demonstrated.
- Significant differences in adsorption and catalytic activity depending on anion structure, solvent dielectric constant, and electrode's porous structure and composition are revealed.
- Different carbon electrodes have been prepared and analysed using different materials and techniques along with various non-aqueous and aqueous electrolytes for the development electrical double layer capacitors.
- Pt-metal-nanoclusters activated and d-metal-nitrogen active centre–based electrocatalysts have been developed for use in PEMFC electrodes and PEM single cells.
- Enhancing the intermediate temperature SOFC cathode materials through the optimisation of materials porosity, the use of nanoscale raw powders, and the search for novel electrochemically active materials.
- Advances in the development of synthesis of complex oxide materials and novel *operando* methods for the characterisation of interfacial processes.

Extended author information available on the last page of the article

Introduction

The chemical composition and crystallographic structure of electrodes, as well as the chemical composition and dielectric characteristics of electrolytes, have a remarkable influence on the electrical double layer (EDL) characteristics, adsorption kinetics of organic compounds and ions, faradaic processes of electroreduction of oxygen, complex cations and anions, and on the fuel oxidation kinetics. The latter has been systematically studied at the University of Tartu since 1990 [1–14]. Detailed theoretical analyses and experimental results have been discussed based on previously published models [15–34].

The current results of the Tartu electrochemistry working group are based on the fundamental studies at solid drop bismuth electrodes (started in 1965) [35] and at single-crystal Bi(*hkl*) facets (started in 1974) [36, 37]. Therefore, the pioneering ideas of Grahame, Frumking, and Trasatti have been all applied for the development of fundamental electrochemistry at the University of Tartu [1–12, 20–28, 36, 37]. The role of the potential drop in the electrode surface layer, obtained by the electronic characteristics of metal or carbon electrodes, has been discussed in [11, 12, 33, 38–43]. Systematic analysis of experimental data indicates that the

electronic characteristics of the sp-metals and carbon electrodes (effective mass and concentration of effective charge carriers, dielectric constant, Fermi energy levels work function dependence of crystallographic structure and orientation, etc.) [1, 2, 9, 11, 38–43] can have a more significant role on the EDL structure (including interfacial capacitance values) and Gibbs adsorption and Gibbs free energy values than the solvent (dielectric constant, dipole moment, etc.) or anion solvation/adsorption characteristics [5–8, 13]. Additionally, the EDL structure has been simulated by density functional theory (DFT) and molecular dynamics (MD) methods [44–52].

The influence of surface roughness on the EDL characteristics [53, 54] has been analysed based on models developed by Daikin et al. [55–57]. It was demonstrated that the surface roughness values established from electrochemical impedance spectroscopy (EIS) data depend on the electrode potential (surface charge density), electrolyte concentration (Debye screening length), and temperature. In addition, the surface roughness depends on the electrode's crystallographic and electronic structure (Fermi energy differences), and the difference in work function values for different crystallographic planes exposed on the rough polycrystalline surface [1, 2, 53–57].

EDL and adsorption studies have been conducted on Bi(*hkl*), Sb(*hkl*), Cd(*hklf*), and C(0001) single-crystal electrodes [2, 9–12, 44, 45, 53, 54, 58–66], as well as on porous carbon electrodes [7, 44, 45, 53, 54, 67–85]. Gibbs adsorption and Frumkin molecular interaction coefficient values depend remarkably on the crystallographic structure of the electrode, the chemical nature of electrode metal and electronic parameters, solvent chemical composition, and organic molecule characteristics. This was explained by the different solvation energies of the metal surface, organic molecules and solvent polarisability, and electrode potential, i.e., surface charge density applied. Therefore, the electrode metallic characteristics and crystallographic structure play a critical role in the density and geometrical structure of the adsorbed molecular layers formed, i.e., calculated Gibbs adsorption values.

A detailed comparison of specific adsorption at metal Bi(*hkl*), Sb(*hkl*), and Cd(0001) electrodes, glassy carbon, highly oriented pyrolytic graphite basal plane C(0001), graphene electrodes, and micro-mesoporous (MMP) carbons with high surface area will be given [25–32]. It was found that the influence of the solvent properties on the adsorption kinetics of iodide, bromide, and chloride and Gibbs energy of adsorption can most clearly be established using simple single-crystal plane | surface-active electrolyte systems, including 1-ethyl-3-methylimidazolium tetrafluoroborate ($EMImBF_4$) with additions of 1-ethyl-3-methylimidazolium chloride (EMImCl), 1-ethyl-3-methylimidazolium bromide (EMImBr), and 1-ethyl-3-methylimidazolium iodide (EMImI). It should be noted that surface pre-treatment processes hugely influence the EDL, adsorption kinetics, and faradaic reaction kinetics.

The fundamental knowledge collected has been applied for the development of very high energy and power density electrical double layer capacitors (EDLCs) [7, 68–89] prepared by applying the sol–gel method for syntheses of very mesoporous carbons [81, 90, 91], hybrid superacpacitors (HSCs), and Li^+- and Na^+-ion batteries (LIBs and SIBs) [92–98]. It should be stressed that the porous structure (hierarchical porosity) of metal and complex oxide electrodes, but especially of the carbon electrodes, has a large influence on the limiting series capacitance (C_s), characteristic adsorption time constant (t_{char}), Gibbs adsorption and adsorption free energy, and on the power density (P) values. In order to widen the ideal polarisability region, ionic liquids (ILs) with variable chemical compositions have been studied [60–65, 99–110]. Systematic EIS studies of electrodes in aqueous and non-aqueous electrolytes, ILs and IL mixtures containing surface-inactive ions and surface-active anions and cations, and some additions of organic solvents [60, 62–65, 99–109] demonstrate a high correlation with electrolytes based on non-aqueous solvents with additions of specifically adsorbing, so-called surface-active, anions and physically adsorbing organic compounds. The role of electrode potential on the region of ideal polarisability has been demonstrated by in situ Fourier transform infrared (FTIR), Raman, EIS, and synchrotron beam–based X-ray photoelectron spectroscopy (XPS) studies [5, 65, 101, 107–115]. Electrochemical blocking of electrodes under high overpotentials due to the electropolymerisation of active organic compounds has been demonstrated, and patents have been received [116]. This effect is significant in avoiding overcharging EDLC, HSC, LIBs, and SIBs.

The influence of the polymer membrane characteristics on EDLCs, HSCs, LIBs, and SIBs has been studied by Tõnurist (Liivand) et al. [99, 117, 118]. It was demonstrated that the power density, as well as energy density of EDLCs completed with various self-made polyvinylidene membranes using the electrospinning method [119–123], depends very strongly on the electrolyte membrane characteristics (on the meso-macroporosity, thickness, pore size distribution, etc.), especially in solvents with high viscosity (including ILs).

The carbide-derived carbons (CDCs), such as Mo_2C-derived hierarchically porous carbon with an optimal ratio of micro- and mesopore volumes, have been used for the fabrication of artificial switches/muscles [124–126]. The quickest relaxation times have been established for highly mesoporous carbon–based switches [124–127]. The carbon materials synthesised have been studied by novel in situ methods, including small angle neutron scattering (SANS), quasielastic (QENS), and inelastic (INS) neutron scattering methods, wide-angle X-ray diffraction, and other synchrotron beam

based and traditional gas adsorption methods [8, 128–134]. It was found that for hydrogen storage, very microporous carbon materials can be applied. The same tendency is valid for CH_4 storage [133–136].

The Faradaic processes at MMP carbon electrodes activated with Pt, Pt-Ru, Pt-Ir, Pt-CeO_2, Pt-Pr_6O_{11}, and d-metal = nitrogen nanoclusters (Fe = N_2, Co = N_2, FeCo = N_2) activated catalysts depend exceptionally strongly on the carbon support specific surface area, mesopore volume ratio to micropore volume, and pore size distribution function of carbon support and to surprisingly large extent on the electrical conductivity of powder under application [4, 5, 137–170].

Solid oxide materials for solid oxide fuel cells (SOFC) and electrolysers [66, 171–180], including complex perovskite oxides, Ni–cermet anodes, and fluoride-type electrolytes, have been synthesised and tested for solid oxide fuel cells and electrolysers by Nurk, Kivi, Lillmaa, Korjus, Maide, and Heinsaar since 2001 [181–213]. Different complex oxide electrode synthesis methods have been applied, starting from the solid oxide high-temperature sintering method.

Electrical double layer structure at single-crystal metal and carbon electrodes

The electrical double layer structure at different electrodes has been studied in various electrolytes such as H_2O, acetonitrile (ACN), ethanol, methanol, propylene carbonate (PC), gamma butyrolactone (GBL), ethylene carbonate (EC), and dimethyl carbonate (DMC) [36, 59, 214–220]. For that purpose, various methods such as cyclic voltammetry (CV), EIS, in situ scanning tunnelling microscopy (STM) and atomic force microscopy (AFM), in situ FTIR and Raman as well as *operando* synchrotron radiation beam–based photoelectron (SR-XPS), and SANS have been applied. Typically, the CV method is employed first when studying the systems mentioned above to determine their ideal polarisability range. It was found that the region of ideal polarisability is narrow for Cd(*hklf*) and very wide for C(0001) and graphene electrodes. The series capacitance, electrode potential curves (*C vs E* curves) calculated from Nyquist complex plane ($-Z''$, Z') plots, given in Fig. 1, show that the interfacial properties of electrode | H_2O and electrode | non-aqueous electrolyte solution depend on the metal electronic characteristics and used solvent chemical composition. The series capacitance can be divided into the inner layer (C_i) and outer layer (C_d) capacitances, connected in series:

$$\frac{1}{C} = \frac{1}{C_i} + \frac{1}{C_d}. \quad (1)$$

In 1980–1990s [1, 2, 11, 12, 21, 38–43, 58, 59], it was demonstrated that C_i can be represented as:

$$\frac{1}{C_i} = \frac{1}{C_m} + \frac{1}{C_{dip}} + \frac{1}{C_H}, \quad (2)$$

where C_m is the capacitance of the metal or thin surface film, C_{dip} is the solvent layer capacitance, and C_H is the Helmholtz capacitance.

The influence of electrode material on the interfacial capacitance has been demonstrated by Oll et al. [62]. In the given study, very low C_s values have been measured for ionic liquid–based systems (Fig. 2), increasing from C(0001) (non-metallic electrode) towards Au, known as an ideal electronic conductor. For a semi-metallic Bi, the moderate C_s values, similar to Pb, have been calculated. It should be stressed that for Bi, Pb, Pt, and Au, the high-vacuum electromagnetic deposition method of electrode materials has been used to avoid any chemical contamination of surfaces during the chemical or electrochemical polishing steps. Furthermore, it can be seen how the crystallographic structure of the carbon electrode influences the C_s values. A very sharp capacitance minimum can be seen for a very high-quality graphene electrode and C(0001). This capacitance minimum is mainly caused by the potential drop inside the graphene and C(0001) surface layer due to the very low concentration of charge carriers in the electrode surface layer [2, 58, 222], which results in low C_m. Oll et al. also showed that there is no hysteresis of C_s *vs* E curves that is visible in the case of amorphous carbon electrodes. It is very interesting that the potential of capacitance minimum somewhat depends on the carbon electrode under study, but overlapping E_{min} values can be seen for graphene and partially graphitised porous carbon synthesised from TiC using chlorination method and further cleaned during high-temperature (800 °C for 4 h) hydrogen reduction step. Surprisingly, there is no capacitance minimum in the C_s *vs* E curve for amorphous carbon electrode, explained by the non-ideal metal phase structure and slow kinetics of formation of EDL at the micro-mesoporous surface.

In addition to experimental investigations, numerous computational studies have been conducted to study the electrode | ionic liquid EDL structure and its properties [46–52, 223–226]. Followingly, these studies have allowed investigation of the adsorption of ionic liquid ions on the electrode's surface, which is experimentally challenging, as well as the influence of the electrode's potential on the EDL structure. For instance, in the case of Bi(111) | ionic liquid interface, the DFT calculations allowed to reason the difference between the measured capacitance of $EMImBF_4$ and 1-butyl-4-methylpyridinium tetrafluoroborate ($BMPyBF_4$) by estimating the optimal distance between the electrode's surface and ionic liquid ions, which are related to the C_H [227]. Under intensive scrutiny has been the computational estimation of *C vs E* dependence, as it can be determined

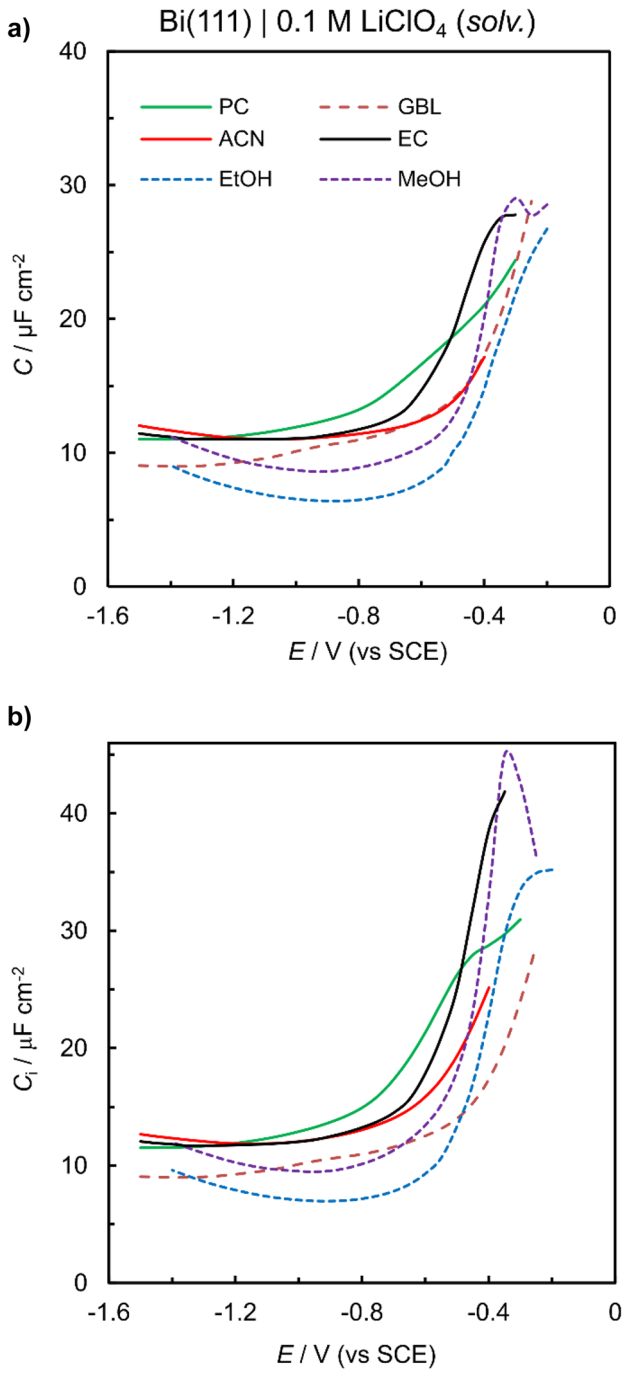

Fig. 1 **a** Series capacitance, electrode potential curves (*C vs E* curves); **b** inner capacitance, electrode potential curves (C_i *vs E* curves) for Bi(111) electrode in 0.1 M $LiClO_4$ solution in different solvents (given in the figure) [5, 215–218, 221]

both experimentally using EIS and computationally. Numerous aspects of *C vs E* dependence and capacitance-structure dependence at the metal | ionic liquid interface have been investigated by Ivaništšev et al. [46, 47, 223–226]. Using constant field MD simulations, the occurrence of aforementioned capacitance hysteresis has been reasoned with the

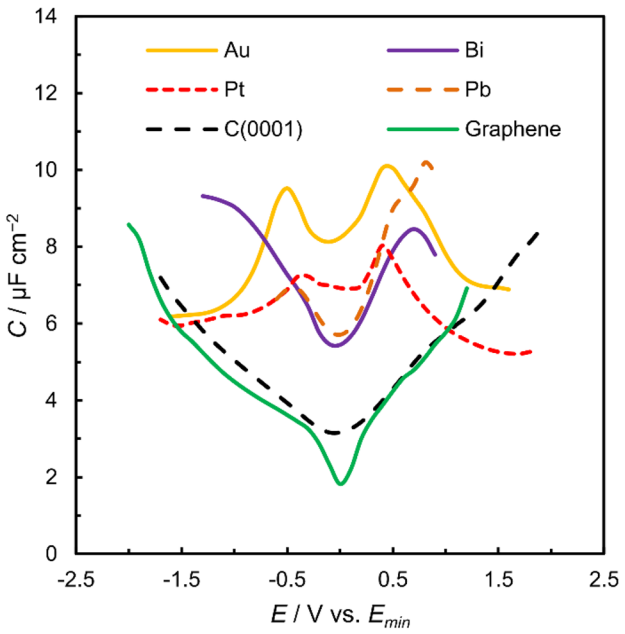

Fig. 2 *C vs E* dependences for different electrode materials measured in $EMImBF_4$ [62]

formation of different ionic liquids interfacial structures, which need overpotential to transition from one structure to another [50]. The impact of the surface charge plane position at Au(*hkl*) | ionic liquid interfaces has been highlighted by Voroshylova et al. by showing that a simple correction of computational data significantly improves the agreement with the experimental results [48]. Furthermore, a recent study showed that the peaks in a *C vs E* curve arise due to the restructuring of the ionic liquid near the electrode's surface [51]. The effect of temperature and quantum capacitance (i.e., C_m) on the *C vs E* dependence of graphene | ionic liquid interface has been studied by Ers et al. [49, 52], showing that the quantum capacitance has a significant impact on the overall interfacial capacitance. In contrast, the temperature has a minor effect on the interfacial capacitance near the potential of zero charge (pzc) when the quantum capacitance is very low, as shown in Fig. 3b.

Adsorption of organic compounds from H_2O and IL electrolytes

The adsorption of organic compounds at Bi(*hkl*), Sb(*hkl*), Cd(*hklf*), and C(0001) electrodes has been studied mainly by EIS and in situ STM and AFM methods [228–242]. The data collected for the adsorption of aliphatic alcohols, cyclohexanol, cyclohexanone, and cyclohexane carboxylic acid at Bi(*hkl*), Sb(111), and Cd(0001) facets have been discussed in detail in Lust et al. [13]. It was concluded that the Gibbs

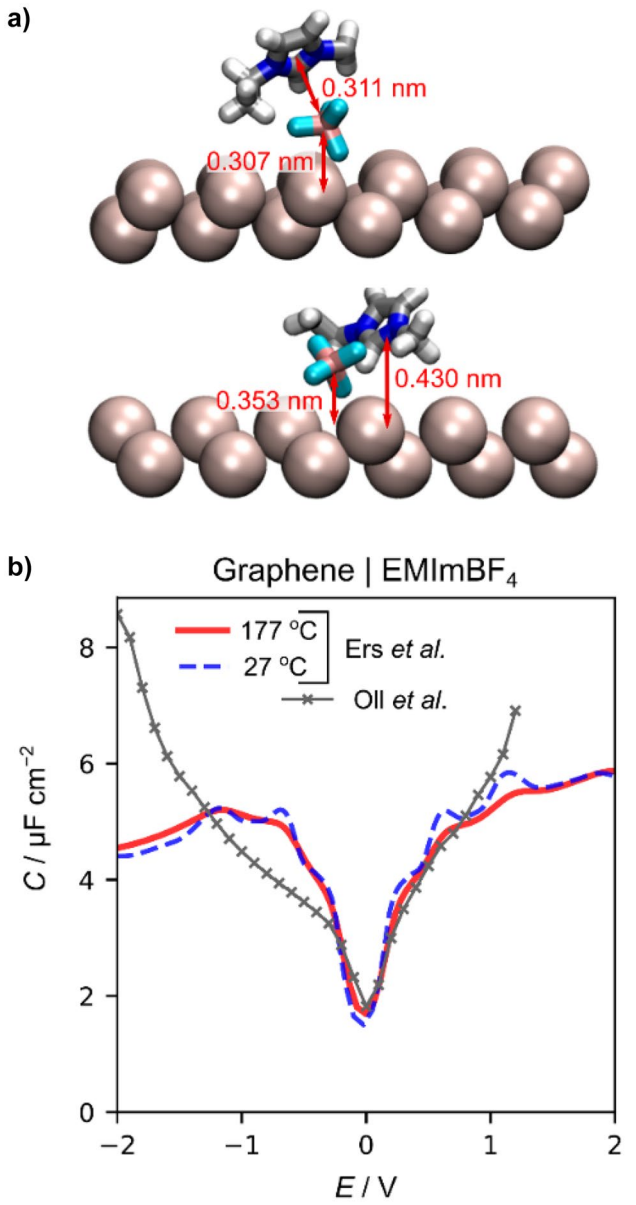

Fig. 3 **a** The structures of $EMImBF_4$ ionic pair on Bi(111) surface together with measured distances [227]. **b** The *C vs E* curves for graphene | $EMImBF_4$ obtained from experimental measurements [62] and using molecular dynamics simulations at temperatures 27 °C and 177 °C [52]

adsorption energy increases from Bi(111) to Bi(011) facet and from Bi(111) to Sb(111). The small positive calculated formal charge transfer coefficient values (from 0 to 0.09) characterise the substitution of water clusters, consisting of two or three molecules and a small dipole contribution of the functional group of adsorbate, which is directed towards the solution. Additionally, it was found that the organic compound adsorption activity is lowest at Cd(0001) and highest at Sb(111) facet [13, 228–232, 240–242]. Thus, the H_2O adsorption activity decreases from Cd(0001) to Sb(111) [1, 2].

The adsorption behaviour of 2,2′-bipyridine (2,2′-BP) and 4,4′-bipyridine (4,4′-BP) molecules has been investigated by in situ STM method [237–241]. For 2,2′-BP and 4,4′-BP, the compact adsorption layer forms, which has been visualised. The in situ STM data, given in Fig. 4, show the highly organised molecular rows of 4,4′-BP at various electrodes together with the models of formed layers. Interestingly, these rows' configurations depend on the electrode's crystal structure and metallic properties.

It should be stressed that the atomic level adsorption layer structure of 4,4′-BP depends on the concentration of surface-inactive electrolyte [239]. With the increase of ionic strength, the Gibbs adsorption of 4,4′-BP increases in agreement with data for other organic molecules' adsorption at metal electrodes [13]. Interestingly, recently, Pikma et al. showed that in an ionic liquid environment, the adsorption of 4,4′-BP takes place in two distinctive self-assembled layers, one on top of the other, not just in a monolayer [241].

Additionally, the adsorption of camphor and thiourea was investigated on the Bi(111) surface. Similarly to 4,4′-BP, camphor forms a highly regular adsorbed layer at Bi(111) (Gibbs adsorption $2.3 \cdot 10^{-10}$ mol·cm^{-2}) [238]. It is fascinating that, in contrast, the thiourea, exhibiting weak specific chemisorption behaviour at Bi(111), does not form a regular adsorption layer. Surprisingly, there are no adsorbed thiourea molecules at ideally flat monocrystal areas. Instead, the adsorbed molecules can be observed at defect surface areas, i.e., on the step edges of the characteristic triangular steps [234], illustrated in Fig. 5.

EIS, Raman, and infrared spectroscopy methods have been used to study the chemical interaction between Bi(*hkl*) and other sulphur-containing organic compounds [243]. It was identified that the interaction is very strong, and due to chemisorption, a bismuth-thiolate layer forms at the Bi(111) surface.

Adsorption of halide anions at single-crystal Bi(hkl), Sb(111), and Cd(0001)

Specific adsorption of ions from H_2O, non-aqueous, and IL mixture electrolytes at metal and carbon electrodes has been a focus of intensive studies and discussions since the 1960s [1, 2, 5, 20, 22, 24, 25, 33, 60, 62–65, 99–101, 112–114, 215–218, 220, 221, 244–255]. Various models (Hurwitz-Parsons [244–246], Kolotyrkin et al. [256], Damaskin [257], Palm and Damaskin [258], etc.) and modified isotherms and models [38, 259–265], including the conception of partial charge transfer, have been developed and tested. It was found that the Frumkin adsorption isotherm can be used for the interpretation of specific adsorption data calculated at fixed potentials [215–218, 220, 221, 247–253, 255, 257, 258]. The specific adsorption of halides has been studied

by CV, EIS, SR-XPS, and subtractively normalised interfacial Fourier transform infrared spectroscopy (SNIFTIRS), in situ Raman, and in situ STM/AFM methods. It was found that the adsorption of halide anions depends on the single-crystal plane structure, solvent characteristics, and on the anion or cation chemical composition. The anion surface activity increases from Cd(0001) to Sb(*hkl*) and from F^- to I^-. The halide adsorption is nearly reversible up to *C vs E* curves peak potentials in agreement with in situ STM data. As for the Bi(111) interface, very stable adsorption superstructures have been observed for I^- and Br^- containing electrolytes. The contact adsorption of Cl^- is more questionable at the Bi(111) interface as only a weak Moire structure of an adlayer has been observed. It is interesting that within a very wide potential region (even over 1 V), the Br^- and I^- superstructure is stable and drastic reorganisation processes of the electrode surface structure have been observed only at very high negative (desorption of anions) and at very positive potentials, where dissolution/oxidation of Bi(*hkl*) surface started [5].

The adsorption of halide anion starts at a very negatively charged electrode surface, in agreement with in situ STM and SR-XPS data, and this phenomenon is known as the specific adsorption of anions as it takes place against the electrostatic repulsion forces. Data in Fig. 6 and in Table 1 indicate that the Gibbs adsorption energy is influenced by the solvent chemical composition, and the strongest adsorption of I^- takes place from ACN (where the solvation energy of anions is lowest).

Surprisingly, it was found that the simple virial isotherm can be applied for the analysis of specific adsorption data from ACN, ethanol (EtOH), methanol (MeOH),

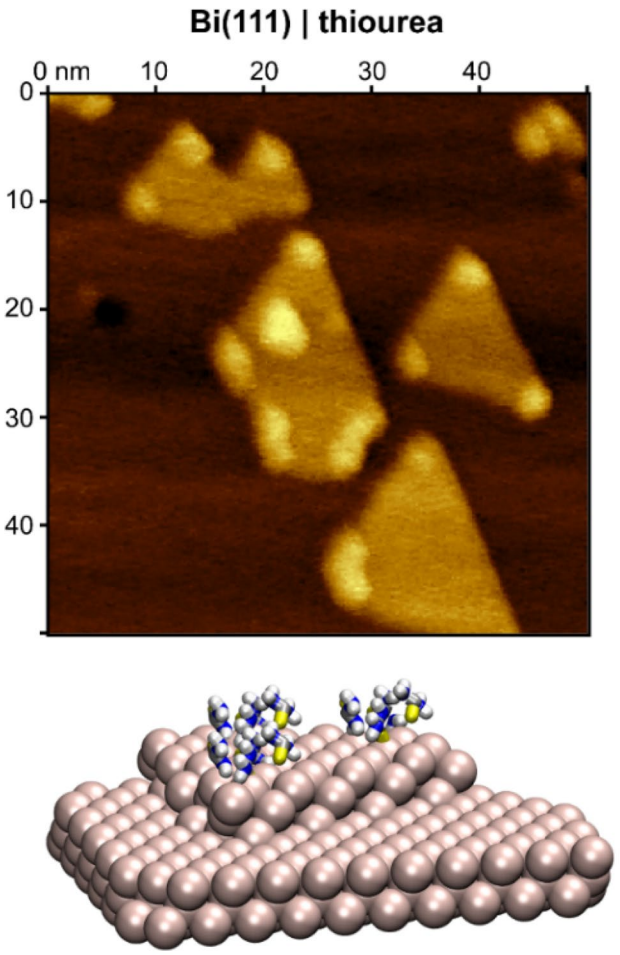

Fig. 5 In situ STM image and model highlighting the adsorption of thiourea at the defect surface areas of Bi(111) surface [234]

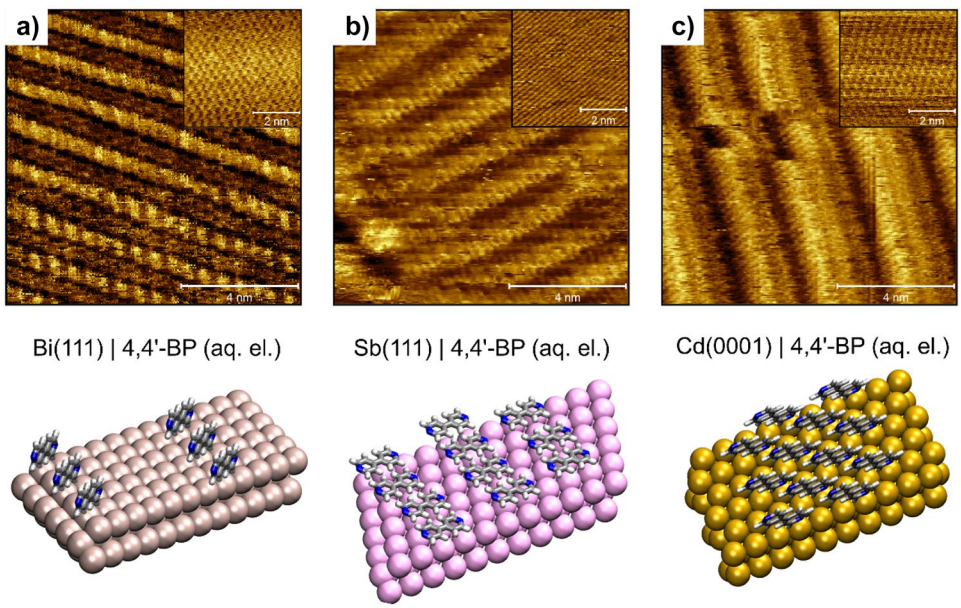

Fig. 4 In situ STM images of 4,4′-bipyridine monolayers together with proposed packing models on **a** Bi(111), **b** Sb(111), and **c** Cd(0001) single-crystal electrode [239, 240, 242]

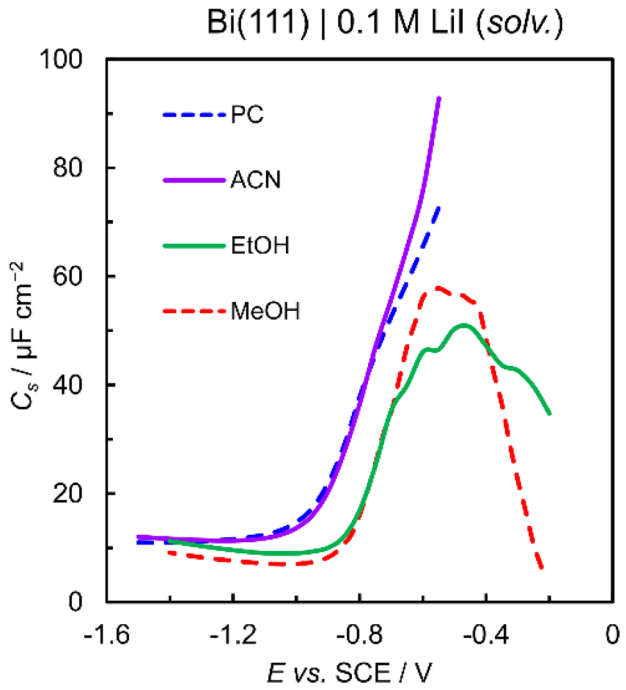

Fig. 6 C_s *vs* E curves for Bi(111) electrode in 0.1 M LiI in different solvents [5]

PC, and ethyl methyl carbonate (EMC) mixed binary electrolyte solutions with moderate constant ionic strength [12, 59, 215–218, 220, 221, 247–253, 255, 258]. According to the Hurwitz–Dutkiewicz-Parsons method [244, 245], charges for specifically adsorbed ions σ_1° can be calculated at constant surface charge density σ or at constant electrode potentials E, according to formulas:

$$\sigma_1 = (\frac{F}{RT})(\frac{\Delta\xi}{lnx})_{\sigma=const} \tag{3}$$

$$\sigma_1 = (\frac{F}{RT})(\frac{\Delta\gamma}{lnx})_{E=const} \tag{4}$$

where ζ is the Parsons' function $\zeta=\gamma+\sigma E$ and $\Delta\zeta=\zeta_0-\zeta$ at constant σ, γ is the specific surface work value, $\Delta\gamma=\gamma_0-\gamma$ at constant E, and the parameters with index 0 corresponding to these values in the supporting electrolyte. The most important adsorption characteristic, the Gibbs energy of adsorption $-\Delta G_A$, was obtained by fitting the σ_1 values to the semi-empirical simple virial isotherm [12, 20–22, 33, 59, 215–218, 220, 221, 244–253, 255].

$$ln(\frac{\sigma_1}{zxc}) = -\frac{\Delta G_A}{RT} - \frac{2B_{\text{eff}}\sigma_1}{z} \tag{5}$$

or to the corrected virial isotherm

$$ln(\frac{\sigma_1}{zxc}) = -\frac{\Delta G_A}{RT} - \frac{2B_{\text{eff}}\sigma_1}{z} \tag{6}$$

with

$$\psi_0 = \frac{2RT}{|z|F} arcsh\left(\frac{\sigma+\sigma_1}{2A\sqrt{c}}\right) \tag{7}$$

where z is the charge number of the adsorbed anion (-1 in the case of I^-, Br^-, and Cl^- anions), c is the total concentration of electrolyte solution (0.1 M), and B_{eff} is the second virial coefficient, characterising the mutual repulsion (and size) of the adsorbed ions. Using a simple virial isotherm, the B_{eff} is an effective parameter because we have neglected the dependence of the diffuse layer potential drop (ψ_0 from σ_1) in isotherm (3) and calculations. However, the B_{eff} values can be used for very preliminary analysis of the mutual interaction of adsorbed ions from various solvent systems [12, 59, 215–218, 220, 221, 247–253, 255, 258], especially at E_{min} potential (pzc), where the ψ_0 potential drop value is zero and B_{eff} can have some (comparative) physical meaning. The coinciding σ_1 value, calculated both ways, gives evidence of the self-consistency and correctness of the obtained data. Similar to non-aqueous mixed electrolytes, Damaskin and Palm introduced additional corrections for isotherms [257, 258], but surprisingly deviation of the corrected experimental isotherm from linear correlation increases further. This approximation has been criticised by Vorotyntsev [266], but no final theory has not been developed yet.

The slope of a virial isotherm depends on the electrode metal studied, and for Bi(*hkl*), not shown for shortness, the slope values are higher if compared with Cd(0001) plane. Thus, B_{eff} values calculated using uncorrected isotherm can be used only for qualitative analysis of data, assuming that in the same solvent, the ψ_0 effects are comparable for different Bi(*hkl*) planes.

Systematic analysis of experimental data for Bi and Sb electrodes demonstrates that the ψ_0 potential drop corrections

Table 1 The Gibbs adsorption energy values for I^- ions at the Bi and Cd electrodes from different solvents

Electrode	$-\Delta G_A^0$ (H_2O) kJ/mol [10, 253]	$-\Delta G_A^0$ (MeOH) kJ/mol [249, 253]	$-\Delta G_A^0$ (EtOH) kJ/mol [249, 253]	$-\Delta G_A^0$ (EC) kJ/mol [216]	$-\Delta G_A^0$ (PC) kJ/mol [250]	$-\Delta G_A^0$ (GBL) kJ/mol [217]	$-\Delta G_A^0$ (ACN) kJ/mol [218]
Bi(111)	92.0	94.2	98.5	100.0	102.0	103.9	105.1
Cd(0001)	99.4	93.8	94.5				

in diffuse layer applied for corrected isotherm (4) are usually strongly overestimated [12, 26, 27, 30, 59, 215–218, 220, 221, 247–253, 255, 258]. Only for water-based binary electrolyte systems with constant ionic strength electrolyte systems the diffuse layer potential drop (ψ_0 potential drop) corrections for quantitative analysis of data at Bi(*hkl*) electrodes can be used [12, 59, 247, 258]. The same effect, i.e., overestimated ψ_0 value, has been observed for analyses of faradic charge transfer processes at Bi(*hkl*) and Cd(0001) electrodes [267–276] if the Frumkin slow charge transfer theory [21, 26–28, 30, 66, 277–283], including ψ_0 potential correction, has been applied. Thus, the role of diffuse layer seems to be insignificant for specifically adsorbing anions from non-aqueous electrolytes and nearly contact adsorption of Cl^-, Br^-, I^-, and SCN^- anions at single-crystal planes from non-aqueous electrolytes [12, 59, 215–218, 220, 221, 247–253, 255, 258], including from ILs and IL mixtures as well as IL with addition of solvent [5, 63–65, 101, 107–109, 112–114], demonstrated using in situ STM [5, 100, 114, 284], infrared spectroscopy [60], and in situ synchrotron beam–based XPS measurements data [109, 110].

This is in agreement with the very weak influence of solvent characteristics (dipole moment, dielectric permittivity, donor–acceptor number, etc.) on the Gibbs adsorption energy, but specifically on the values of formal charge transfer coefficient (so-called electrosorption valency) and effective dipole moment [38, 216–218, 220, 247–253, 259, 262–265], created at metal | electrolyte interface, being 10 times lower for Bi, Sb, and Cd electrodes, than the dipole moment values calculated for ideal conductor | anion at vacuum interface [12, 26, 27, 30, 59, 215–218, 220, 221, 247–253, 255, 258]. Due to the partial charge transfer process being reversible within the moderate potential region at non-ideal metals (Bi, Sb), the adsorption of halide ions is a complicated process, and new systematic studies and detailed comparison of experimental data from various aprotic and technologically important solvents (ACN, EC, PC, EMC, DMC, diethyl carbonate (DEC), GBL) and IL mixtures, potentially applicable in modern energy storage and conversion devices like batteries and EDLCs [215–218, 250], have a more straightforward direction of studies.

The Gibbs adsorption energy values, given in Table 1, indicate that there are noticeable differences between Cd, Bi(*hkl*), and Sb(*hkl*) electrodes with the increasing adsorption activity in the presented order of metals. The most active adsorption for Bi(*hkl*) has been observed for most reticular density plane Bi(011) plane and very lyophilic C(0001). Adsorption of I^- anions (like Br^- and Cl^- anions) increases in the order of solvents; $H_2O < MeOH < EtOH < EC < PC < GBL < ACN$, demonstrating that with the decrease of solvation energy of anions, the Gibbs adsorption energy increases.

Data in Fig. 7a show that the C_s depends extremely strongly on the chemical composition of IL under study. Very low capacitance values have been calculated for big anions with high molar volume. The surface structure of Bi(111) and Bi(01 $\bar{1}$) has shown to be very stable within a wide potential region [114, 285]. Only at moderately negatively charged electrode surface ($E = -1.6$ V *vs* Fc/Fc^+ reference electrode) the Moire superstructure has been observed, dependent on the electrode crystallographic structure, surface electrochemical activity, and electrode potential.

The capacitance values are very sensitive for water additions in IL. For extremely well-dried 1-ethyl-3-methylimidazolium trifluoromethanesulfonate (EMImOtf), very low capacitance values have been calculated, demonstrated in Fig. 7b. In very well-dried IL, the capacitance values are higher for the Bi(01 $\bar{1}$) plane and lower for Bi(001), like for H_2O electrolytes. The capacitance values increase noticeably when the H_2O concentration increases. Detailed analysis

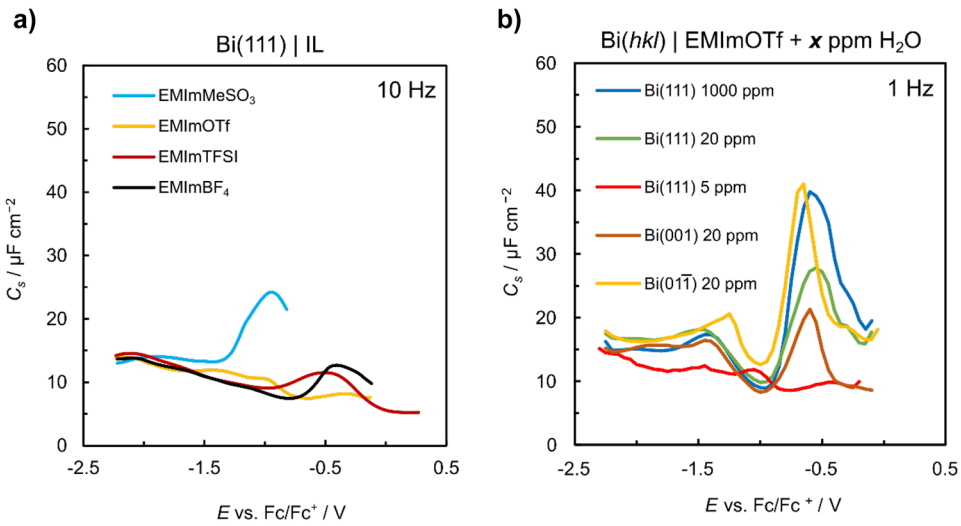

Fig. 7 **a** C_s *vs* E curves for Bi(111) | IL systems [5]; **b** C_s *vs* E curves for Bi(*hkl*) | EMImOTf systems with specified water content [114]

of EIS data demonstrates that the adsorption of anions is quicker than cations (nearly 1.5 orders), but the series capacitance values are very low for big fluorinated anions (OTf^-) within all adsorption regions demonstrating slow adsorption kinetics similar for big cations. Nearly ideal capacitive behaviour has been observed from −1.7 to −0.6 V *vs* Fc/Fc^+.

The specific adsorption of Cl^-, Br^-, and I^- anions from surface-inactive IL $EMImBF_4$ mixture has been analysed (Fig. 8). Very similar behaviour as already discussed for H_2O [12, 59], non-aqueous surface-active electrolytes [218, 220, 221, 247–253, 255] has been established for halide ions + IL electrolytes for Bi(*hkl*), Sb(111), Cd(0001), and C(0001) planes by Siinor and Siimenson et al. [63, 65, 286, 287]. STM images in Fig. 8 show the well-organised adsorbed layers of I^-, Br^- from $EMImBF_4$. With the increase of halide anion concentration in surface-inactive electrolyte, the differential capacitance curve shifts towards more negative potentials, but the maximal capacitance values (C_s(max) = 58 μF·cm^{-2}) are

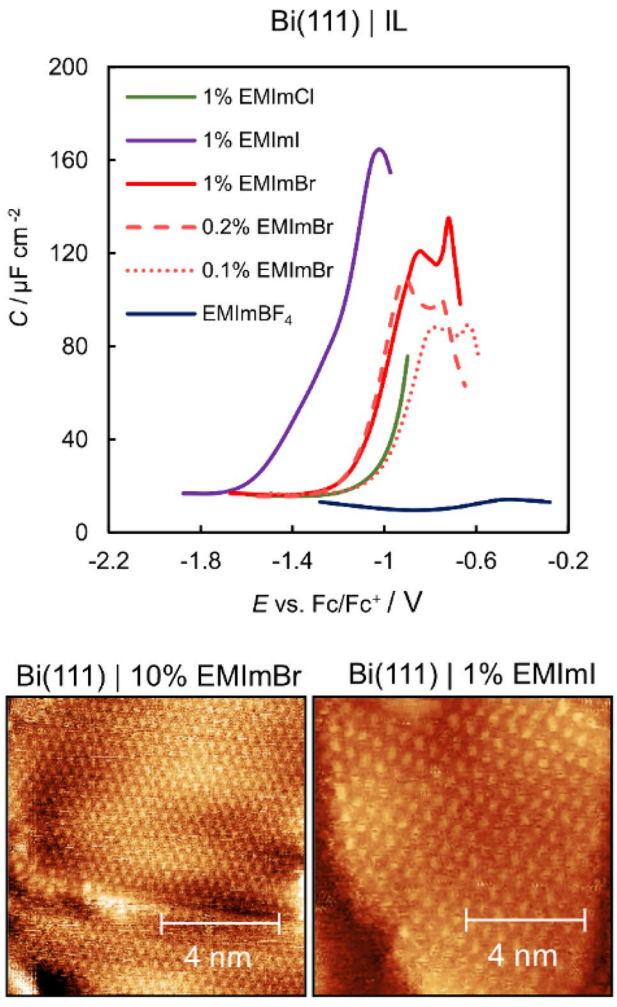

Fig. 8 C_s *vs E* curves for Bi(111) | IL systems containing specifically adsorbing halide anions, together with in situ STM images of systems containing Br^- and I^- ions [5, 65, 100]

independent of Br^- (or I^-) additions in surface-inactive IL. The back-integration method of C_s *vs E* curves has been used to calculate surface charge density values in [5]. Using the given method, very high surface charge densities have been calculated, indicating the high surface activity of halide anions at Bi(*hkl*) and Sb(111) surface from IL. Therefore, the higher charges for non-aqueous solutions containing specifically adsorbed I^- ions have been calculated.

At very negative potentials, there is no halide adsorption and only with the increase of electrode potential does the specific adsorption start. It is surprising that the I^- and Br^- adsorption is very intensive, and it takes place already at a highly negatively charged (−12 or −10 μC·cm^{-2}, respectively) surface. It is to be stressed that the adsorption of halides is nearly reversible up to capacitance maximum potentials for Sb(*hkl*) and Bi(*hkl*) electrodes. Thus, halide specific adsorption–based pseudocapacitors can be developed for enhanced energy density storage. The in situ STM data show that there are ions at the Bi(111) electrode surface with a regular distance of 0.42 nm between the Br^--anion centres. The Cl^- adsorption is weak, and only after long-lasting polarisation of Bi(111) at fixed potentials the Moier's superstructure is formed at the electrode with constant ionic strength.

There is a significant influence of the single-crystal planes and carbon electrode surface crystallographic structure (C(0001), graphene, porous carbon) on the shape of complex plane EIS plots (−Z" *vs* Z′) and *C vs E* [7, 63, 65, 68–87, 89, 286–290]. Thus, the surface charge density *vs* potential curves (σ *vs E*), established using the back-integration method of *C vs E* curves, depend very remarkably on the electrode studied. For comprehensive analysis and development of supercapacitors, HSC, LIBs, and SIBs, systematic analysis of data, including analysis of the influence of solvent polarisability, dielectric constant, and viscosity, is inevitable. Specific adsorption of iodide and bromide from non-aqueous surface-inactive electrolyte (E_4NBF_4, E_3MNBF_4, and EM_3NBF_4 in ACN) and from IL systems ($EMImBF_4$ + EMImI, $EMImBF_4$ + EMImBr, and $EMImBF_4$ + EMImCl) at carbon electrodes [63, 65, 284, 286, 287] has been applied for the enhancement of specific energy and power densities of HSC based on MMP carbon or carbon microsphere electrodes.

Electrochemical kinetics at single-crystal electrodes

Thomberg, Jäger, and Härk have studied the electroreduction of $[H_3O]^+$ [14, 273] and $[S_2O_8]^{2-}$ at Bi(111) [271] and Cd(0001) [268, 270, 274], as well as $(Co[NH_3]_6)^{3+}$ [269, 272] and Eu^{3+} [275] at Bi(*hkl*) and Cd(0001) by CV, EIS, and chronoamperometry methods. $[Fe(CN)_6]^{3-}$ anions at Cd(0001) electrode have been studied by Nerut et al. [276]. It was found that the reduction rate depends

on the crystallographic structure of the electrode used, as well as on the chemical composition and electronic characteristics of the electrode material (Bi or Cd) studied.

The overvoltage of $[H_3O]^+$ electroreduction increases from Bi(111) to Bi(01 $\bar{1}$) [14, 268–271, 273–275] in the same order as established for the increase of adsorption activity of anions and organic compounds, explained by weaker adsorption of water molecules at Bi(111) and Bi(*hkl*) as well as weaker chemical adsorption of $[H_3O]^+$ on Bi(111) plane compared with Bi(01 $\bar{1}$). For more chemically active planes, i.e., Bi(01 $\bar{1}$) and Bi(001), some deviation from Frumkin's slow discharge theory [26, 277] has been observed. This deviation has been explained by the weak adsorption of reacting compounds at the electrode surface. The given knowledge collected has been used for the development of electrochemical waste water purification systems [291].

The same order of activities has been recognised for $[S_2O_8]^{2-}$ and $[Co(NH_3)_6]^{3+}$ reduction at Bi(*hkl*). For more hydrophilic Cd(0001), a weaker deviation from Frumkin classical model has been observed. A more pronounced deviation of Bi(*hkl*) from the classical model [26, 277–280, 283, 291] can be explained by the semi-metallic character of Bi(*hkl*) compared with Cd(0001) and Au(*hkl*) surface planes [278–280, 283]. The electroreduction of $Eu_2(SO_4)_3$ has been studied at Bi(01 $\bar{1}$) electrode in acidic $HClO_4$ and H_2SO_4 solutions (at similar pH = 3.0) with additions of $LiClO_4$ and Na_2SO_4 electrolytes as surface-inactive electrolyte solutions. The kinetics of Eu^{3+} cations depends on the electrode potential applied and on the concentration of the supporting electrolyte.

The systematic analysis of the electroreduction data for Bi(*hkl*) indicates that similar to the specific adsorption of anions, the diffuse layer potential drop values are overestimated. Therefore, it seems that the centre for charge transfer for real systems is closer to the electrode than that assumed by the classical Frumkin slow discharge model, i.e., ψ_0 potential values are overestimated [14, 268–271, 273–276]. The new model developed by Damaskin et al. [30] is in better agreement than the classical ψ_0 correction model. Detailed analysis of EIS data indicates that within the moderate *ac* frequency region, the system is controlled by an adsorption step. Only mixed kinetic processes occur at very low *ac* frequencies, i.e., the adsorption and mass-transfer step processes are the rate-limiting steps at Bi(*hkl*) and Cd(0001) surfaces.

Development of electrical double layer and hybrid supercapacitors

Syntheses and characterisation of micro-mesoporous carbon powders from metal carbides

Carbon electrodes have been systematically studied since 1991 in order to establish the electrical double layer characteristics and pzc values for geometrically rough carbon and glassy carbon electrodes in ACN + $(C_2H_5)_4NBF_4$ solutions [1, 2]. Experimental EIS data measured at different *ac* frequencies demonstrated that the surface is geometrically rough, and the capacitance values depend on the glassy carbon and graphite electrode surface treatment methods, i.e., on the surface roughness values of electrodes. Also, the role of half-metal (semi-metallic) surface film properties of glassy carbon and graphite electrodes were analysed [86].

Since 1997, the binary (α-SiC, TiC, VC, B_4C, WC, Mo_2C, Al_4C_3, Cr_3C_2, etc.) [7, 67, 68, 70, 72–83, 85, 87] and ternary carbides (Ta_4HfC_5, $WTiC_2$) [82] have been used for the preparation of MMP carbon electrode powders with hierarchical porous structure. The so-called high-temperature chlorination method has been used for the synthesis of corresponding MMP carbon powders, respectively. The carbon powders were purified by the high-temperature hydrogen treatment step (by applying 750–850 °C for 2–6 h). HCl, CO_2, KOH, and $ZnCl_2$ or a combined $ZnCl_2$ + KOH mixture of activators were used for additional activation of C(α-SiC) and other carbon powders [83–85].

The carbon materials were analysed using X-ray diffraction spectroscopy (XRD), focused ion beam time-of-flight secondary ion mass spectrometry (FIB-TOF–SIMS), Raman spectroscopy, scanning electron microscopy with energy dispersive X-ray analysis (SEM–EDX), and high-resolution transmission electron microscopy (HR-TEM) combined with electron energy loss spectroscopy (EELS) and selected area electron diffraction spectroscopy (SAED) analysis methods [7, 67, 68, 70, 72–83, 85, 87]. The SEM–EDX data show that prepared carbon particles have complicated and variable shapes, containing wrinkled, blocked, and amorphous regions [84]. It is interesting that, for different CDCs, nearly graphitised blocks form between amorphous particles at sintering temperatures lower than 1200 °C. The HR-TEM-SAED-EELS data confirm this conclusion, demonstrating that the ordering of carbon takes place even at $T \geq 900$ °C [78–82]. The Raman spectra ($l = 514$ nm) were fitted with a combination of two Lorentzian and two Gaussian functions for both first-order and second-order Raman scattering regions [8, 70, 72–83, 85, 128–134, 288, 289, 292]. Detailed analysis of spectra indicates that with the increase of the final treatment temperature, the 2D peak and other second-order excitation peaks increased, demonstrating that the graphitisation processes have already started at 900 °C.

The Brunauer–Emmett–Teller (BET) gas adsorption method and Hg intrusion porosimetry methods have been used for detailed porosity analysis [7, 8, 67, 68, 70–83, 85, 87, 128–136, 169, 293–295]. For BET analyses, N_2, Ar, Kr, CO_2, and H_2 were used as test gases; various fitting methods (non-local density functional theory (NLDFT) and Saieus

program integrating different fitting models); different pore models (cylindrical pore, heterogeneous surface, standard slit, and aspect ratio 6) have been used [8, 71, 128–136, 169, 293–295].

Based on the BET gas adsorption method, the carbon powder micro-mesoporosity characteristics (ratio of micropore (V_{micro}) to mesopore volume (V_{meso}), the ratio of micropore surface area (S_{micro}) to mesopore surface area (S_{meso})) are influenced by binary and ternary carbide chemical composition, raw carbide crystallographic structure, and synthesis temperature (Table 2). The X-ray scattering and SANS data show that the nanostructure of C(Mo_2C) prepared at different chlorination temperatures depends on applied T [130, 132]. The specific inner surface area for C(Mo_2C), together with the volume fraction of the pores, increases with the chlorination temperature up to 900 °C, but at higher temperature values ($T > 1000$ °C), a significant decrease of both parameters takes place. Materials prepared at $T = 600$ °C or 700 °C are ultramicroporous, having a slit-like or cylindrical pore shape with an average size in the order of 0.6 nm. C(Mo_2C) synthesised at $T > 900$ °C have pore widths around 1 to 3 nm. Using the wide-angle X-ray scattering (WAXS), it was demonstrated that the pore shape of different CDCs varies, C(α-SiC) (1000 °C) has sphere-like pores ($d = 1$ nm), C(TiC) (950 °C) has cylinder-like pores, and C(Mo_2C) (1000 °C) has slit-like pores [129]. Thus, the raw CDC chemical composition and crystallographic structure have a significant influence on the geometrical shape of micropores formed. The pore surface roughness decreases with the chlorination temperature as well as with the increase of activation temperature used, established by SANS method results [8, 71, 128–134].

A more detailed study was conducted using the SANS method, where C(Mo_2C) were synthesised at fixed Cl_2 reaction temperatures of 700, 800, 900, and 1000 °C [130]. Results demonstrated that the shape of prevailing pores depends on the chlorination temperature applied, and there are structural geometry changes at the surface of the porous structure of materials studied. With increasing temperatures (from 700 to 1000 °C), microporous structures of materials change from mixed cylindrical/slit-like to purely slit-like. The observed changes in the geometries, expressed by the increase of the dimensionality parameter from 1.3 to 1.8, empirically correlate with the decrease of disorder between graphitic layers. Thus, the formation of the cylindrical pores can be explained by the curvature of graphitic carbon layers formed at $T < 800$ °C [130].

A combination of Raman spectroscopy and WAXS methods have been applied for detailed analysis of different CDC carbons synthesised from 6 different carbides at different temperatures (given after carbon powder in brackets) by chlorination and hydrogen cleaning methods from: Mo_2C (600 °C, 700 °C, 800 °C, 900 °C, 1000 °C, 1100 °C), Ta_4HfC_5 (800 °C, 900 °C, 1000 °C, 1100 °C),

Table 2 Results of the sorption measurements for the different micro- and mesoporous carbide–derived carbon materials

Carbide	T_{chlor}/°C	S_{BET}/m^2·g^{-1}	S_{micro}/m^2·g^{-1}	V_{micro}/cm^3·g^{-1}	V_{tot}/cm^3·g^{-1}	Ref
α-SiC	1000	1120	1110	0.51	0.54	[81]
	1100	1140	1130	0.51	0.52	
TiC	700	1320	1300	0.59	0.69	[296]
	900	1544	1503	0.71	0.87	
	1100	1448	1377	0.81	1.01	
VC	500	1163	1143	0.47	0.51	[70]
	700	1277	1256	0.56	0.62	
	900	1305	1282	0.63	0.66	
	1100	236	190	0.10	0.18	
Mo_2C	400	488	436	0.22	0.32	[78]
	600	1855	1823	1.08	1.14	
	800	1675	1559	1.18	1.40	
	1000	326	293	0.55	0.72	
	1200	146	0	0	0.80	
WC	800	1270	1260	0.56	0.59	[79]
	900	1290	1280	0.60	0.64	
	1000	1280	1260	0.61	0.66	
	1100	1580	1550	0.83	0.89	
Ta_4HfC_5	800	1810	1780	0.79	–	[82]
	900	1780	1760	0.81	–	
	1000	1990	1960	0.91	–	
	1100	1980	1950	0.95	–	
$WTiC_2$	800	1640	1630	0.72	–	[82]
	900	1840	1830	0.83	–	
	1000	1880	1860	0.84	–	
	1100	360	350	0.19	–	

$WTiC_2$ (800 °C, 900 °C, 1000 °C, 1100 °C), WC (800 °C, 900 °C, 1000 °C, 1100 °C), TiC (800 °C, 900 °C, 1000 °C, 1100 °C), and VC (500 °C, 600 °C, 700 °C, 800 °C, 900 °C, 1000 °C, 1100 °C) [129]. The 5-peak fit of the Raman spectrum first-order scattering region, suggested by Sadezky et al. [297], obtained the most coherent results. Thus, the influence of the T_{syn} on the peak shape, i.e., on the structural parameters of the collected results, showed the influence of the precursor carbide structural and chemical composition on the stage of graphitisation at equivalent temperatures at $T = 1000$ °C [129]. The graphitisation of C(Mo_2C) and C(VC), both synthesised at 1000 °C, was evident from the considerable narrowing of the G-band and from the increase in average graphitic areas stacking size, L_C, values obtained from WAXS data. The use of the ratio of Ad/Ag for the determination of the coherent domain length from Raman spectra based on the Ribeiro-Soares et al. method [298] yielded the most reliable results when compared to the L_a values calculated from WAXS data. The coherent domain length obtained from the Raman spectra was large (4.4 nm) than the average graphene layer extent value, L_a, obtained from WAXS. This discrepancy has been attributed to the number of defects and curvature in the graphene domains in the CDC-derived particles. Thus, this relates to the non-ideal structure of graphitic domains synthesised and formed into C(Mo_2C) and C(VC) at $T = 1000$ °C. Detailed Raman and WAXS analysis data demonstrated that these methods are complementary to each other, and the simultaneous application of the mentioned methods is of high importance for the characterisation of disordered partially graphitic/non-graphitic carbon materials.

For the development of materials with more advanced mesoporous structures, the sol–gel method was used for the preparation of mesoporous TiC raw powders [90]. After the chlorination and hydrogen cleaning steps, the XRD, Raman, SEM–EDX, XPS, X-ray fluorescence (XRF), HR-TEM, combined SAED and EELS, and BET measurements were conducted. It was established that the mesoporosity of sol–gel prepared carbons is noticeably higher than the corresponding values for C(TiC) derived from industrial carbon powders (Fig. 9). Also, the experimental Nyquist plots show that the EDLCs based on the carbon materials prepared using the sol–gel method have a very wide region of ideal polarisability up to 3.4–3.6 V [41].

Micro-mesoporous carbon materials prepared from glucose, white sugar, and Estonian well-decomposed peat

Fascinating nanospherical carbon materials have been synthesised from glucose, white sugar solutions, and Estonian well-decomposed peat powder [97, 137, 149, 150, 157, 299–304], shown in Fig. 10. Highly homogeneous carbon material consisting of nano- and microspheres with diameters nearly 0.9–1.0 µm has been prepared from glucose (C(Glc)), with particle size and shape practically independent of synthesis T (800–1400 °C) [97, 149, 150, 299–302], different from white sugar–derived carbon (C(WS)) [301], where the diameter of carbon spheres varies from 1 to 4 µm. HR-TEM data show that the surface of C(Glc) is nicely graphitised. It is interesting that the diameter of these C(Glc) nanospheres is independent from the applied activation temperature. Only at very harsh activation conditions with KOH have the nanospheres been destroyed for open meso- and macropores.

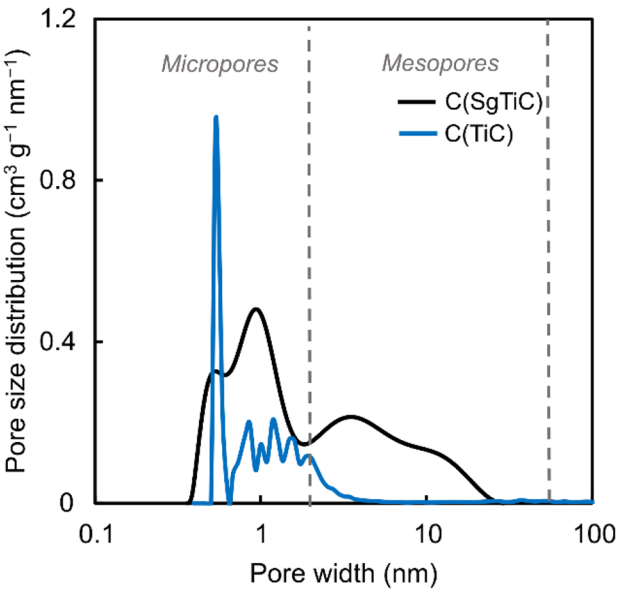

Fig. 9 Pore size distribution for commercially available (C(TiC)) and sol–gel prepared TiC derived (C(SgTiC)) carbon electrodes, calculated from combined N_2 and CO_2 adsorption isotherms [90]

Estonian well-decomposed peat has been used for the preparation of carbon powders (C(EP)) using high-temperature decomposition as well as hydrothermal carbonisation methods [137, 157]. Very well-oriented carbon graphitic areas can be seen in C(EP) material from with Raman spectroscopy, SEM–EDX, and HR-TEM data. For application in EDLCs, proton-exchange membrane fuel cells (PEMFCs), and gas adsorbing devices (mainly H_2 and CH_4), an additional carbon material treatment process at high activation temperatures using KOH or $ZnCl_2$ has been conducted [305]. Depending on the activation temperature and activation reactant applied, the micro-mesoporous structure has been developed with a specific surface area from 540 up to 2150 $m^2 \cdot g^{-1}$. The Raman spectra indicate that some graphitisation (or crystallographic ordering) has started already at 900 °C, 1100 °C, and 1400 °C [3].

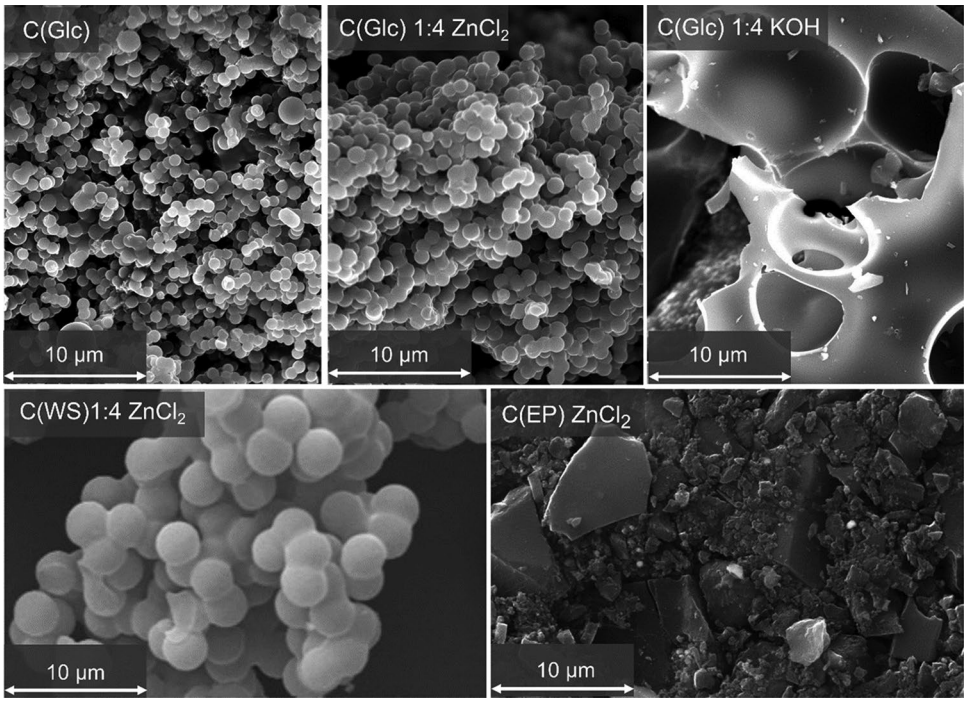

Fig. 10 Surface images measured using HR-SEM for various samples (noted in the figure) [97, 137, 149, 150, 157, 299–304]

Electrochemical results for EDLC and hybrid supercapacitors based on non-aqueous electrolyte solutions

For electrochemical studies, both three-electrode and two-electrode electrochemical setups were applied. The electrodes have been assembled using carbon materials described earlier and the Teflon suspension in H_2O as the binder [7, 67, 68, 70, 72–83, 85, 87, 90–97, 137, 149, 150, 157, 299, 300, 302–304, 306, 307]. The pastes of electrode materials were roll-pressed into thin carbon films with thicknesses from 60 to 400 µm. Generally, the Al current collectors were deposited onto one side of the roll-pressed film electrodes using the electromagnetic deposition method (in a high vacuum (10^{-8} bar)) for good electrical contact. Other times the electrospinning method of carbon layer deposition and followed by isostatic compression has been used for comparison. It should be noted that the influence of the electrode thickness on the energy and power densities is substantial [67]. This phenomenon will be discussed in more detail later, but in the referred works, electrodes with a thickness of 100 µm have been mainly used. The other aspect is that the electrolyte concentration has a significant influence on the electrochemical results. The complex impedance plane plot shape changes with the decrease of electrolyte concentration and the high-frequency series resistance $R_s(hf)$ somewhat increases [86, 87]. Furthermore, the high-frequency polarisation charge transfer (R_{ch}) resistance (i.e., the wideness of small high-frequency semicircle) and the mass-transfer limited processes resistance (R_D) (wideness of linear area with 45° slope) increases, and the limiting capacitive (at very low *ac* frequencies) behaviour has been established only at very high series resistance values.

Various non-aqueous solvents (ACN, GBL, PC, DMC, EC, etc.) and mixtures of organic carbonates (EC:DMC; PC:EC; DMC:EC:PC, etc.), as well as ethylacetate, acetone (AC), solutions of Et_4NBF_4, but mainly $TEMABF_4$ as electrolytes have been used, and the results are displayed in Fig. 11 [69]. It was found that the region of ideal

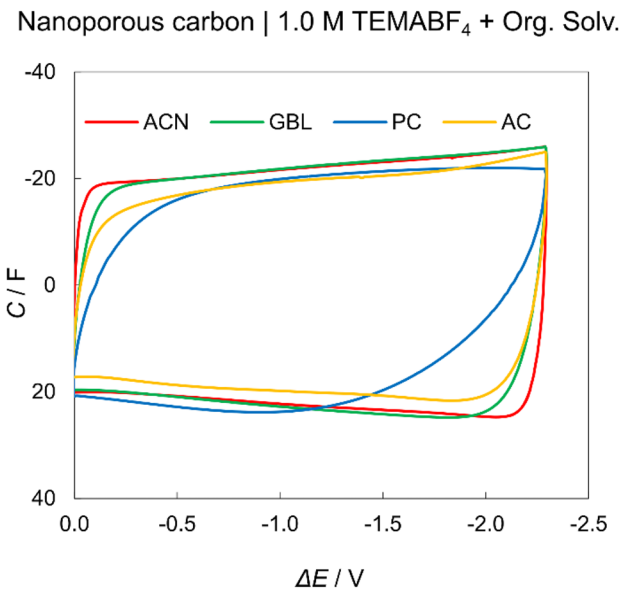

Fig. 11 *C vs E* curves at a cell potential scan rate of 50 mV·s.$^{-1}$ for the EDLCs in 1.0 M $TEMABF_4$ in ACN, GBL, AC, and PC [69]

polarisability is very wide for well-dried ACN + $TEMABF_4$ solution (up to 3.2–3.4 V) for example C(VC) 900 °C [7, 67, 68, 70, 72–83, 85, 87, 89–92]. The electrolyte composition influence of fluorinated organic compounds addition to PC + 1 M Et_3MeNBF_4 mixture has been tested. It was found that the influence of fluoroethylene carbonate on the PC-based solution was weak in the system containing microporous titanium carbide–derived carbon (TiC-CDC) electrodes [307]. The EDLC cell characteristics based on TiC-CDC electrode and 1 M Et_3MeNBF_4 solutions in PC within a very wide temperature region from − 45 to 100 °C have been tested [308]. The results showed that the region of ideal polarisability decreases if $T > 80$ °C.

Almost simultaneously with the first publications from the Tartu University [67–71], Gogotsi et al. published a paper where CDC characteristics of micro-mesoporous carbon prepared from Ti_3SiC_2 were discussed [309]. Followingly, numerous papers were published, which investigated the parameters of CDCs, which were pepared from boron carbide [310] and ZrC [311, 312]. One of the first papers by Gogotsi et al. in cooperation with P. Simon was published in 2008 [313] that was pursued by a Nature Materials paper in the same year [314], which focused on the influence of carbon micro-mesoporosity onto gas adsorption characteristics. In 2016, Huang et al. [315] demonstrated that the CDC-based EDLCs can be integrated with silicon-based microelectronic devices. In papers [316, 317], more information analysing CDC characteristics in various conditions have been published. One of the shortcomings in the analysis of numerous papers is that the capacitance values have been calculated from the CVs, which are not corrected by ohmic drop. This results in overestimated capacitance and power density values.

The coworkes (A. Jänes, G. Nurk, P. Möller, E. Lust) and Ph.D students (M. Arulepp, L. Permann, M. Lätt) of the Univesrsity of Tartu were also engaged in Tartu Tehnoloogiad AS from 1997 to 2005. In this company, they established a laboratory and participated in the development of electrochemical background of EDLC studies, characterised the CDC materials in non-aqueous electrolytes, and measured the energy/power density characteristics of assembled supercapacitors. Based on the fundamental knowledge and technical information collected, common papers have been published [67–75] and many World and US patent applications have been completed and accepted. Unfortunately at these times, the supercapacitors were too expensive for wide areas technological application. Following the bankruptcy of Tartu Technologies AS at 2009, the supercapacitor development for commercial applications has carried on in Estonia. For example, one of the leading supercapacitor producers in EU, Skeleton Technologies OY has won 2018 SET Awards in "innovative mobility category."

$LiClO_4$, $NaClO_4$, $LiBF_4$, $NaBF_4$, $LiPF_6$, $NaPF_6$, KBF_4, KPF_6, etc., were used to study the influence of electrolyte chemical composition on the electrical double layer parameters in non-aqueous solutions by analysing cation and anion chemical composition and geometric structure [7, 67, 68, 70, 72–83, 86, 87, 92–97, 307, 308]. Very noticeable specific adsorption of Cs^+ cations, as well as weak adsorption of K^+ and Na^+ ions, was observed from non-aqueous solutions using the constant current charging–discharging method [94–97, 307, 308].

For comparison, H_2O-based supercapacitors containing Na_2SO_4, Li_2SO_4, Rb_2SO_4, and $LiClO_4$, $NaClO_4$, etc., have been studied [89]. Due to high hydrogen evolution overvoltage at carbon electrodes, the region of ideal polarisability in H_2O is nearly up to 1.6 V for $Na_2SO_4 + H_2O$. The ideal polarisation region is noticeably narrower for $Rb_2SO_4 + H_2O$ electrolyte due to weak solvation of Rb^+ cations and specific adsorption of Rb^+ at carbon electrodes. Some faradic processes started at higher cell potentials $E > 1.6$ V [89].

For analysis of experimental results, the complex plane plots have been measured and used for the calculation of series capacitance (C_s) and parallel capacitance (C_p) values. If the system is ideally polarisable, then the C_s and C_p are overlapping at low *ac* frequencies, where there is no dependence of C_p or C_s on f [29, 31]. Only these values have been used as the accurate capacitance values [7, 60–65, 67, 68, 70, 72–83, 85–87, 90–97, 105, 300, 306–308] corresponding to limiting Gibbs adsorption values. Collected data show that the C_s values highly depend on the electrode total and meso-microporosity, i.e., on the specific surface area (S_{BET}) and on the DFT total pore volume values, calculated using the 2D-NLDFT-HS model [3]. The C_s values increase with the gas phase activation using CO_2 up to 10 h, but at longer activations, the noticeable decrease of microporous surface area initiates the decrease of C_s and C_p values. The same tendency is valid for materials that were chemically activated with $ZnCl_2$ and KOH. However, it should be noted that only optimal activation times for electrode materials increase the energy densities of EDLCs [305].

The characteristic relaxation times have been calculated using the complex power values ($S(\omega) = P(\omega) + jQ(\omega)$), where active and reactive power are equal to $P(\omega) = \frac{\omega C''(\omega)\Delta E^2_{max}}{2}$ and $Q(\omega) = -\frac{\omega C'(\omega)\Delta E^2_{max}}{2}$, respectively [29, 31]. Data in Table 3 show that characteristic relaxation time depends on the electrolyte viscosity increasing from ACN to PC and further to IL. Very short relaxation times have been calculated for mesoporous carbon EDLCs prepared by the sol–gel syntheses method [90, 91, 306].

The energy density *vs* power density plots (Ragone plots) have been measured using the constant power method

Table 3 Calculated characteristic relaxation time constants (τ_R) for the different electrolyte-based supercapacitors. MPCC denotes microporous carbon cloth

Electrode material	Electrolyte	τ_R [s]	Ref
C(TiC)	1 M Et_3MeNBF_4 in AN	0.8	[68]
C(TiC)	1 M Et_3MeNBF_4 in GBL	2	[68]
C(TiC)	1 M Et_3MeNBF_4 in PC	4	[68]
C(TiC)	1 M $LiBF_4$ in EC + DMC (1:1)	3.2	[93]
C(TiC)	1 M $LiClO_4$ in EC + DMC (1:1)	21.1	[92]
C(TiC)	$EMImBF_4$	3.98	[71]
MPCC	$EMImBF_4$	12	[254]
MPCC	$EMImB(CN)_4$	16	[254]
MPCC	$EMImPF_3(C_2F_5)_3$	27	[254]
MPCC	$EMImN(SO_2CF_3)_2$	8	[254]
MPCC	$EMImN(SO_2F)_2$	17	[254]
C(Mo_2C)	1 M Na_2SO_4 in H_2O	19	[89]
C(Mo_2C)	6 M KOH in H_2O	21	[89]
C(Mo_2C)	1 M Et_4NI in H_2O	21	[89]

[7, 67, 68, 70, 72–83, 85, 87, 89–91, 306]. The energy density increases in a row of solvents PC < GBL < EC + PC < ACN (Fig. 12), from microporous materials to mesoporous and future to sol–gel derived very mesoporous carbon. The energy and power density depend on the cation's chemical composition, and it increases in a row of cations: $Li^+ < Na^+ < K^+ < Rb^+ < Cs^+$ [92–95, 97, 307, 308]. The dependence of energy density on anion composition is more complicated, and with the decrease of cation solvation energy, adsorption activity increases, but for Cs^+, very slow specific adsorption started decreasing the physical adsorption of electrolyte cations due to the blocking effect of the electrode surface with the chemically bonded cations. This effect is heavily dependent on the solvent used.

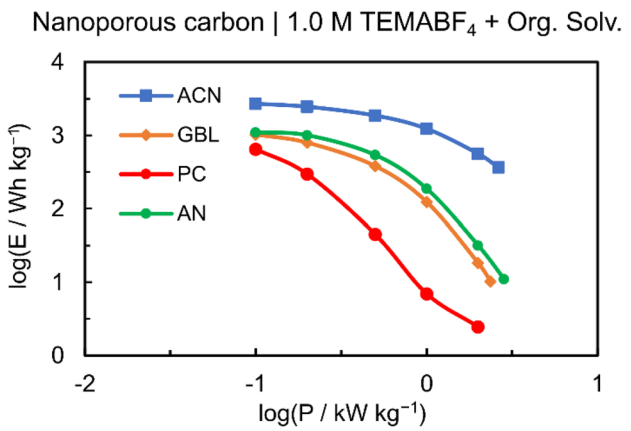

Fig. 12 Ragone plots for the EDLCs in 1.0 M $TEMABF_4$ in ACN, GBL, AN, and PC, highlighting that higher energy and power density can be achieved with other organic solvents than commercially used PC [69]

EDLC in ionic liquids

For the analysis of the influence of IL composition on the region of ideal polarisability, the two-electrode systems have been completed based on various ILs ($EMImBF_4$, 1-ethyl-3-methylimidazolium bis(trifluoromethylsulfonyl) imide (EMImTFSI), 1-ethyl-3-methylimidazolium tetracyanoborate (EMImTCB), 1-ethyl-3-methylimidazolium tris(pentafluoroethyl)trifluorophosphate (EMImFAP), 1-ethyl-3-methylimidazolium thiocyanate (EMImSCN), 1-ethyl-3-methylimidazolium bis(fluorosulfonyl)imide (EMImFSI), etc.), as well as for ILs with the addition of ACN and other solvents [105, 318, 319]. Based on CV and EIS data, the widest region of ideal polarisability was measured for EMImTCB [254] (Fig. 13). It was found that the addition of ACN very slightly decreases (100–200 mV) the region of ideal polarisability compared to pure IL, especially for EMImTCB. EIS data show that in $EMImBF_4$, nearly ideal capacitive behaviour was established up to 3.2 V and only at higher cell potentials a deviation of the ideal capacitive behaviour (phase angles higher than − 88°) takes place. However, the addition of ACN significantly decreases the characteristic time constant values (more than one order), thus increasing the power densities of EDLC remarkably.

To analyse the effect of the carbon electrode, EDLCs based on hierarchical micro-mesoporous sol–gel TiC–derived carbon (SgTiC-CDC) electrodes and $EMImBF_4$ and 1 M $TEMABF_4$ + ACN as the electrolytes were tested

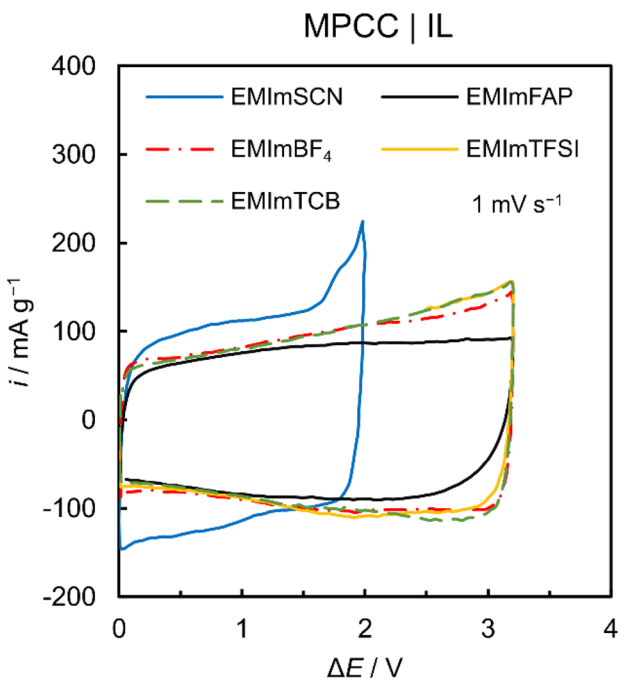

Fig. 13 Cyclic voltammograms for various microporous carbon cloth | IL-based EDLCs (noted in the figure) measured with scan rate 1 mV·s.$^{-1}$ up to 3.2 V [254]

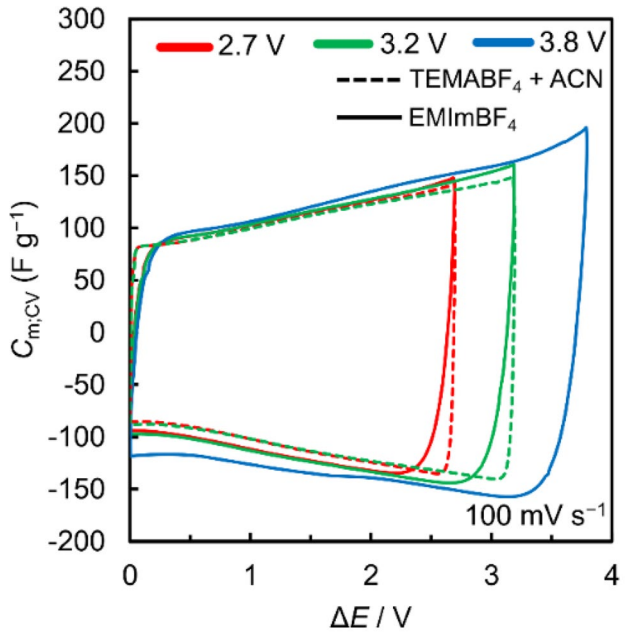

Fig. 14 *C vs E* curves calculated from cyclic voltammograms at various potentials at a scan rate of 100 mV·s.$^{-1}$ in $EMImBF_4$ and $TEMABF_4$ + ACN electrolytes (noted in the figure) [91]

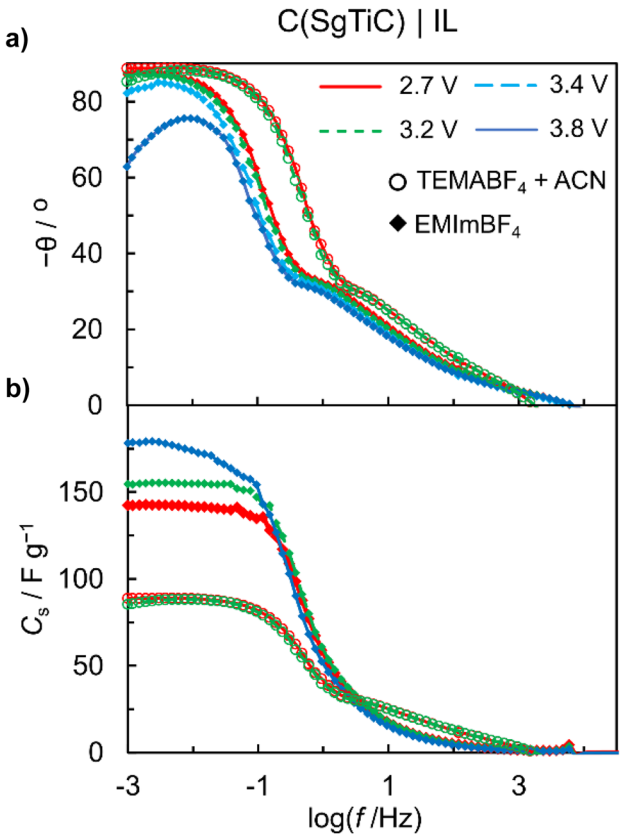

Fig. 15 **a** Phase angle (θ) *vs ac* frequency and **b** specific series capacitance (C_s) *vs ac* frequency dependencies for EDLCs completed with C(SgTiC) electrodes in $EMImBF_4$ and $TEMABF_4$ + ACN electrolytes (noted in the figure) [91]

to establish the electrochemical characteristics and region of ideal polarisability. A very wide region of ideal polarisability (up to 3.8 V) can be achieved if the cell potential limit has been shifted by small potential steps ($\Delta E = 0.1$ V) from 3.4 to 3.6 V and further to 3.8 V (Fig. 14) [91]. This effect has been explained by the dissolution of most active defect amorphous areas of carbon electrodes during the so-called surface passivation (defect and active surface area dissolution) step. Very high capacitance (energy values) values have been calculated for IL-based cells.

The EIS revealed that the high-frequency series resistance depends on the electrolyte applied, and the $R(hf)$ values are nearly one order higher for the $EMImBF_4$-based systems. Additionally, for $EMImBF_4$, the so-called micro-mesoporous mass-transfer area in the Nyquist plot is three times wider than that for $TEMABF_4$ + ACN electrolyte-based EDLCs [91]. The Bode phase angle *vs* log *f* plots show (Fig. 15a) that the characteristic relaxation frequency is one order longer for IL-based EDLCs. The calculated series resistance values are higher than for ACN-based systems (Fig. 15b). Interestingly, the C_s values for ACN are practically independent of the electrode potential applied if the cell potential is around 3 V, indicating that the limiting Gibbs adsorption values have been established. $EMImBF_4$-based EDLCs show that only at very high cell potentials (3.8 V) the limiting Gibbs adsorption (C_s independent of *ac* frequency) has been established.

Additionally, it has been shown that the micro-mesoporous structure, i.e., the ratio of S_{micro}/S_{meso} and V_{micro}/V_{meso}, has a remarkable influence on the limiting capacitance values, characteristic time constants, and real power and imaginary power values if the same electrolyte has been tested [91]. Very short characteristic time constant values have been established for two-electrode cells consisting of mainly mesoporous sol–gel method–derived carbon as a working electrode and $TEMABF_4$ + ACN as an electrolyte. Very long characteristic charging/discharging times were calculated mainly for very microporous α-SiC-derived carbon-based systems. However, the latter systems exhibit high limiting capacitance values and very long characteristic relaxation times, especially in $EMImBF_4$ [91].

It has been shown that the limiting series and parallel capacitance values are higher for ionic-liquid-based EDLC. Nevertheless, the characteristic time constant values are longer than that for ACN-based EDLCs. Thus, the solvent molecules adsorbed at the carbon surface decrease the Gibbs adsorption of ions from ACN-based electrolytes compared with IL data [91].

The constant power discharged method has been applied to analyse energy densities at fixed power density. Data in Fig. 16 show that the highest energy densities have been calculated

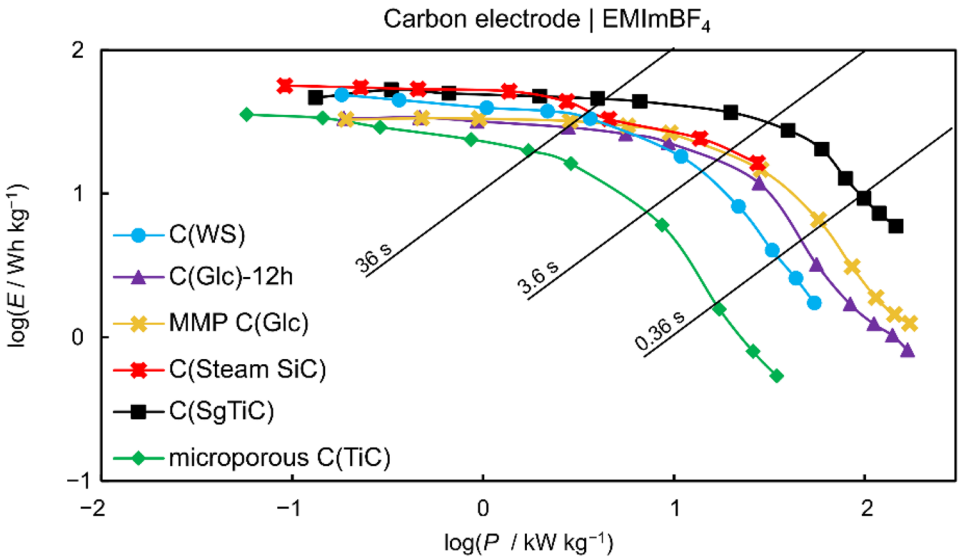

Fig. 16 Gravimetric Ragone plots for different carbon materials (noted in the figure) measured within cell potential range 3.0 to 1.5 V in $EMImBF_4$ electrolyte [91]

with optimal porous structure, i.e., for systems with high microporosity and mesoporosity, prepared using the sol–gel method for syntheses of TiC compared to microporous carbon derived from commercially available TiC, D-glucose-derived carbon (C(Glc)-12 h), micro-mesoporous D-glucose-derived carbon (MMP C(Glc)), steam activated carbon derived from SiC (C(SteamSiC)), and carbon derived from granulated white sugar (C(WS)) [3, 91, 112, 300]. EDLCs with very high microporosity demonstrated moderate or even low power densities and cannot be used as peak power generating devices.

Electropolymerisation of ILs at carbon electrode surface

In order to identify the ideal polarisability region and processes limiting the ideal capacitive behaviour, the $EMImBF_4$-based two-electrode system has been overpolarised [60, 109]. At negative potentials ($E = -2.4$ V), the electroreduction of $[EMIm]^+$ cations takes place, and a cyclic compound is formed, demonstrated in Fig. 17a, experimentally established by FTIR [60] as well as by synchrotron XPS studies [109]. At very positive potentials ($E = 2.0$ V) (three-electrode data), the oxidation (decomposition) of $EMImBF_4$ to $MImBF_3$, CH_3CH_2F, and B_2F_7 takes place, established by XPS studies [108, 320]. For ideal blocking of the carbon electrode surface, the oxidation of butyl methyl propyldicyanamide (BMPDA) to polydicyanamide (polyDCA) has been conducted and demonstrated at the carbon electrode (Fig. 17b) [106]. Very high energy density supercapacitors have been prepared if compared with ceramic, aluminium oxide, and tantalum oxide–based capacitors [106, 107], and this method has been patented in USA and UK [116, 321].

Influence of specifically adsorbing anions onto the EDLC characteristics

For the future increase of the capacitance and energy density of EDLCs, the mixtures of salt and ILs with the

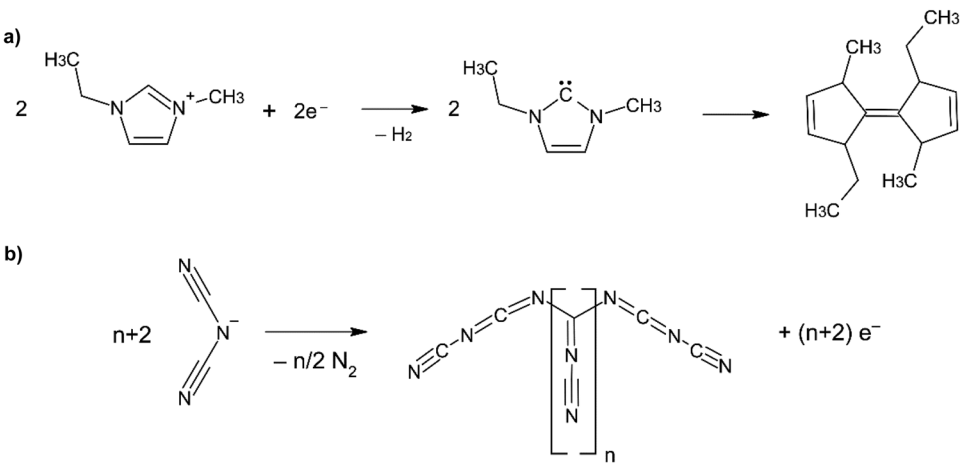

Fig. 17 **a** Proposed reaction scheme for the electroreduction of $[EMIm]^+$ cations [60]. **b** The formation of the carbon–nitrogen polymer from $[DCA]^-$ anion [106]

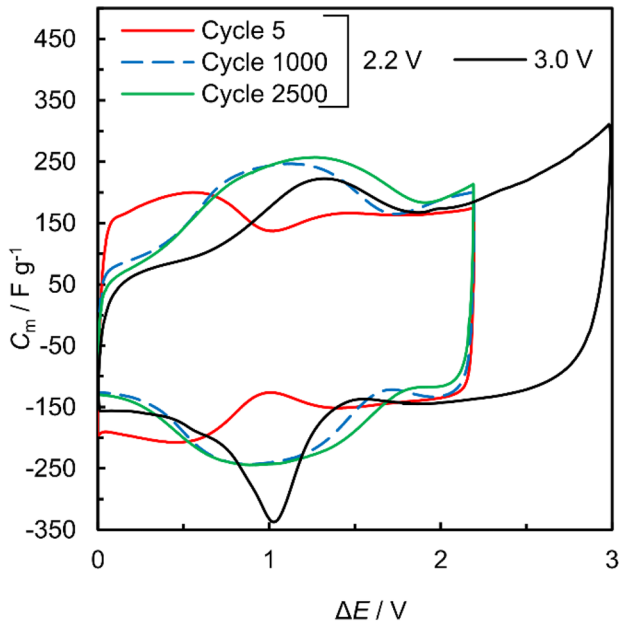

Fig. 18 Cycling voltammetry curves expressed as specific capacitance *vs* cell potential dependencies of electrical double layer capacitors based on microporous–mesoporous carbon electrodes in $EMImBF_4$ + 5% EMImI mixture within different cell potential ranges at potential scan rate 10 mV·s^{-1} [112]

addition of surface-active anions (Cl^-, Br^-, and I^-) have been investigated by Thomberg, Siinor, Siimenson, and Oll [60, 63–65, 100, 112, 113, 304]. Figure 18 demonstrates that the carbon surface is chemically stable and nearly ideally polarisable within cell potential region $\Delta E > 2.0$ V. The given CVs show that the capacitance increases with the cycle number applied up to 1000 cycles, and the future increase of the cycle number does not improve the capacitance values. It is interesting that the charging and discharging cycle capacitance values are nearly the same, indicating the nearly reversible adsorption of I^- at the MMP carbon electrode. However, cycling within a wide potential region indicates that at $\Delta E > 2.4$ V, partial charge transfer takes place (in agreement with synchrotron XPS data at positively charged electrode), and the I_3^- or Br_3^- complex anion formation occurs (discussed by Rogers et al. [115]). In the discharging curve, the reduction current peak is formed; thus, the reduction of the surface compound takes place. It is important to mention that E_{peak}(red) is independent of the potential scanning rate indicating that the limiting step for the reoxidation process (I_3^- to I^-) is the desorption/adsorption rate determined step from the electrode surface [112, 113, 115]. Impedance data indicate that with the increase of the specific adsorption of anions, the characteristic time constant increases, but only nearly 10%. Also, higher E_{max} values have been calculated for electrolytes with the addition of I^- in IL mixture than the values calculated for surface-inactive $EMImBF_4$.

A noticeable increase in energy densities accumulated by the adsorption of halide anions has been demonstrated for two-electrode single cells at moderate power densities. Very high E_{max} values have been established at lower power density Ragone plot region, where the E_{max} is 20% higher than that for $EMImBF_4$-based EDLC. However, a quicker decrease of E_{max} takes place at very high power densities compared with EDLCs based on surface-inactive electrolyte solutions [112, 113]. The energetic efficiency of supercapacitors containing specifically adsorbing anions is lower than for surface-inactive IL–based EDLCs due to the partial charge transfer between carbon surface and adsorbed anions.

Influence of membrane parameters on EDLC characteristics

The influence of separator characteristics on the two-electrode supercapacitor cells has been studied using standard (TF-4425 from Nippon Kodoshi, Japan; Cellgard Japan) and self-made polyvinylidene difluoride (PVDF) separators [99, 117, 118, 120–123]. PVDF was dissolved in dimethyl formamide, and used in the electrospinning method at different electric field strengths (10–40 kV·m^{-1}), spinning rates, polymer pressing out rates, etc., have been used for the preparation of membranes with different thicknesses, densities, total porosity, etc. [99, 117, 118, 122, 123].

The influence of polymer membranes' geometrical structure, thickness, and porosity values on EDLC parameters has been analysed by Thomberg et al. [99, 117, 118, 122, 123] using the EIS method for cells with various membranes. The characteristics of membranes have been established using the Hg intrusion porosimetry measurement method and BET gas adsorption methods [99, 117, 118, 122, 123]. The EIS data show that the very high-frequency series resistance value depends on the micro- and mesoporosity (hierarchical porosity parameters) of the membrane used. The characteristic relaxation frequency values, given in Table 4, noticeably depend on the membrane thickness selected for the completion of two-electrode cells. Therefore, the power density of a two-electrode supercapacitor cell depends strongly on the micro-meso-macroporosity of the membrane separating the positively and negatively charged electrodes. The low-frequency parameters are also influenced by high-frequency resistance R_s values, but this influence is moderate compared with that observed within the high-frequency (high power density) region. However, for extremely high power density supercapacitors, the optimisation of membrane porosity (ion–ion transfer resistance within the membrane) is extremely important. A more detailed discussion is given in [99, 117, 118, 122, 123].

Table 4 The parameters of different poly(vinylidene fluoride) separator materials prepared using electrospinning, as discussed in [118], and measured in a system consisting of C(TiC) electrodes and 1 M $TEMABF_4$ + ACN solution. The specific surface area and total porosity were determined using mercury intrusion porosimetry. The characteristic time constant is noted with τ_R

Membrane material	Thickness of membrane [μm]	Porosity [%]	S_{Hg} [$m^2 \cdot g^{-1}$]	E_{max} [Wh kg^{-1}]	P_{max} [kW kg^{-1}]	τ_R [s]
TUX1	15	42	21.15	34.4	179	0.84
TUX3	33	42	21.15	34.5	146	1.22
TUX5	10	18	56.00	35.3	264	0.64
TUX6	15	22	50.30	34.9	256	0.58
TUX7	26	23	37.84	34.6	159	1.01
TUX8	38	30	32.25	33.3	180	0.71

For comparison, the same electrode systems have been completed using the $EMImBF_4$ as an electrolyte and serial-produced membranes TF4425, etc. A comparison of data with standard separator TF4425 based cells shows that even higher power densities have been achieved for well-optimised membranes made in University of Tartu. Therefore, similarly to organic electrolyte–based systems, optimisation of membrane characteristics is very important for IL-based EDLCs, and as for EDLCs containing thick membranes (TUX 5), very low power densities were measured [99, 117, 118, 120–123].

Hydrogen and methane adsorption at carbon materials and thin-film complex metal hydrides

Hydrogen and methane adsorption in different CDCs: C(TiC) 950 °C, C(SiC) 1000 °C, $C(Mo_2C)$ 900 °C, with well-defined pores and different sizes and shapes, volumetric adsorption has been studied using in situ quasi-elastic neutron scattering methods by Härmas et al. [133], Koppel et al. [134], Palm et al. [135]. The predominant shape of pores for three of these carbons (spherical-C(SiC) 1000 °C, cylindrical C(TiC) 1000 °C, and slit-like $C(Mo_2C)$ 900 °C) has been established using the small angle neutron scattering method [128]. In addition to the strong effect of the presence of sub-nanometre pores, as in the case of C(TiC) 950 °C and C(SiC) 1000 °C, the effect of the pore shape on the diffusion coefficient of hydrogen has been observed and discussed. While the C(TiC) 950 °C and C(SiC) 1000 °C have the same, nearly similar pore size distributions, the prevalently shaped pores in C(SiC) 1000 °C restrict the diffusion of H_2 to a large degree in comparison with C(TiC) 950 °C. In the case of low H_2 loading pressure, no mobile H_2 was detected in C(SiC) 1000 °C, but the H_2 mobility has been demonstrated for C(TiC) 950 °C. It was found that the prevalently slit-shape and large pores for $C(Mo_2C)$ with flatter pore potential enabled a higher mass-transfer processes rate for confined hydrogen molecules and therefore exhibited weaker interaction between hydrogen molecule and adsorbing carbon surface. The observed molecular behaviour of hydrogen confined into micropores of C(SiC) 1000 °C, C(TiC) 950 °C, and in $C(Mo_2C)$ 900 °C allowed the explanation of differences in gas adsorption isotherms, given in Fig. 19, where it is visible that C(TiC) has a microporous structure and $C(Mo_2C)$ has a micro-mesoporous structure with well-expressed hysteresis in BET gas sorption curves [3]. The best fit of the experimental data for C(TiC) and $C(Mo_2C)$ has been established using the Aspect ratio 6 model or heterogeneous surface model [293–295].

The localisation and low mobility of H_2 in sub-nanometre pores lead to higher gas adsorption (intake) at lower pressures. Higher pressure needs to be applied to confine H_2 in pores with flatter surface potential and weaker interactions between adsorbate and adsorbent, i.e., mainly the influence of H_2 pressure and the interaction of H_2 with $C(Mo_2C)$ have been analysed. It is shown that the increase in H_2 pressure and the amount of confined H_2 molecules leads to the increase in cooperative molecular interactions. A similar effect has been observed for H_2 adsorbing in zeolites, and the establishment of this effect for very weakly adsorbing H_2 molecules suggests the universal character of the phenomenon discussed [136, 322].

A detailed analysis of the porosity and solid base geometrical structure of different CDCs (α-SiC, TiC, Mo_2C) (Fig. 19b) and peat-derived carbons has been conducted for moderate temperature and pressure. It was found that the hydrogen adsorption in non-modified CDC carbons decreases in order: α-SiC, TiC, Mo_2C and thus with the decrease of microporosity. For fixed Mo_2C carbons as well as for α-SiC-derived materials, H_2 adsorption decreases with the increase of carbon syntheses temperature, thus with the increase of mesoporosity, and decrease of microporosity.

SANS, QENS, and INS data indicate that the carbon surface roughness influences the specific interaction of hydrogen, porous structure, tortuosity, etc., which has been discussed in [129, 130, 132, 134]. The decisive influence of CDC crystallographic structure (cubic, tetrahedral, rhombic, and hexagonal) on the CDC carbon structure synthesised has been investigated.

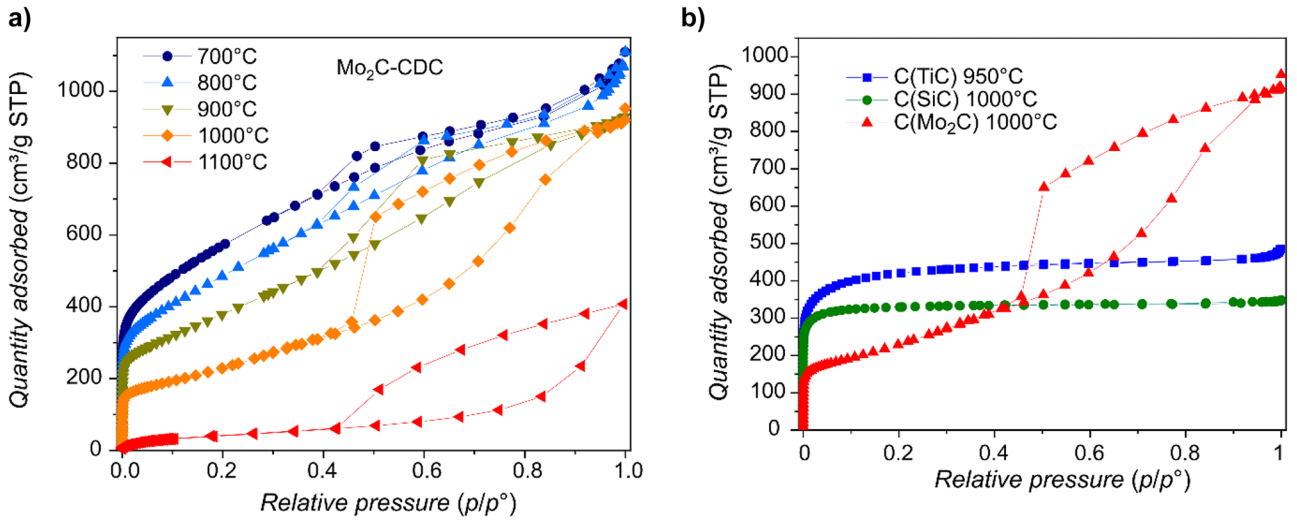

Fig. 19 **a** N_2 adsorption isotherms of carbons derived from Mo_2C at different temperatures (noted in the figure) and **b** N_2 adsorption isotherms of different carbide-derived carbons (noted in the figure) [132, 135]

It was demonstrated by SEM, HR-TEM, AFM, and FIB-TOF–SIMS methods that the ball-like shape of pores prevails on/in CDC prepared from α-SiC, cylindric from TiC, and slit-shape pores in carbon prepared from Mo_2C. Additionally, they have very different characteristic relaxation times and power densities increasing from C(α-SIC) to C(Mo_2C). The QENS and INS studies of molecular hydrogen adsorption verified complicated adsorption/desorption kinetics of materials with different porous structures of hydrogen at very low temperatures (− 253 °C) [133, 134, 136].

The adsorption of methane also depends on the structure of the porous carbon, increasing with the increase of microporosity from C(α-SiC) to C(TiC) and lastly to C(Mo_2C). The effect of pore size and surface morphology of carbon materials on the adsorption of methane was studied using C(TiC) 950 °C and 1100 °C, and C(Mo_2C) 1000 °C materials. Nitrogen adsorption, Raman spectroscopy, and XRD have been used for the characterisation of methane adsorption. All materials have a high specific surface area: C(TiC) 950 °C, 1450 $m^2 \cdot g^{-1}$; C(TiC) 1100 °C, 870 $m^2 \cdot g^{-1}$; and C(Mo_2C) 1000 °C, 820 $m^2 \cdot g^{-1}$, but the pore size distribution depends strongly on the synthesis temperature and the applied activation method. C(TiC) 950 °C contains mainly micropores, C(TiC) 1100 °C, activated with HCl, contains micro- and mesopores with a pore size distribution maximum from 1.5 to 5 nm, and C(Mo_2C) 1000 °C is mainly mesoporous from 2.4 to 10 nm. The methane adsorption increases from C(Mo_2C) to C(TiC) 950 °C, being 165 $cm^3 \cdot g^{-1}$ and 295 $cm^3 \cdot g^{-1}$, respectively. Excess isotherms of methane adsorption were measured at different temperatures from − 100 to 40 °C and pressures from 0.35 to 1.35 MPa and modelled enthalpies and entropies of CH_4 adsorption. It was found that the changes in entropy are the key factor determining the amount of CH_4 adsorbed per unit surface area of CDC. It was established that up to 55% more methane can be adsorbed in C(TiC) 950 °C, compared with C(Mo_2C) 1000 °C if the carbon structure is optimised [135].

For higher hydrogen adsorption values, the MMP carbon electrodes have been modified with thin films of $NaAlH_4$ [323]. Differently from homogenous $NaAlH_4$ solid particles (7.5 wt% of H_2 per 1 g $NaAlH_4$), the release of hydrogen started at moderate temperatures (60–80 °C) differently from monolithic materials where H_2 evolution started only at 240–280 °C. It means that the thin-film hydrogen storage materials can be used for the release of hydrogen using the heat generated by the PEMFC stack when it generates electricity for *ac* motors. It is great to point out that the hydrogen adsorption capacity in thin-film $NaAlH_4$ is nearly 3–3.5 times bigger than that for MMP carbons (up to 2.5–3.0 wt%). In addition, the gravimetric hydrogen capacity is 4–5 times bigger than that for compressed hydrogen up to 700 bar, as well as nearly two times larger than for liquefied hydrogen. It should be stressed that the adsorption/desorption of hydrogen into nanostructural $NaAlH_4$ is an energy-efficient process compared with the liquefaction of hydrogen.

Development of carbon materials for Li^+-ion and Na^+-ion batteries

The carbon materials synthesised from different raw materials (from carbides (CDC), glucose (glucose-derived hard carbon, HC(Glc)), and Estonian well-decomposed peat

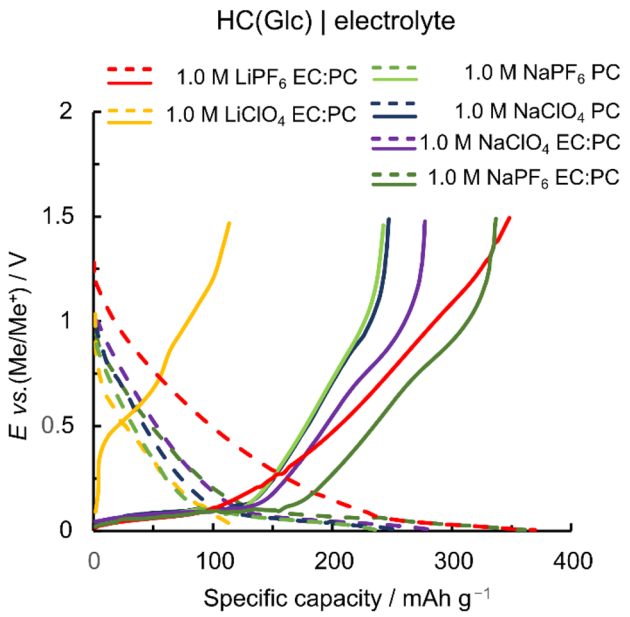

Fig. 20 Galvanostatic charge/discharge profiles measured at 50 $mA{\cdot}g^{-1}$ current density for half-cells based on Li^+- and $Na.^+$-ions in different electrolytes, marked in the figure [97]

(peat-derived hard carbon, HC(EP)) at different syntheses temperatures from 1200 to 1700 °C have been used as negatively charged electrodes for LIBs and SIBs, where Li metal and Na metal have been used as positively charged electrodes, respectively. Very open porous 3D structures (S_{BET} up to 1100 $m^2{\cdot}g^{-1}$ for HC(Glc) and 1050 $m^2{\cdot}g^{-1}$ for HC(EP)) with a partially graphitised curved graphitic surface, established by Raman spectroscopy, have been prepared. The partial graphitisation of HC(Glc) and HC(EP) is very important, giving materials under study good electrical conductivity compared with amorphous non-graphitised carbons [92–94, 96, 97, 299–303].

Due to the low graphitisation level of CDC and not partially graphitised carbons like HC(Glc), white sugar–derived hard carbon (HC(WS)), or HC(EP) carbons, the adsorption capacity values for Li^+ are only moderate and mentioned CDC could not be used for high energy density LIBs. Surprisingly high capacities have been observed for glucose, and peat-derived carbons, even up to 320–360 $mAh{\cdot}g^{-1}$, thus showing very promising high capacity values (Fig. 20). The limiting capacity values depend on the electrolyte (salt and solvent) used. The highest capacity values have been calculated for $NaPF_6$ electrolyte solutions dissolved in EC + PC 1:1 mol/mol mixed solvent system at a 50 $mAh{\cdot}g^{-1}$ charging rate. An increase in the PC molar ratio in the mixed solvent system also decreases the limiting capacity of negatively charged electrodes. The exchange of $NaClO_4$ to $NaPF_6$ increases the capacity values notably [303]. It should be noted that for C(EP), there is no noticeable dependence of limiting capacity values on the chemical nature of the cation tested, i.e., for $LiBF_4$ and $NaBF_4$, as well as for $LiClO_4$ and $NaClO_4$; nearly comparable high capacity values (320–360 $mAh{\cdot}g^{-1}$) have been established.

These systems have been studied using different *operando* testing methods, including XPS, XRD, AFM, and FIB-TOF–SIMS. It is interesting that the 20% larger Na atoms compared with Li atoms adsorption onto HC(Glc) surface causes a 60% increase in in-plane bond lengths values, established by *operando* X-ray total scattering study of HC(Glc) in Li^+-ions and Na^+-ions containing solutions [8, 131]. Thus, the Na adsorption to the surface or intercalation between the HC(Glc) graphitic layers could affect the neighbouring π-electron graphitic electron systems. Sodiation causes an increase in interlayer distances in the charging curve sloping region, characterising the different intercalation/charge collection mechanisms for Li^+- and Na^+-based systems [131]. FIB-TOF–SIMS data show that the surface chemistry for Li^+-ions containing electrolytes is more complicated than that for Na^+-ions containing systems. Therefore, at the carbon electrode surface in Na^+-ions containing electrolytes, there is no dense blocking SEI differently from Li^+-ions containing solutions. It was observed that the Na adsorption capacity depends very strongly on the hard carbon syntheses temperature, and the highest capacity values have been established for HC(Glc) and HC(EP), synthesised at 1400–1500 °C.

The accumulation of Li^+-ions (formation of Li) and Na^+-ions (Na) into hard carbon materials is very slow, and maximal capacity (maximal faradic current density) values have been calculated only at a very slow potential scanning rate (0.1 $mV{\cdot}s^{-1}$). The cyclic stability (so-called cyclability) of HC(Glc) is good, and after 80 cycles, the capacity stabilises at 160 $mAh{\cdot}g^{-1}$ level (at a high charging rate of 50 $mA{\cdot}g^{-1}$ applied). The charging Coulombic efficiency after the preliminary 10 cycles increases up to 98%.

Thus, based on the results collected for the three-electrode cell, it was decided to complete the two-electrode cells with real positively charged electrodes. The two-electrode cell capacity, containing HC(Glc) or HC(EP) and Li^+-ions or Na^+-ions electrolytes, is limited by the capacity of positively charged electrodes, and future studies are inevitable for completing high power density SIBs. At the moment, Na^+-ions–based electrolyte systems can be used for stationary electricity storage only, where the capacity values (stored energy per g of device) of devices are not critical, and the cheap prize of SIBs is more important than the high volumetric or gravimetric density of devices.

The development of Pt-metal-nanoclusters activated and d-metal-nitrogen active centres based electrocatalysts for PEMFC electrodes and PEM single cells

Preparation and physical characterisation of Pt and Ru modified catalysts

Various micro-mesoporous carbons have been used as carbon supports for oxygen electroreduction and PEMFC single-cell studies. These carbon materials have been prepared from carbides [4, 138–148, 151–153, 155, 162–170, 324–326], glucose solution [149, 150], and from Estonian well-decomposed peat [137, 154, 156, 157]. The materials were activated using different methods, e.g., with CO_2 gas (at different temperatures and for different durations of 1–12 h), $ZnCl_2$, or KOH powders. Most of the carbons were post-treated with molecular hydrogen (at $T = 800$ °C for 2–6 h). Pt and Ru, Pt-Ru, Pt-Ir alloys [148, 169] nanoclusters were deposited on the supports using mainly the $NaBH_4$ reduction method. $H_2PtCl_6{\cdot}xH_2O$, $RuCl_3{\cdot}xH_2O$, and $IrCl_3{\cdot}xH_2O$ have been used as metal donors for the deposition of metal nanoclusters onto various MMP carbon supports, i.e., C(Mo_2C) (600–1200 °C), C(VC) (900–1200 °C), C(WC) (900–1100 °C), C(TiC) (800–1200 °C), C(SiC) (900–1100 °C), and C(Cr_3C_2). In addition to the self-made carbons, the traditional Vulcan XC72R and Ketjenblack carbon powders have been used to see how the carbon support structure, specific surface area, hierarchical porosity, graphitisation level, the ratio of microporous surface area to mesoporous surface area, and the ratio of mesopore volume to micropore volume influence the oxygen electroreduction rate in acidic and alkaline aqueous electrolyte solutions. Thus, the same carbon supports, tested in EDLCs and hybrid capacitors, have been used.

The catalyst suspension consisting of catalyst, Nafion solution, MilliQ$^+$ water, and isopropanol was used for preparing thin-film electrodes. For some electrodes, ultrasonic spraying has been used.

For the analysis of materials, the HR-TEM, FIB-TOF–SIMS, FIB-SEM–EDX, XRF, XPS, and XRD studies have been conducted. The results indicate that a nearly homogeneous distribution of Pt and Pt-Ru nanoclusters has been achieved (Fig. 21).

Very well-oriented single-crystal Pt areas have been deposited onto well-treated C(Mo_2C) supports. The systematic analysis of materials indicates that depending on the deposition conditions, Pt nanoparticles with different ratios of facets ((111), (100), (011), (321), and (331)) have been deposited (Fig. 21a). The single-crystal areas are nearly 4–14 nm wide. The porosity characteristics have been measured by the nitrogen gas adsorption method (discussed above). It should be mentioned that after the deposition of Pt, the Pt-C(Mo_2C) has a hierarchical structure like that of the carbon support with well-expressed mesopores and micropores at the surface (Fig. 22a). The same is valid for glucose solution derived carbon materials activated with Pt clusters, noted as Pt-C(Glc) (Fig. 22b).

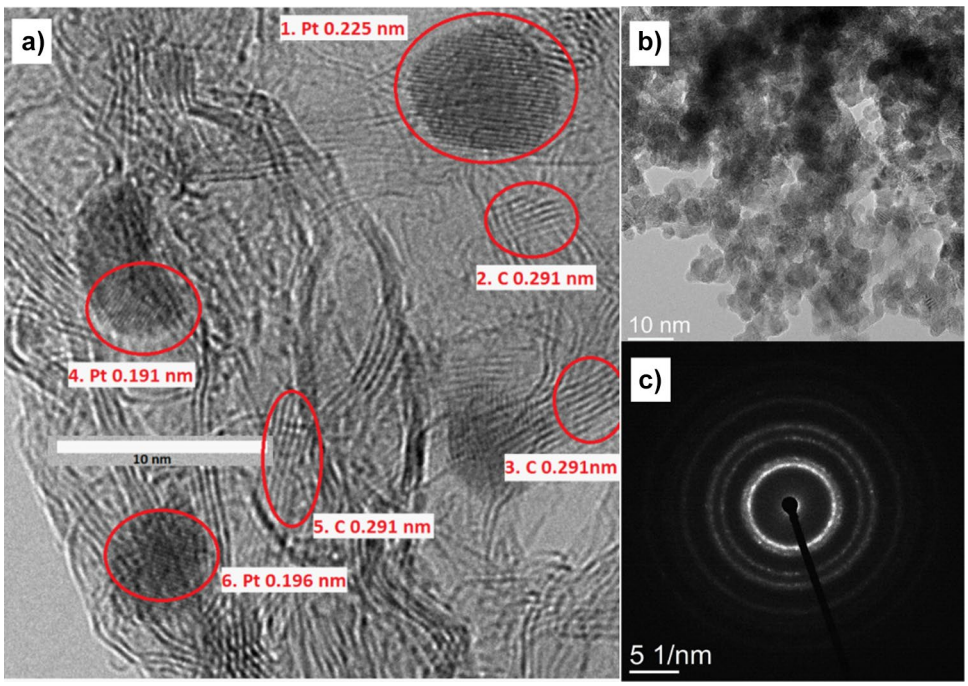

Fig. 21 HR-TEM images for **a** Pt–C(Mo_2C) 800 °C and **b** Pt–Ru–C(Mo_2C) 600 °C catalysts; **c** SAED image of Pt–Ru–C(Mo_2C) 600 °C catalyst [165, 168]

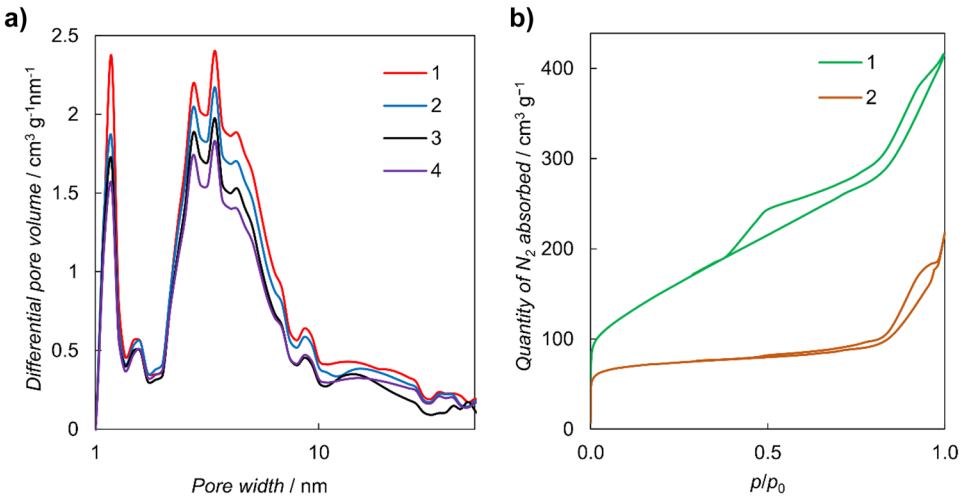

Fig. 22 **a** Dependence of the differential pore volume on the pore width for various catalysts: 1 — C(Mo_2C) 750 °C; 2 — 3.5 wt% Pt-C(Mo_2C) 750 °C; 3 — 8.3 wt% Pt-C(Mo_2C) 750 °C; 4 — 12.4 wt% Pt-C(Mo_2C) 750 °C and **b** low-temperature nitrogen adsorption/desorption isotherms for the catalyst powders: 1 — 60 w% Pt-C(Mo_2C) 800 °C and 2 — 60 wt% Pt-C(Glc) [325]

Oxygen reduction data on platinum-based catalysts in acidic and alkaline electrolyte solutions

The cyclic voltammetry and rotating disc electrode methods were used to characterise the oxygen reduction reaction (ORR) kinetics. There are very well-developed surface oxygen compounds' reduction peak at 0.8 V and hydrogen evolution peaks at 0.25 and 0.1 V (*vs* SHE) for Pt-C(Mo_2C) electrodes in cyclic voltammograms (Fig. 23a) in 0.5 M H_2SO_4 saturated with Ar at electrode potential rate

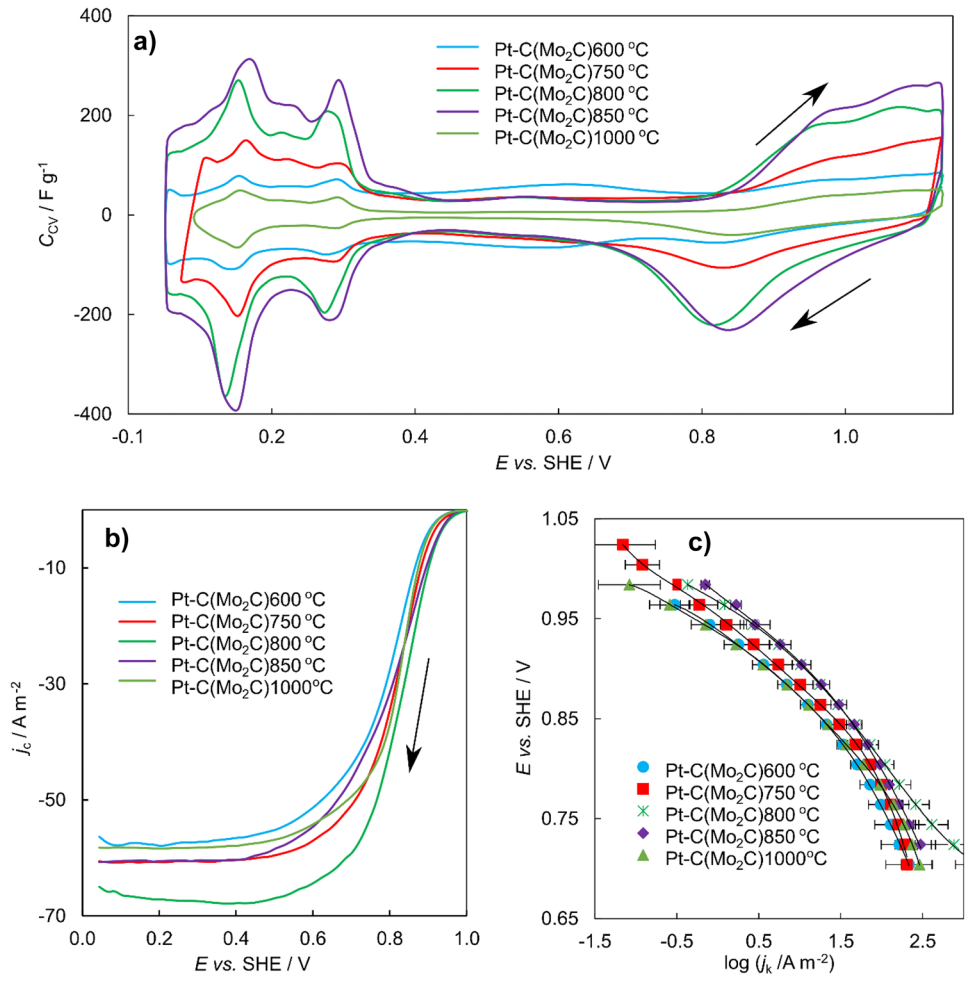

Fig. 23 **a** Calculated capacitance C_{CV}, *E* plots for Pt-C(Mo_2C) electrodes (noted in the figure); **b** RDE data for Pt-C(Mo_2C) electrodes at 3000 rev·min.$^{-1}$ in 0.5 M H_2SO_4 solution saturated with O_2; **c** corrected Tafel plots calculated from RDE data (noted in the figure) [4]

10 mV·s^{-1}. It should be stressed that the carbon structure, specific surface area, the ratio of micro/mesopores surface area and volume, and the existence of the graphitised surface structure of catalysts have a great impact on the deposition of the Pt nanoparticles. It is interesting that the hydrogen adsorption/desorption peak potentials are nearly independent of the micro-mesoporous structure of the carbon support material used, indicating that the reaction rate is mainly controlled by the Pt nanoclusters activity deposited onto carbon C(Mo_2C) support. The intensity of cyclic voltammetry peaks corresponding to the adsorption/desorption of O_2 (oxygen-containing surface compounds) and H_3O^+ ions (kinetics) depends on the micro/mesoporosity ratio and graphitisation level of supporting carbon structure. Data in Fig. 23a show that the hydrogen adsorption/desorption rate has maximum values for Pt-C(Mo_2C) 850 °C. Thus, for moderately microporous carbon supports [139, 141, 142, 162, 163, 170], the rate of mass transport in micropores seems to be quite slow. There is only a very weak dependence of adsorption/desorption peak potentials as well as peak current densities on the potential scanning rate, indicating that the adsorption/desorption step rate limited processes prevail at Pt-C(Mo_2C) electrode surfaces in a solution saturated with argon. Very high electrochemical surface area values have been calculated (from 14 to 30 m^2·g^{-1} for Pt-C(Mo_2C) 700, 750, 800, and 850 °C) [4], indicating that optimal micro/mesoporous structure is important for high O_2 reduction kinetics in order to avoid the accumulation of H_2O_2 (including other intermediates) and H_2O into micropores, observed for Pt-C(Mo_2C) 600 °C catalyst with high microporosity, but with low mesoporosity.

The ORR for Pt-C(Mo_2C) catalysts is demonstrated in Fig. 23b. The O_2 reduction kinetics is highest at Pt-C(Mo_2C), where Pt was deposited onto carbon synthesised at 750–850 °C. These materials also demonstrate the best supercapacitors' energy density *vs* power density characteristics [3]. It is interesting that for the Pt catalysts synthesised using other CDC supports, i.e., C(VC), C(WC), C(TiC), and C(SiC), there is a very weak dependency of ORR rate on the carbon support micro-mesoporosity characteristics under study explained by the catalytic role of the structure of Pt nanoclusters deposited.

Taleb et al. studied ORR kinetics at Pt catalysts deposited onto HC(Glc) in acidic and alkaline media and came to the same conclusion [149]. The electroreduction of oxygen is quite a complicated process, and it depends on the nanocrystal surface structure of the Pt particles [140]. Based on the HR-TEM data, all basal planes (111, 001, 011) and catalytically more active high-index Pt planes (311, 211, 331, etc.) have been observed at Pt-C(Mo_2C) surface in agreement with XRD and HR-TEM-SAED data [138, 143, 145]. It should be noted that for some mainly microporous CDC (no hysteresis in BET adsorption data), there is only a very weak dependence of oxygen reduction rate on the surface structure (like for C(WC), C(VC), C(Cr_2C_3)). Thus, it can be concluded that the Pt-carbon electrodes with macro-heterogeneous porous structure, combined with hierarchical micro-mesoporous structure, have demonstrated the quickest catalysis of O_2. The rotating disk electrode (RDE) data show that nearly Levich and Koutecky–Levich models [327] can be applied for the mathematical analysis of experimental data in spite of crystallographic inhomogeneous and surface roughness of Pt-nanoclusters activated electrodes. It seems that the catalytically active Pt centres can be found only at the open surface regions, where the oxygen reduction takes place [142, 163]. Therefore, for more active catalysts, the mesoporous and microporous carbon supports with high mesopore volume, giving more attainable catalytic centres per flat-gross section surface area, could be created for more high energy and power density PEMFCs.

The kinetic current densities (Fig. 23c) have been calculated using a modified Koutecky–Levich method [327, 328]:

$$\frac{1}{j} = \frac{1}{j_k} + \frac{1}{j_d} + \frac{1}{j_f} = \frac{1}{j_k} + \frac{1}{0.62nFD^{\frac{2}{3}}\nu^{-\frac{1}{6}}c_0\omega^{\frac{1}{2}}} + \frac{L}{nFc_fD_f}, \quad (8)$$

where j_k, j_d, and j_f are kinetically limited, diffusion-limited, and Nafion film diffusion-limited current densities, respectively. In addition, the remaining variables are B — Levich constant, c_0 — the O_2 concentration in the solution, L — the film thickness, c_f — the O_2 concentration in Nafion film, D — the O_2 diffusion coefficient in the electrolyte, and D_f — the O_2 diffusion coefficient in the Nafion film.

The role of the third component, i.e., processes in the Nafion layer, is unimportant as the j_f values are very high in comparison with kinetic current values j_k for the electrodes studied in our works [170, 324] (like it was established by Paulus et al. [328]). For well-optimised electrodes, the number of electrons transferred is nearly 4 [4, 137, 139, 140, 145–147, 149, 152, 154, 155, 165, 167–170], indicating that the formed H_2O_2 reduces to the final product in acidic electrolyte solutions. However, for less meso-macroporous electrodes, the number of electrons transferred is lower than 3.5 (or even lower than 2.9), and the reaction is not going to the end and some intermediate products (H_2O_2) form, blocking the active electrode surface and lowering the diffusion-limited currents, observed experimentally at very many microporous electrodes at very high negative potentials, where the oxygen reduction faradic charge transfer step is not limiting process any more, but ORR is controlled by adsorption/desorption kinetics inside of the limiting diffusion (mass-transfer) layer.

The influence of Pt loading on the ORR has been studied using C(Mo_2C) 750 °C (Pt-C(Mo_2C)) and C(Vulcan) as supports (noted as Pt-C(V)) [140, 141, 143]. Electroreduction of oxygen has been studied at catalysts with very low Pt loading

[141, 143, 324, 325] 3.5–20 wt% and small Pt nanoparticles (linear dimension from 2 to 5 nm) deposited onto C(Mo_2C) support. Pt has been deposited by the $NaBH_4$ method, and the well-crystallised Pt nanoparticles with increasing reflex intensity with the increased amount of Pt have been prepared and confirmed by XRD. The Pt particle size increases from 2.6 to 3.4 nm with the increase of Pt wt% in the catalyst, according to HR-TEM histograms in Fig. 24.

The gas adsorption data analyses indicate that with the increase of Pt wt%, the S_{BET} (multipoint analyses method) noticeably decreases from 1942 to 1672 $m^2 \cdot g^{-1}$ with a well-expressed mesoporous and microporous structure. The ORR polarisation curves for Pt-modified C(Mo_2C) catalysts demonstrate that the 8 ± 1 wt% Pt loading is optimal. Somewhat higher ORR activity has been measured for 0.1 M $HClO_4$ solutions compared with the 0.05 M H_2SO_4 solution, and the lowest activity was observed for 0.1 M KOH solution (Fig. 25). The Pt mass corrected current $|j_{Pt}|$ decreases with the increase of Pt wt% in the catalyst [143].

The calculated Tafel-like plots were linear within a narrow potential region with the Tafel slope values somewhat decreasing (independent of the chemical composition of acid) with the increase of Pt wt% deposited onto carbon support. However, for KOH solutions, the lower Tafel plot slope values have been established. The change in the Tafel slope value can be attributed to a change from the Langmuir ORR mechanism at low current densities to a more complicated mechanism in the high current density region [329, 330].

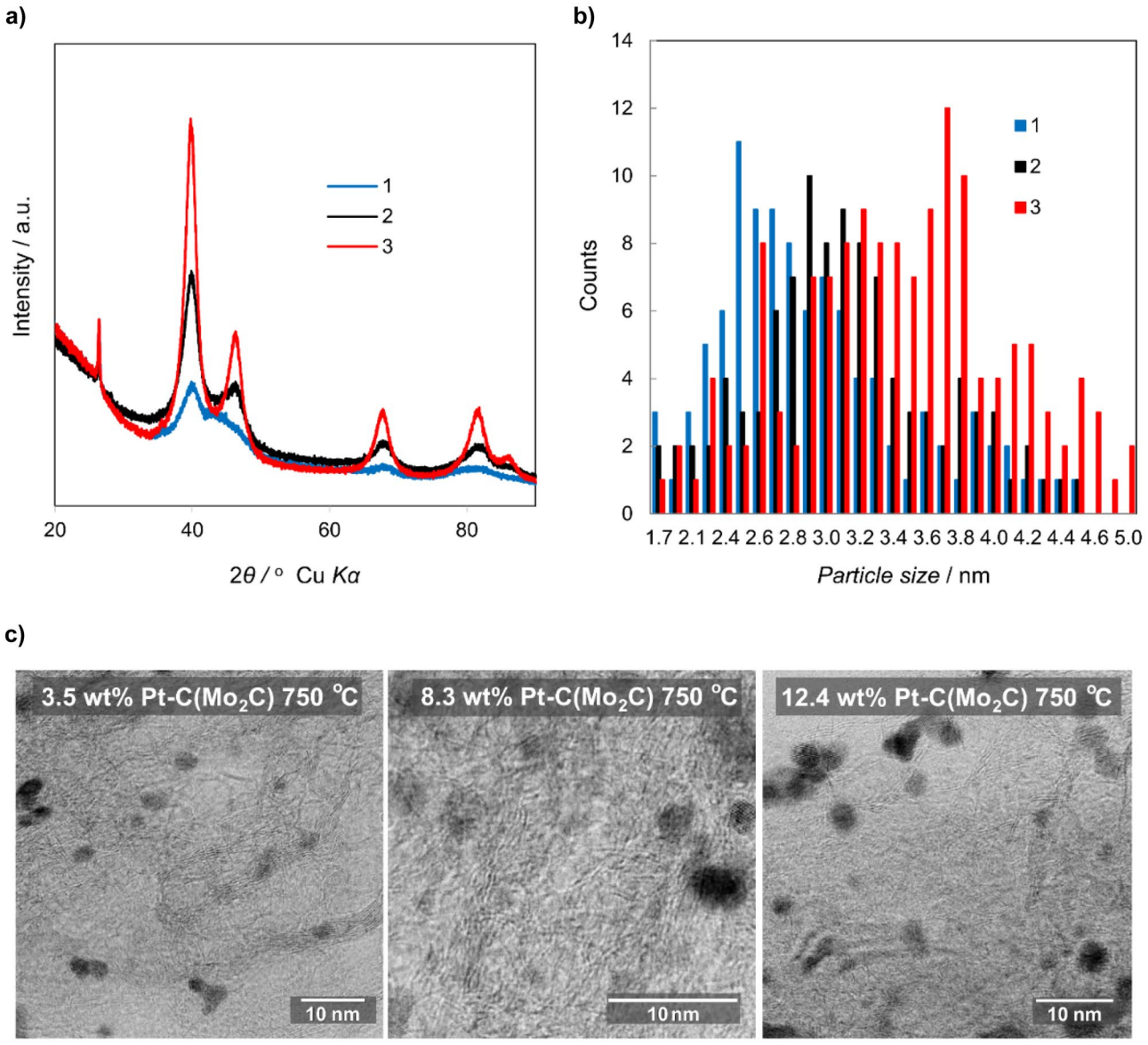

Fig. 24 **a** X-ray diffraction data and **b** HR-TEM histograms for various Pt catalysts: 1 — 3.5 wt% Pt-C(Mo_2C) 750 °C; 2 — 8.3 wt% Pt-C(Mo_2C) 750 °C; 3 — 12.4 wt% Pt-C(Mo_2C) 750 °C; and **c** HR-TEM images (noted in the figure) [325]

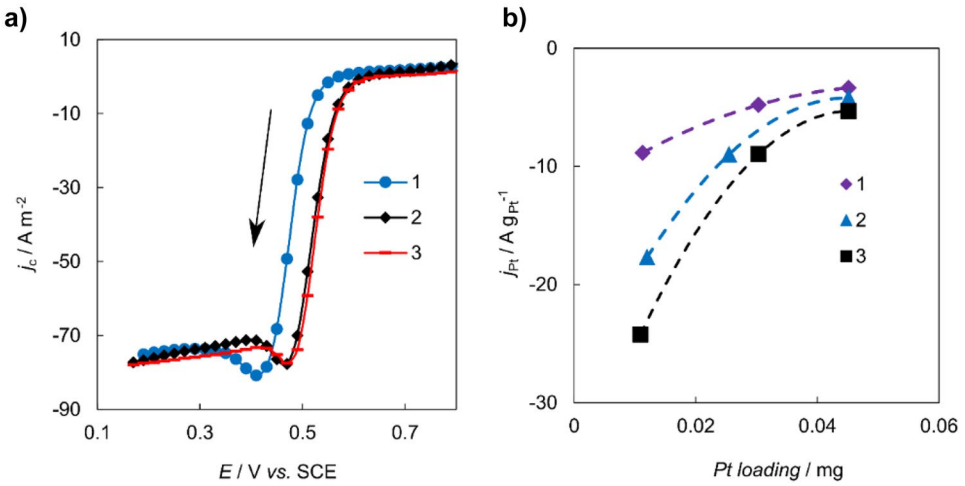

Fig. 25 **a** Polarisation curves for Pt catalysts: 1 — 3.5 wt% Pt-C(Mo_2C) 750 °C; 2 — 8.3 wt% Pt-C(Mo_2C) 750 °C; 3 — 12.4 wt% Pt-C(Mo_2C) 750 °C in 0.1 M $HClO_4$ electrolyte solutions saturated with O_2 at $v = 10$ mV·s^{-1} and at electrode rotation rate 3000 rev·min^{-1} [325]; **b** dependence of the Pt mass corrected current (j_{Pt}) on the Pt loading in a catalyst in various electrolyte solutions: 1 — 0.1 M KOH; 2 — 0.05 M H_2SO_4; 3 — 0.1 M $HClO_4$ (j_{Pt} values were obtained from cyclic voltammogram at onset potential at $v = 5$ mV·s^{-1})

In addition to Pt wt% in the catalyst, the effect of catalyst loading on the ORR activity was investigated [326]. The 20 wt% Pt-C(Mo_2C) 750 °C and commercially available modified carbon 20 wt% Pt-Vulcan XC72R (with different catalyst loadings from 0.1 to 1.0 mg·cm^{-2}) have been studied in 0.1 M KOH solution (Fig. 26a). The Pt-C(Mo_2C) has higher current densities $|j|$ than commercial Pt catalyst within the mixed kinetic region demonstrating higher O_2 reduction kinetics. For both catalysts, the half-wave potential value increases with the Pt loading; however, for Pt-C(Mo_2C), the change is more pronounced. According to the CV analysis (Fig. 26b), the threefold increase of the ORR electroreduction peak current density $|j_{peak}|$ has been observed for Pt-C(Mo_2C) if the catalyst loading increases tenfold. Thus, the same current densities can be achieved for Pt-C(Mo_2C) at the three times lower catalyst loading compared with the commercial catalyst, explained by the influence of C(Mo_2C) supporting effect for O_2 reduction. Therefore, the enhanced O_2 reduction activity has been explained by the meso-macroporous structure and the existence of well-conducting graphitic areas with some catalytically active defects expressed on partially graphitised C(Mo_2C) surface near the Pt clusters [331].

The time stability of Pt catalysts deposited onto different C(Mo_2C) is very good, determined by the results of 30 000 current cycles using the RDE method and accelerated stability tests [145, 146, 151, 163]. The ORR studies of Pt-C(Mo_2C) 750 °C have been performed over a wide temperature range (from 10 to 80 °C), and good thermal stability of the electrode materials has been demonstrated [144]. Also, the influence of chemical composition and amount of intermixed ionomer (polyvinyl alcohol or Nafion) in the catalyst layer on the oxygen reduction reaction characteristics have been investigated [324]. It was demonstrated that the highest electrochemical activity towards ORR was achieved by adding 30 wt% Nafion to the catalyst layer.

For a detailed analysis of the reaction mechanism, the EIS method has been used [4, 168, 169]. In good agreement with CV and RDE data, the complex plane impedance plots indicate that the adsorption/desorption step-limited processes are very slow at Pt-C(Mo_2C) catalysts as the nearly ideal limiting capacitive behaviour has been observed at very low *ac* frequencies, demonstrated in Fig. 27. Only at *ac* frequencies

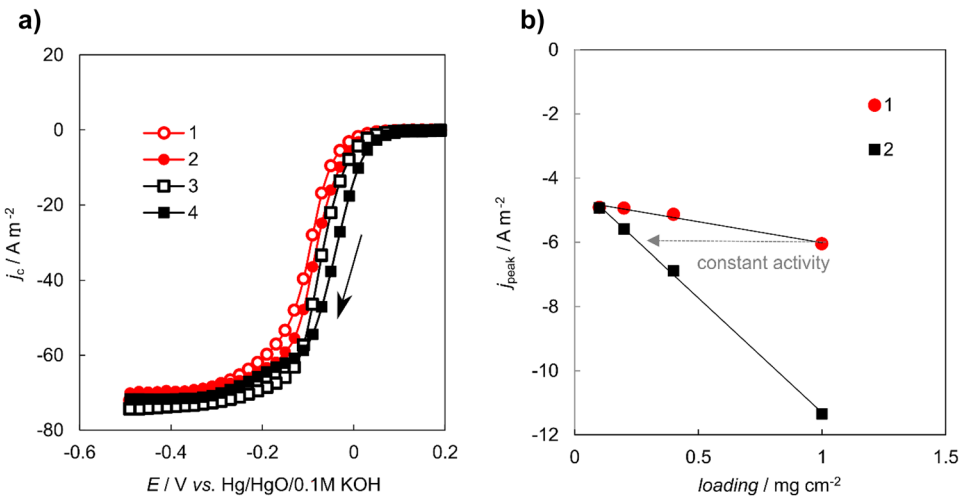

Fig. 26 **a** RDE data for 20 wt% Pt-Vulcan XC72R (1,2) and 20 wt% Pt-C(Mo_2C) 750 °C (3,4) with catalyst loading of 0.4 mg·cm^{-2} (1,3) and 1.0 mg·cm^{-2}. **b** Reduction peak current density (j_{peak}) from CV data (at electrode potential scan rate 5 mV·s.$^{-1}$) as a function of catalyst loading for 20 wt% Pt-Vulcan XC72R (1) and 20 wt% Pt-C(Mo_2C) 750 °C (2) [141]

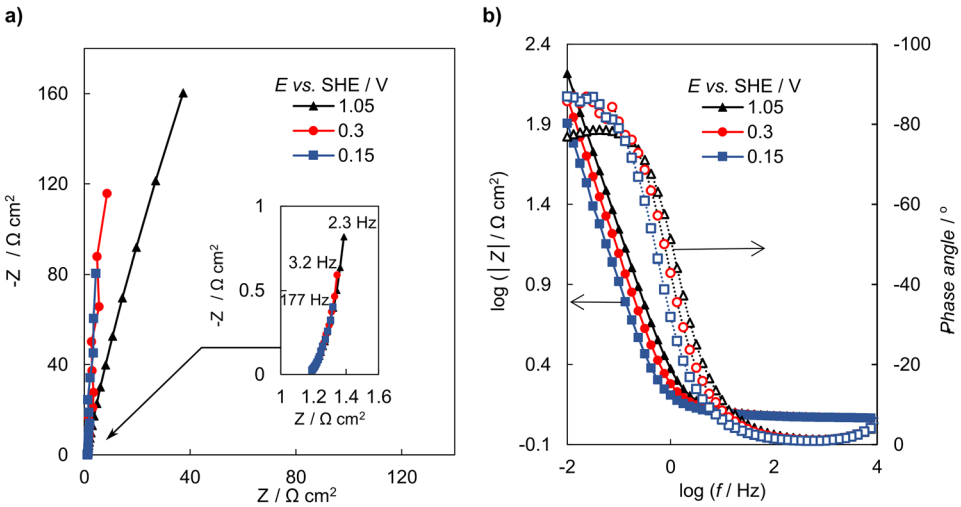

Fig. 27 For Pt-C(Mo_2C) 800 °C system [168], **a** Nyquist plots at different potentials (*E vs* SHE, noted in the figure) and **b** Bode phase angle θ, log *f*- and log |Z|, log *f*-plots in O_2 saturated 0.5 M H_2SO_4 solution at different fixed electrode potentials (noted in the figure)

higher than 100 Hz, the faradic charge transfer processes control the O_2 electroreduction. At 0.1 Hz < *f* < 100 Hz, the mixed kinetics (mass transfer and adsorption step kinetics) determines the total process rate and at *f* < 0.1 Hz, the adsorption/desorption processes are rate-limiting. This is the main reason why some hysteresis in rotating disk electrode data has been observed, as well as why the diffusion-limited currents depend on the micro/mesoporosity ratio of the catalysts applied. It should be stressed that the EIS data fitted indicate that at low *ac* frequency, totally blocking behaviour for systems has been observed. The limiting series capacitance C_s and parallel capacitance C_p values overlap at *ac f* = 1 Hz, indicating that the developed catalysts can be applied as capacitive electrodes for supercapacitors.

Oxygen reduction data on catalyst supports in acidic and alkaline electrolyte solutions

The ORR kinetics on the catalyst support and observed capacitive behaviour is also important in the PEMFC applications as catalyst structure has an enormous impact on the rate of ORR. Therefore, the ORR has been studies on various MMP carbons like CDC, C(Glc), and C(EP) [4, 137–139, 143, 149, 150, 152, 153, 155, 156, 164–170]. In order to characterise the influence of the support material structure on the ORR, the dependence of the ORR kinetic current (at a constant potential) on the specific surface area of the material was constructed (Fig. 28). There is some systematic dependence of log j_k on S_{BET}. In general, the ORR activity increases with increasing the specific surface area of the carbon support. Most importantly, the role of the carbon source (different CDCs, D-glucose, white sugar, Estonian well-decomposed peat) is clearly visible.

In acidic solution (0.1 M $HClO_4$ or 0.5 M H_2SO_4), the most active materials are based on $ZnCl_2$-activated C(EP) at 700 °C ($S_{BET} = 1270\ m^2 \cdot g^{-1}$) and C($Mo_2C$) 750 °C ($S_{BET} = 2020\ m^2 \cdot g^{-1}$) with optimal micro/mesoporosity ratio [4, 137, 154, 156, 157]. It should be noted that the ORR reduction rate may depend somewhat on the chemical nature of the electrolyte anions (SO_4^{2-} or ClO_4^-). Certainly, the least active is commercial carbon black Vulcan XC72R due to quite low specific surface area and non-defective structure. If Mo_2C is used as a carbon source, the CDCs with different specific surface areas are synthesised, and the ORR rate increases from C(Mo_2C) 600 °C to C(Mo_2C) 750 °C, and thereafter, the activity starts to decrease, being the slowest at C(Mo_2C) 1000 °C [4, 139, 164, 165, 168, 170]. Interestingly, the mesoporous CDCs with low micropore volume (C(Mo_2C) 1000 °C, fewer defects at the surface) have lower ORR kinetics compared with other CDCs [139, 141].

In a 0.1 M KOH aqueous solution, very high catalytic activity has also been established for C(Mo_2C) 750 °C and for peat-derived carbon activated by $ZnCl_2$ at 700 °C for 6 h [156, 164]. Surprisingly, C(Glc) prepared by hydrothermal carbonisation method ($S_{BET} = 1190\ m^2 \cdot g^{-1}$) is most active compared to activity in acidic solution [150]. It should be noted that only C(Mo_2C) 750 °C has a measurable amount of mesopores. But the macroscopic structures of C(Glc) and C(EP) are totally different as the nanospheres form the very highly macroscopic structure of C(Glc) and C(EP). According to the physical and electrochemical characterisation methods of the C(EP) synthesised using various carbonisation protocols, it could be concluded that depending on the carbonisation method used, carbons with very different surface morphologies, elemental compositions, porosities, and graphitisation levels and the ORR activities were obtained, influencing the ORR rate strongly [136].

Generally, for unmodified carbons, the number of electrons transferred per one oxygen molecule varies from two to three in acidic and alkaline media. This indicates that ORR is mainly a two-electron H_2O_2 forming process. However, for most active carbons, it could be above three,

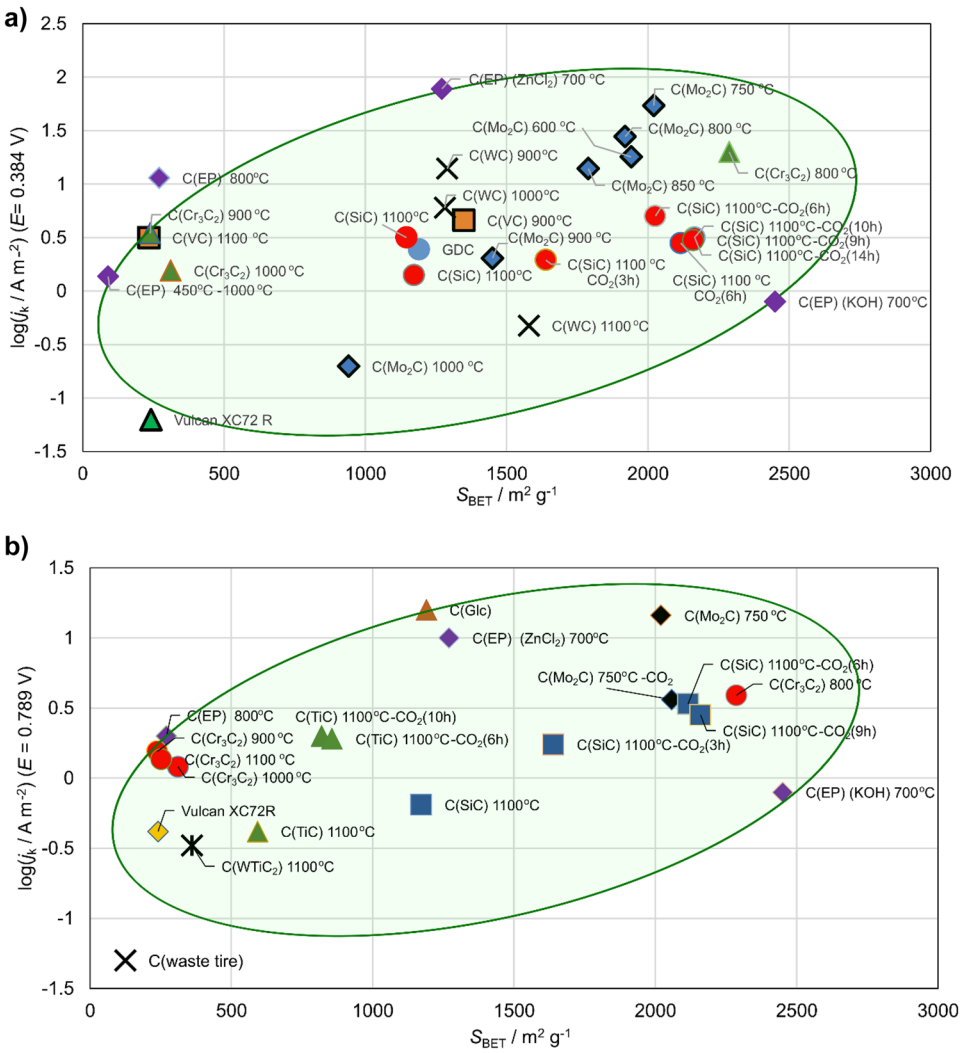

Fig. 28 Dependence of the ORR kinetic current (at a constant potential) on the specific surface area of the carbon material in **a** acidic and **b** alkaline solutions [4, 137, 149, 150, 155, 164, 166, 167, 332–335]

indicating that further reduction of peroxide is possible, i.e., the 2 + 2 reaction mechanism seems to be applicable.

The calculated Tafel plots are linear within a narrow potential range in acidic media, and the calculated Tafel-like plot slope values in acidic solutions range from 120 to 155 mV, depending on the micro/mesoporosity ratio and graphitisation level of carbon (support materials) used. In 0.1 M KOH solution, the Tafel-like plot slope values are lower (around 70–90 mV), indicating the change of reaction mechanism in alkaline media [152, 164, 166].

Oxygen reduction at d-metal-nitrogen nanoclusters activated carbon electrodes

Nowadays, it is increasingly important to find a substitute for precious metal catalysts for electrochemical oxygen electroreduction. Therefore, different d-metal compounds ($FeSO_4 \cdot 7H_2O$ or $Co(NO_3)_2 \cdot 6H_2O$) together with nitrogen-containing compounds as nitrogen donors (e.g., urea, ethylenediaminetetraacetic acid (EDTA), 1,3-di(1H-imidazol-1-yl)-2-propanol (DIPO), 1,10-phenanthroline (Phen), and 2,2′-BP) and carbon source (CDC, C(EP) and Vulcan XC72R) have been used to synthesise non-noble metal catalysts. Catalysts prepared have been characterised by novel informative methods such as HR-TEM, XPS, XRD, SEM–EDX, FIB-TOF–SIMS, XPS, and physical adsorption of gases (N_2, Ar) [151–153, 155]. RDE data in 0.1 M KOH (Fig. 29a) show that very active Fe–N catalysts have been prepared with nearly the same activity as for Pt-Vulcan. The catalytic activity decreases in the order Fe–N-2,2′-BP ≥ DIPO ≥ Phen > EDTA > urea, thus depending on the chemistry of nitrogen donors [152, 153, 155]. For the most active three Fe–N catalysts, the number of electrons transferred per one oxygen molecule is nearly 4. For some less active materials, the number of electrons transferred is lower than 4, and the H_2O_2 (or other intermediates) production cannot be discarded. The ORR kinetics in 0.1 M $HClO_4$ has also been studied, and

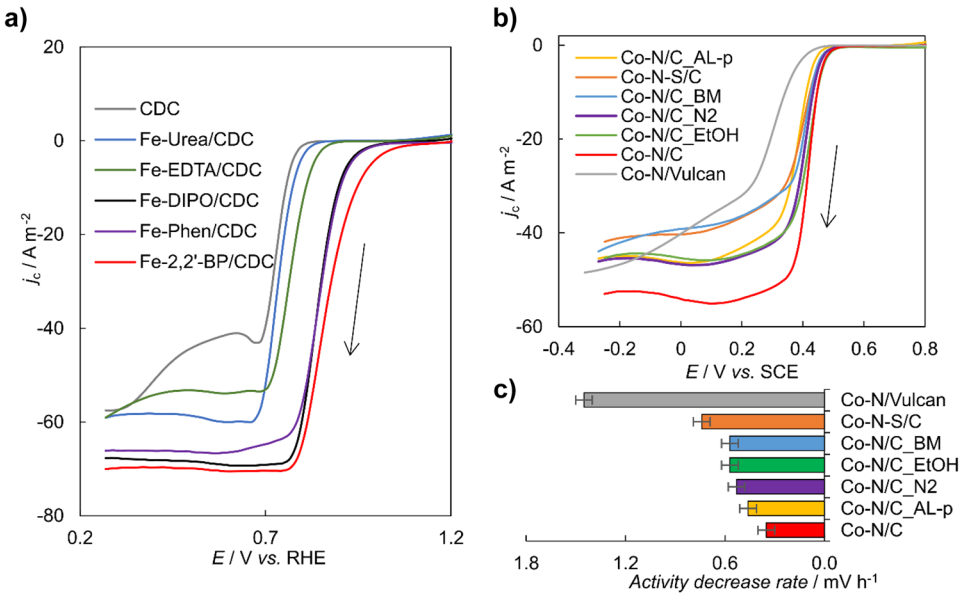

Fig. 29 RDE data for ORR **a** for Fe–N/C catalysts using various nitrogen sources (noted in the figure) in O_2 saturated 0.1 M KOH solution (3000 rev·min^{-1}, 10 mV·s^{-1}) and **b** for Co–N/C catalysts synthesised by varying synthesis conditions (noted in the figure) in O_2 saturated 0.1 M $HClO_4$ solution (1500 rev·min^{-1}, 10 mV·s.$^{-1}$). **c** Activity decrease rates for the Co–N/C catalysts (noted in the figure) [152, 154]

the activity is higher in 0.1 M KOH solution compared to the acidic solution. The same tendency has been achieved for Co–N/C type catalysts (Fig. 29b).

The results of this work indicate that tuning the synthesis conditions, such as the mixing environment, pyrolysis gas, and post-treatment, does not have a substantial effect on the ORR activity of the Fe–N/C and Co–N/C catalysts. This presents an opportunity to choose the synthesis parameters so that the catalyst manufacturing process is as cost-effective and environmentally friendly as possible. Co-doping the C(EP) with both cobalt and nitrogen shows significantly high ORR activity, and a more active ORR catalyst can be synthesised from carbon support which shows better ORR activity [137]. The more serious problem is that the time stability and the cyclability of these catalysts depend somewhat on the used nitrogen donor and synthesis method applied [154, 155]. In addition, the number of cycles that can be applied decreases with the same row of materials as the catalytic activity given above. Therefore probably, the mentioned best-developed catalysts currently can be applied only for devices where long-lasting catalytic activity is not needed (for some rescue devices and military applications because they are less expensive than the Pt-catalysts-based devices).

Methanol oxidation reaction catalysts

Various carbon supports have been used for the preparation of $Pt/CeO_2/C$ and $Pt/Pr_6O_{11}/C$ complex catalysts for the electrooxidation of methanol as a fuel [158–161]. It was found that the $Pt/Pr_6O_{11}/C$ complex catalyst demonstrated higher current densities than the $Pt/CeO_2/C$ complex catalyst (Fig. 30). The measured catalytic activity has been compared with the standard Pt-Vulcan XC72R catalysts for methanol reduction, and higher current densities have been established for self-made $Pt/CeO_2/C$ and $Pt/Pr_6O_{11}/C$ complex catalysts. The chronopotentiometry measurements demonstrated very good time stability of catalysts prepared onto CDC carbon support.

Development of solid oxide materials, fuel cells, and electrolysis cells

Development of complex oxide materials

Solid oxide fuel cells are very high energy–density power-generation devices that have been developed for more than 100 years, with the main progress achieved during the last 40–50 years [171–180]. However, there are many unsolved problems still up to the present day. The scientists at the University of Tartu have prepared solid oxide complex materials with perovskite structure since 2001 [181–185, 208, 209, 336]. The gained insight has been used for the development of fuel cell-powered self-driving car and solid oxide fuel cells for Elcogen OÜ/OY and H2Electro OÜ.

Cubic structured $La_{(1-x)}Sr_xCoO_{3-\delta}$ (LSC) and $Gd_{(1-x)}Sr_xCoO_{3-\delta}$ or hexagonally structured $Pr_{(1-x)}Sr_xCoO_{3-\delta}$ perovskites, showing mixed ionic electronic conductivity at $T > 600$ °C, were among the first synthesised materials, which were prepared from corresponding oxides (so-called solid-state reaction method) [181, 182, 336] or nitrate solutions ($La(NO_3)_3{\cdot}6H_2O$; $Pr(NO_3)_3{\cdot}xH_2O$; $Gd(NO_3)_3{\cdot}6H_2O$, $Sr(NO_3)_2$ and $Co(NO_3)_2{\cdot}6H_2O$) via the so-called nitrate solution thermal decomposition method in Pt beaker at 302–402 °C [184, 185, 209]. The fluorite structured

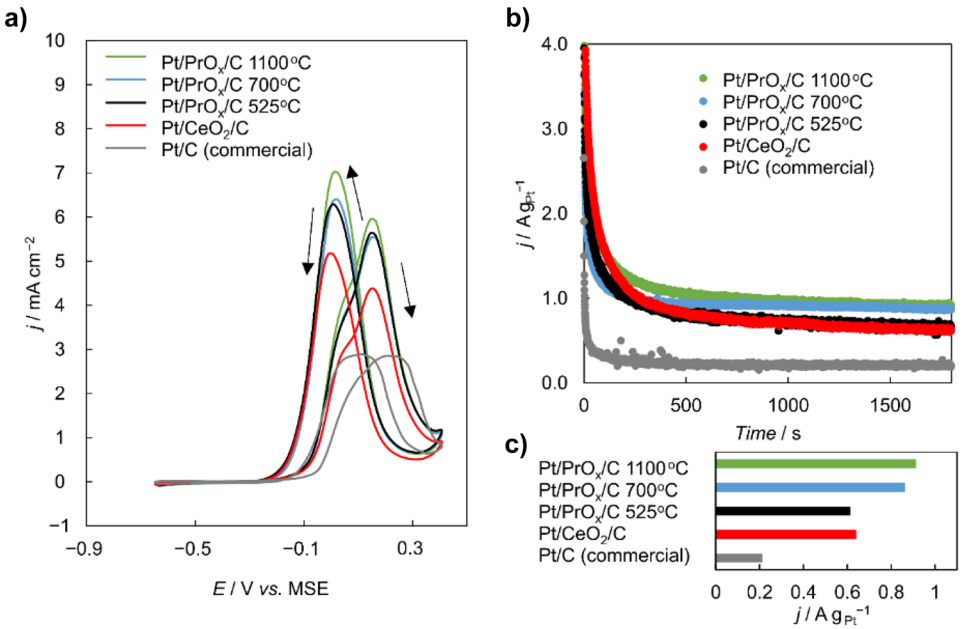

Fig. 30 Methanol oxidation on the C/Pr_6O_{11}/Pt catalysts and commercial catalyst (noted in the figure) in 0.5 M H_2SO_4 + 1 M CH_3OH solution saturated with argon. **a** Cyclic voltammograms at the potential sweep rate 10 mV·s.$^{-1}$; **b** chronoamperometry results measured at $E = -0.2$ V *vs* MSE; and **c** the final current densities after 1800s [158–161]

electrolytes $Ce_{(1-x)}Gd_xO_{2-\delta}$, $Ce_{(1-x)}Sm_xO_{2-\delta}$ ($S_{BET} = 19.9$ $m^2 \cdot g^{-1}$) were synthesised by the dry pressing of commercial oxides at different pressures and, thereafter, sintered at 1300–1427 °C. Good quality compact complex oxygen anions conducting electrolytes with 99.99% theoretical density were produced [181, 182, 184, 185, 208, 209, 336].

The anodes were prepared in two or three layers. The anode functional layer was prepared from a mixture of commercial NiO and $Ce_{0.9}Gd_{0.1}O_{2-\delta}$ with $S_{BET} = 70.8$ $m^2 \cdot g^{-1}$. A more porous anode diffusion layer was prepared from commercial NiO/$Ce_{0.9}Gd_{0.1}O_{2-\delta}$ ($S_{BET} = 6.5$ $m^2 \cdot g^{-1}$ with 1% of carbon powder removed at $T = 1200$ °C). The anode layers were screen printed and sintered at 1200–1350 °C (or sometimes at lower or higher T). The anodes have been studied using SEM–EDX, XRD, and FIB-TOF–SIMS methods. Thereafter, the cathodes were deposited onto a half-cell consisting of bi- or single layer electrolyte at different sintering temperatures [181, 182, 184, 185, 209, 336]. The supporting electrolyte half-cells, used for electrochemical studies, were prepared from oxides using the solid-state reaction method [184, 185].

The prepared materials were analysed by XRD, SEM, gas adsorption, and electrochemical characterisation methods. XRD data show that good structural ordering of cathode, anode, and electrolyte has been achieved. Furthermore, the SEM–EDX measurements show that the cathodes and anodes have a very porous and rough structure. Mixed ionic and electronic conductors (MIEC) are widely studied as SOFC cathode and anode materials. Chemical composition and the position of atoms determine the perovskite structured (ABO_3) LSC electrode characteristics. The trivalent A-site (La^{3+}, Gd^{3+}, Pr^{3+}) is doped with bivalent cation (Sr^{2+}) to generate crystallographic defects/oxygen vacancies with the aim of improving the ionic conductivity of the electrode. Heterovalent atoms (Co, Fe, Mn), also responsible for the charge balance in the lattice because of the ability to hold several different valence (redox) states, are usually incorporated in the B-site [171–185, 208, 209, 336]. It has been established that oxide ion conductivity in ABO_3 structured materials takes place by oxide ion hopping through a triangular plane made up of two A-site cations and a B-site cation. The oxygen ion mobility is, therefore, influenced by the radii of these cations. The transfer of electron density from oxygen to cations decreases the radius of oxide ions, increasing the capability of passing oxygen anions through the triangle. Oxide ion mobility tends to decrease as the oxide ion vacancies are associated with other defects, influencing both the ionic and electronic conductivities [173–185, 208, 209, 336].

The LSC electrodes have very poor tolerance against certain contaminants due to the high surface energy of the material [173–178, 213]. The rearrangement of cations leads to the segregation of Sr to the surface, being more available to various contaminants, inducing the formation of secondary phases, like $SrCO_3$ or $Sr(OH)_2$. The formation of $SrCO_3$ accelerates the Sr segregation process even further in CO_2-rich environments. The Sr segregation rate increases with the temperature. Sr-rich $SrCO_3$ and SrO are electrical insulators and, therefore, will lower the surface electrocatalytic activity for oxygen electroreduction reaction. The variation of A-site dopant and concentration, respectively, can have a contrary influence on the segregation mechanics. For example, doping LSC or $La_{1-x}Sr_xMnO_{3-\delta}$ (LSM) with Ba^{2+} in the A-site increases the Sr^{2+} segregation because of the

large mismatch between the dopant and the host cation as when the A-site of $LaMnO_3$ is doped with the smaller cation, like Ca^{2+}, with smaller size mismatch between the dopant and the host cations has been found to reduce the segregation level of dopant [172–185, 208, 209, 336].

Electrochemical and physical characteristics of complex oxide materials at moderate temperatures

The University of Tartu has focused the research of intermediate temperature SOFC cathode materials on three main areas: the optimisation of materials porosity, the use of nanoscale raw powders, and the search for novel electrochemically active materials. Regardless of many published papers, there were only a few examples of statistically correct systematic optimisation studies published before Küngas et al. [185] paper, where the performance of electrolyte–supported Ni | $Ce_{0.9}Gd_{0.1}O_{2-d}$ | $Ce_{0.9}Gd_{0-1}O_{2-d}$ | $Ln_{0.6}Sr_{0.4}Co_{3-\delta}$ (Ln = La, Gd, or Pr) symmetric single cells were optimised for anode diffusion layer porosity, anode functional layer starting powder specific surface area ($S_{BET,\ powder}$), and cobaltite-based cathode material chemical composition in a single designed experiment according to the so-called response surface methodology method (RSM) [185]. The optimal cell was found to have either $La_{0.6}Sr_{0.4}CoO_{3-\delta}$ or $Pr_{0.6}Sr_{0.4}CoO_{3-\delta}$ (PSC) cathode, whereas the Ln metal cations (La^{3+} or Pr^{3+}) had a minor effect on the total polarisation resistance values confirmed by the analysed experimental results. For the best cell, an anode active layer prepared of a starting powder with the smallest particle sizes, i.e., with maximal specific surface area $S_{BET} = 135\ m^2 \cdot g^{-1}$ and a maximal pore former content of 2% in raw anode material, used for the preparation of single cells. Obtained data are in good agreement with Zhao and Virkar's results [210]. In addition, it should be stressed that the final electrode preparation conditions, i.e., the temperature and duration of the sintering, the exact weight and thickness of the screen-printed layer, the density of the screen-printed layer, exact reduction conditions of the anode and amount of binder, and acting as an additional pore former in a raw unsintered anode layer, all had a very big influence on the anode porosity and final activity.

The increasing porosity of cathodes was achieved with various carbon powders, which were added as pore formers into the raw powders of SOFC cathodes [181, 182, 184–186, 209, 336, 338]. It was established that very porous $La_{0.6}Sr_{0.4}CoO_{3-\delta}$ can be prepared at optimal carbon powder additions and carbon particle diameters [208]. Very highly porous materials were synthesised, as demonstrated in Figs. 31 and 32.

Cathode porosity had a considerable influence on the oxygen reduction rate, with optimal porosity of 63–66% established for $La_{0.6}\ Sr_{0.4}CoO_{3-\delta}$ and was achieved with 0.5 wt% pore-former addition into the raw cathode paste. It should be stressed that the cathode porosity depends on the sintering temperature and duration, cathode raw layer thickness and particles size distribution of pore former, binder addition

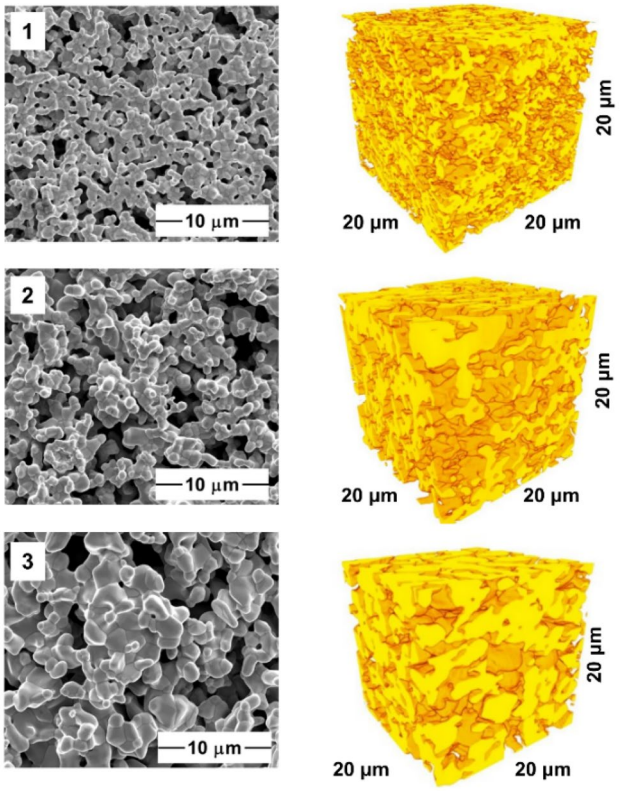

Fig. 31 SEM images and corresponding FIB-SEM 3D reconstructions of the SOFC cathode structures [337]

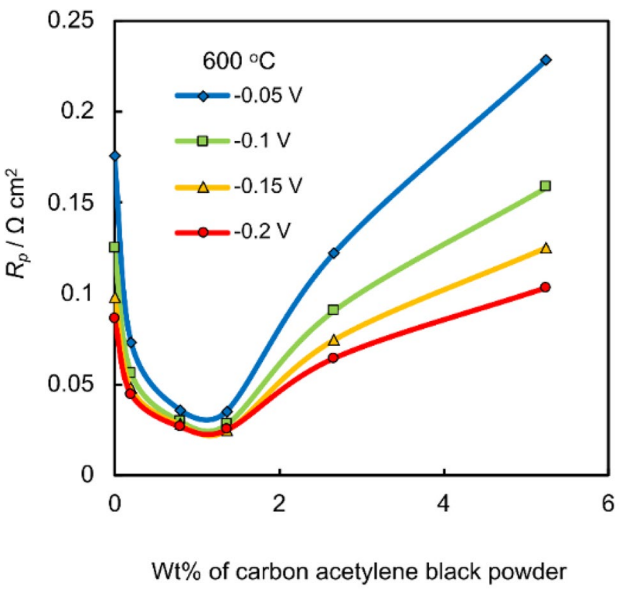

Fig. 32 Influence of cathode porosity on SOFC performance. Different amounts of carbon acetylene black powder were used as pore-forming agents [339]

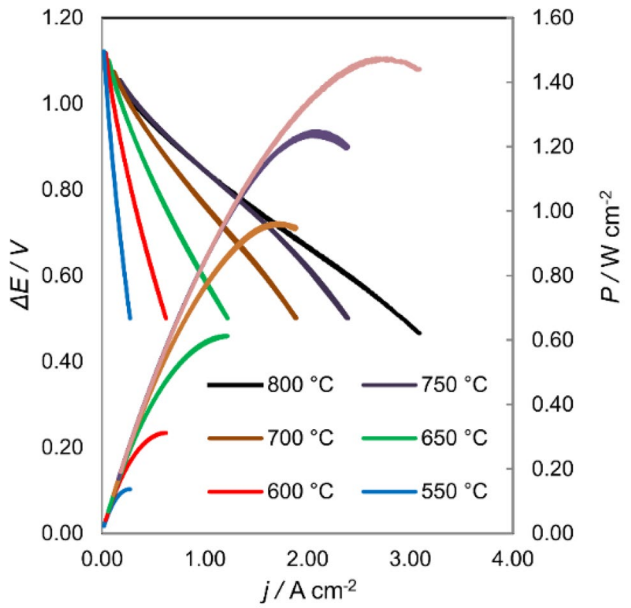

Fig. 33 Power density *vs* current density plots for PSCO|GDC|YSZ|Ni-/YSZ single cell at working temperatures (noted in the figure) [339]

wt% in raw cathode layer, and particle size distribution of raw oxide powder [181, 182, 184, 185, 209, 336].

The FIB-SEM–based 3D tomography has been used to create a 3D model of porous cathode microstructure [21], and it was found that the optimal total porosity is 54%. It was demonstrated that the surface area of the electrode is a very important parameter in addition to the microporosity of the materials under study.

Very high current and power densities have been established for $Pr_{0.6}Sr_{0.4}CoO_{3-\delta}$ | $Ce_{O.9}Gd_{0.1}O_{2-\delta}$ | $Zr_{0.86}Y_{0.15}O_{2-\delta}$ | $Ni/Zr_{0.92}Y_{0.08}O_{2-\delta}$ (Fig. 33) [339]. The bilayered electrolyte was deposited to avoid the formation of isolating bilayer of $SrZrO_{2-\delta}$ or other Sr-containing compounds at the cathode surface. The chrono-potentiometry measurements data show that after the quick decrease of current density at the beginning of polarisation, the currents stabilised at high values for very long times.

The supporting anode microstructure can be a dominating factor in determining the overpotential of the electrooxidation reaction of the fuel at the so-called three-phase boundaries (TPB) and long-term stability of the anode in the fuel cell operating conditions. The anode must have sufficient porosity to allow gas transport to the reaction sites and product species away from the reaction centres. At the time, most of the papers approached the optimisation of Ni-GDC anodes (gadolinium-doped ceria based electrolytes) similarly to Ni-YSZ anodes (yttria-stabilised zirconia based electrolytes) [340, 341]. Tamm et al. [202, 204] optimised the microstructure of supporting Ni-GDC anodes for intermediate SOFC by changing the amount of pore former in the anode raw material. In addition, the influence of pore former particle size distribution on the anode microstructure was studied. The gas adsorption and FIB-SEM were used for the meso-macroporosity analysis of the prepared anodes and cathodes. Assembled single cells were analysed using CV, EIS, and chronopotentiometry or chronoamperometry methods. For the identification of the characteristic frequencies and corresponding process parameters of cathode and anodic processes, the single-cell impedance spectra were recorded and compared analytically as a function of applied potential, partial pressure of hydrogen in the fuel compartment, and partial pressure of oxygen in the cathode compartment. The measured EIS data were analysed in detail using the non-linear regression analysis fitting method and differential derivate of impedance modulus *vs* frequency dependence methods [177, 185, 187].

MIEC ceramic electrodes like $Sr_2Fe_{1.5}Mo_{0.5}O_{6-\delta}$ (SFM) with double perovskite-type structure ($A_2BB'O_6$) or $La_{1-x}Sr_xCr_{0.5}Mn_{0.5}O_{3-\delta}$ (LSCM) or $La_{1-x}Sr_xTiO_{3-\delta}$ (LST) with perovskite structure (ABO_3) can be used instead of metal-cermet hydrogen electrodes [197–201]. SFM has been demonstrated to be a relatively good conductor. The conductivity of LSCM increases at high oxygen partial pressures (high water concentrations) at operating temperatures, which makes it very attractive for electrolysis systems. The main disadvantage of these materials is relatively low electrocatalytic activity. To improve the catalytic activity and stability of the ceramic electrode materials, it is possible to manipulate the bulk stoichiometries and dopant concentrations. Possible dopants for the A-site of SFM are La and Ca and Ni or Cu in the B-site, as well as Ni to the B-site of LSCM. Doping of crystal structure influences the stability of MIEC material, and because of that, better stability could be obtained in some cases by impregnation (creating catalytic centres onto the MIEC surface by using treatment with a solution of catalytically active metal ions) of porous stoichiometrically balanced (no deficiency between A and B sites) non-doped material [197–201, 213].

Infiltration method for SOFC electrode synthesis and its electrochemical characteristics

Tamm et al. employed the aqueous salt solution infiltration method [203] for the preparation of Ni-free low-temperature solid oxide fuel cell anodes, including ceramic 20 vol% $La_{0.7}Sr_{0.3}VO_{3-\delta}$ (LSV) composite electrode, infiltrated into 38 μm thick $Ce_{0.85}Sm_{0.15}O_{2-\delta}$ electrolyte scaffold with 0.019 $S{\cdot}cm^{-1}$ ionic conductivity at 600 °C [186, 187, 202–205, 210]. The cells, without CeO_2 and Pd promoters, exhibited very low catalytic activity towards H_2 oxidation, with a total high polarisation resistance of 2.0 $\Omega{\cdot}cm^2$ and a maximal power density of 17 $mW{\cdot}cm^{-2}$ at 600 °C, comparable to the results established for $(La_{0.7}Sr_{0.3})VO_{3-\delta}$ + YSZ published by

Park et al. [342]. The cell, activated with 2.1 vol% CeO_2 catalyst, was only slightly more active with a total polarisation resistance of 1.4 Ω·cm^2 and maximum power density of 25 mW·cm^{-2} at 600 °C. Activation of LSV with 0.3 vol% of Pd increased the performance of LSV to 59 mW·cm^{-2}. The maximum power density of the cell infiltrated with 2.1 vol% CeO_2 and 0.3 vol% Pd (i.e., complex activated) increased up to 139 mW·cm^{-2} at low $T = 600$ °C. The CeO_2 and Pd activated cells with mentioned anode composition and porous $La_{0.8}Sr_{0.2}CoO_{3-\delta}$ cathodes demonstrated low total electrode polarisation resistances 0.3 Ω·cm^2 and 0.6 Ω·cm^2 in humified H_2 and CH_4, respectively. Improved anode performance was also achieved by modifying the surface of the porous scaffold through etching with an aqueous HF solution, decreasing the total cell resistance down to 0.1 Ω·cm^2 and 0.4 Ω·cm^2 at 600 °C in humidified H_2 and CH_4, respectively. A power density of up to 238 mW·cm^{-2} was achieved for the H_2-fuel-feeded cell. The anodes based on LSV-SDC (samaria-doped ceria) composites exhibited stable performance for at least 40 h under load. However, the industrial use of infiltration technology is still hindered by the multistep nature of the method, making it very time and space consuming [202–205].

Further enhancement of cells was achieved by the optimisation of the scaffold porosity and thickness. After etching the SDC with 10% HF aqueous solution at $T = 22$ °C, the specific surface area increased from 0.32 to 0.53 m^2·g^{-1}. Compared to the YSZ scaffold, where the surface area increased from 0.48 to 2.1 m^2·g^{-1}, the complete restructuring of the electrode took place as the entire pore network changed to a sheet and pillar-like structure. The surface roughness increased for the SDC scaffold, explained by the different solubility of Ce^{4+} and Zr^{4+} in H_2O [186, 187, 202–205, 210].

Development of novel operando methods for analyses of processes at different interfaces

The FIB-TOF–SIMS method, introduced by Kilner et al. [178], has been used for analyses of Sr segregation processes at cathode | electrolyte interfaces [192, 195, 343]. It was found that the segregation of Sr takes place already during the sintering of $LnSrCoO_{3-\delta}$ cathodes onto the barrier $Ce_{1-x}Gd_xO_{2-\delta}$ layer deposited onto YSZ dense electrolyte to avoid contact of electrolyte with the electrode (Fig. 34). It is mainly caused by the problem that the deposited chemical barrier layer is not dense and defect-free.

Therefore, the pulsed laser deposition (PLD) has been applied, and due to the nearly defect-free barrier layer, the Sr segregation effect has been minimised [192, 195, 343]. The main problem is that the PLD is a very time-consuming method and also not usable for large electrodes. Magnetron sputtering (MS) deposited barrier layer has been tested as well. More expressed Sr mobility through the barrier layer has been observed compared with the PLD layer. For some systems, ultrasonic spray (hot) pyrolysis (deposition onto a hot cathode or hot anode) has been successfully used to develop a chemical barrier layer. However, the mobility of Sr through these layers was slightly higher compared to PLD layers because of the very small grain size and a significant amount of grain boundary interfaces.

The *operando* XRD diffraction method under reactant feeding conditions and electrode polarisation has been used by Kivi et al. [188, 189]. Kinetics of crystallographic changes caused oxide ion flux through the membrane to the porous electrode was studied. This is valuable information for the interpretation of impedance data and for separation for interfacial reorganisation processes and crystallographic changes if electrode polarisation is varied. Differences in crystallographic response for polarisation changes were analysed in the case of $(La_{1-x}Sr_x)_yCoO_{3-\delta}$ and $La_{0.6}Sr_{0.4}Co_{0.2}Fe_{0.8}O_{3-\delta}$.

Nurk et al. developed the methods for the analyses of processes at SOFC anodes [193] and the influence of contaminants [194] on SOFC Ni-cermet anode surface composition, i.e., the oxidation state of Ni and $Ce_{0.9}Gd_{0.1}O_{2-\delta}$ electrolyte characteristics (Ce oxidation state).

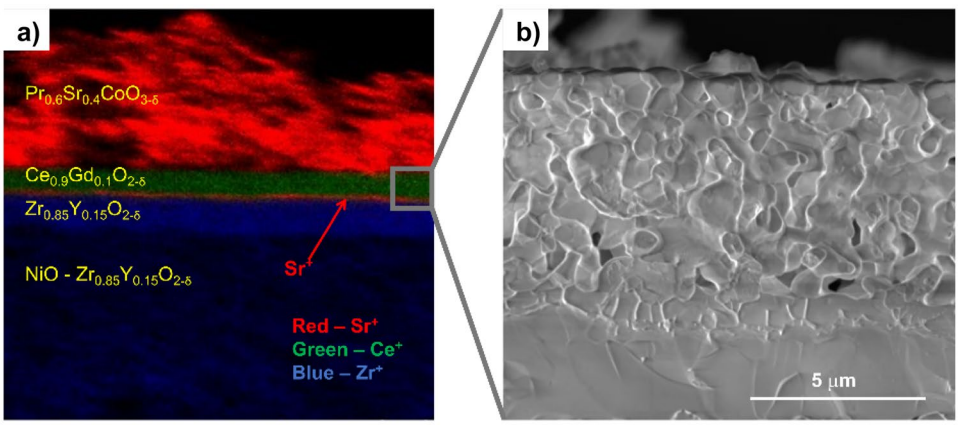

Fig. 34 **a** FIB-TOF–SIMS and **b** SEM images for YSZ | GDC electrolyte system with PSC cathode showing unwanted Sr mobility and forming of $SrZrO_3$ phase between GDC chemical barrier layer and electrolyte layers [343]

Kooser et al. [195] improved the ambient pressure XPS method discussed by Nenning et al. [196] and applied it in the *operando* high-temperature near-ambient pressure conditions (HT-NAP-XPS) in conjunction with EIS. A pulsed laser-deposited Ni-$Ce_{0.9}Gd_{0.1}O_{2-\delta}$ anode thin film was studied in a novel three-electrode dual-chamber cell at different H_2 pressures and electrode potentials at around 650 °C. The simultaneous use of HT-NAP-XPS and EIS methods made it possible to describe possible redox reactions on the surface of Ni-$Ce_{0.1}Gd_{0.1}O_{2-\delta}$ (Ni^{2+} to Ni(O) and Ce^{4+} to Ce^{3+}). Depth probing of the anode showed remarkable variations in the valence band of XPS spectra with H_2 concentration change at the electrode. The formation of a metal-like structure at the valence edge indicates an electrical conductivity gradient directly beneath the anode surface at lower hydrogen pressure values (around 1 mbar). At higher H_2 pressure (5 mbar), the metal-like valence edge was dominant at all probed anode materials. Changes in the electronic structure of the Ce 3d and Ni 2p photoelectron spectra caused by the electrode potential and hydrogen pressure variations were observed, and corresponding fitting of curves was conducted. The O 1 s and valence band photoelectron data were used for the calculation of the chemical composition and redox changes in/at the Ni-$Ce_{0.9}Gd_{0.1}O_{2-\delta}$ electrode. Curve fitting of the Ce 3d photoelectron spectra gave a quantitative estimation of the Ce^{3+} to Ce^{4+} ratio at the anode surface (Ce^{3+}/Ce^{4+} dependence on H_2 pressure and electrode potential/polarisation). At open circuit voltage (OCV) (− 1.263 V) and low H_2 pressure (p_{H2} = 1.17 mbar), the concentration of Ce^{3+} at the electrode surface was 53.7%, but at 5 mbar of H_2 (OCV = − 1.263 V), the concentration of Ce^{3+} was 67.2%. At electrode potential E = − 0.9 V, at 5 mbar H_2 pressure, the concentration of Ce^{3+} was 60.2%. Thus, the influence of the electrode potential on the chemical (redox) state of anode components was demonstrated. The HT-NAP-XPS data were compared with the EIS data, depending strongly on the electrode potential and hydrogen pressure applied and indicating that the resistance of mass-transfer processes correlates positively with Ce^{4+} reduction to Ce^{3+} [193, 195, 196].

Influence of A-site deficiency and chemical composition of B-site including the concentration of Ni, Co, and Cr on electrochemical characteristics of hydrogen electrode in $(La_{(1-x)}Sr_x)_yCr_{0.5-z}Mn_{0.5-w}Ni_{z+w}O_{3-\delta}$ | $(Sc_2O_3)_{0.1}(CeO_2)_{0.01}ZrO_2)_{0.89}$ | $La_{0.8}Sr_{0.2}FeO_{3-\delta}$ reversible solid oxide fuel cell has been studied by Maide et al. [197], Lillmaa et al. [206]. The infiltration method has been used for the preparation of cathode and anode electrodes. The dense $(Sc_2O_3)_{0.1}(CeO_2)_{0.01}(ZrO_2)_{0.89}$ electrolyte layer was sandwiched and co-sintered between two porous ScCeSZ layers. Thereafter, the anode and cathode were impregnated into the porous ScCeSZ matrixes. The wafers were fabricated by laminating three green tapes (porous–tense–porous) using isostatic compression, followed by the high-temperature sintering at 1400 °C for 5 h. Electrochemical characterisation using EIS and CV has been conducted in fuel cell and electrolysis modes. It was established that in the fuel cell mode, the most notable limiting steps were detected around 0.5 Hz and were attributed to a gas-porous solid adsorption–desorption slow rate process. Oxygen partial pressure variations led to small variations in the total impedance of single cells. In electrolysis mode, the dissociative adsorption process was established as an important limiting stage, and the kinetic limitations of the charge transfer step were remarkable. The increase of A-site deficiency caused a significant increase in high-frequency resistance values as well as some increase in total polarisation resistance. Variations in B-site composition had a significant influence on the electrochemical performance with very different frequency dependence of impedance. At 850 °C, the highest current density values of 0.27 A·cm^{-2} (fuel cell mode, p_{H2} = 0.97 atm and p_{H2O} = 0.03 atm) and 0.66 A·cm^{-2} (electrolysis mode) at unit cell potentials of 0.9 and 1.5 V, respectively, were measured for $La_{0.75}Sr_{0.25}Cr_{0.3}Mn_{0.5}Ni_{0.2}O_{3-d}$ (fuel cell mode) and for $(La_{0.8}Sr_{0.2})_xCr_{0.49}Mn_{0.49}Ni_{0.02}O_{3-\delta}$ (electrolysis mode) in hydrogen fuel gas with p_{H2} = 0.70 atm and p_{H2O} = 0.3 atm, respectively. It should be noted that the electrode compositions and porosities should be different for optimal current densities established for FC mode and EL mode. This was explained by the different rate-limiting processes observed for fuel cell mode and electrolysis mode.

Co-electrolysis of CO_2 and H_2O has been investigated by Maide et al. [197], Lillmaa et al. [206] using the A-site deficient $La_{1-x}Sr_xCr_{1-x}MnO_{3-\delta}$ electrodes grown via the impregnation method. The thickness of the dense electrolyte and the porous scaffold was approximately 75 µm and 40 µm, respectively. Ceramic perovskite-structured $(La_{0.8}Sr_{0.2})_x(Cr_{0.5}Mn_{0.5})_yNi_zO_{3-\delta}$ (x = 1, 0.9, 0.8; y = 1.0, 0.94; z = 0.0, 0.06) with various A-site deficiencies and 6 mol% of Ni in B-site were used as hydrogen electrodes and $La_{0.8}Sr_{0.2}FeO_{3-\delta}$ as O_2 electrode. Moderate reaction activity and stability have been observed.

Conclusions

This review summarises the major achievements in interfacial electrochemistry in Estonia since 1990. Electrical double layer characteristics, adsorption of organic compounds and specific adsorption of anions at sp-metal single-crystal planes and micro-mesoporous carbons from aprotic and other non-aqueous electrolytes, and ionic liquids and ionic liquid mixtures have been studied and discussed. Electrochemical characteristics of supercapacitors, including hybrid capacitors and Li^+-ion and Na^+-ion batteries, have been established and analysed. The influence of carbon support materials characteristics (micro-, meso-, and macroporosity,

pore size distribution and hierarchical porous structure, graphitisation level, and electric conductivity) on the Pt-metal nanoclusters, and Pt-metals free polymer membrane fuel cells parameters have been analysed. The influence of rare earth metal oxide nanoclusters deposited onto Pt nanoparticles activated carbon particles on direct methanol fuel cell characteristics has been demonstrated. The electrochemical properties of high-temperature solid oxide fuel cells and high-temperature electrolysis cells have been established, and the influence of the electrode (negatively and positively charged, compositions, porous structure, etc.) on the electrochemical characteristics has been discussed.

Different in situ and *operando* methods like *operando* electrochemical high-temperature X-ray diffraction spectroscopy for solid oxide electrode analyses, synchrotron beam near ambient pressure dual chamber XPS for anode and cathode processes in solid oxide fuel cells, in situ XPS for the study of the influence of electrode potential on the electrochemical processes at carbon electrodes in ionic liquids, neutron beam small angle scattering studies at porous carbon, and complex metal hydride materials characteristics have been conducted and results have been analysed.

The strong influence of sp-metals (Bi, Sb, Cd) and single-crystal carbon (C(0001)) electronic characteristics (concentration of charge carriers, effective mass of electrons) on the potential of zero charge, differential capacitance, Gibbs adsorption, and Gibbs free energies of adsorption values have been demonstrated. The effect of solvent chemical composition and dielectric characteristics on the surface activity and Gibbs adsorption energy values of anions at sp-metal single-crystal and carbon electrodes has been demonstrated. The influence of ionic liquid anion composition on the specific adsorption characteristic, including time constant, at Bi(*hkl*), Sb(*hkl*), Cd(*hklf*), and C(0001) single-crystal electrodes have been demonstrated. The applicability limits of various ionic liquids in electrical double layer capacitors, hybrid supercapacitors, secondary-ion batteries, and other electrochemical devices determining the energy and power density parameters have been verified. Appreciable increase of specific energy and power densities for supercapacitors, hybrid capacitors, and Na^+-ion batteries with ionic liquid and ionic liquid mixture electrolytes containing surface-active iodide and bromide anions has been demonstrated.

The solid fundamental basis and continuous emphasis on the development of a comprehensive understanding of electrochemical processes at the electrode | electrolyte interface in collaboration with the drive to design and enhance the performance of novel energy storage devices has led to the publication of numerous scientific papers with exciting discoveries, e.g., 4–10 V capacitors with graphene-based electrodes, the visualisation of adsorbed layers at single-crystal electrodes, and synthesis of carbide-derived carbon materials with outstanding properties. Furthermore, the group has set their focus on supporting the Estonian transition to green energy through supporting science-based policy-making and industrial processes.

Funding This work was supported by the Estonian Research Council grants PSG249, PRG676, PRG551 and by the EU through the European Regional Development Fund under project TK141 (2014–2020.4.01.15–0011).

References

1. Trasatti S, Lust E (1999) The potential of zero charge. In: White RE, Bockris JO, Conway BE (eds) Modern aspects of electrochemistry. Kluwer Academic / Plenum Publishers, New York, pp 1–193
2. Lust E (2002) Electrical double layers. Double layers at single-crystal and polycrystalline electrodes. In: A. J. Bard, M. Stratmann, E. Gileadi, M. Urbakh (eds) Encyclopedia of electrochemistry: thermodynamics and electrified interfaces. Wiley VCH, pp 188–225
3. Härmas R, Palm R, Härmas M et al (2018) Influence of porosity parameters and electrolyte chemical composition on the power densities of non-aqueous and ionic liquid based supercapacitors. Electrochim Acta 283:931–948. https://doi.org/10.1016/j.electacta.2018.06.115
4. Lust E, Vaarmets K, Nerut J et al (2014) Influence of specific surface area and microporosity-mesoporosity of pristine and Pt-nanoclusters modified carbide derived carbon electrodes on the oxygen electroreduction. Electrochim Acta 140:294–303. https://doi.org/10.1016/j.electacta.2014.04.054
5. Oll O, Väärtnõu M, Gorbatovski G et al (2019) Adsorption of anions on bismuth and cadmium single crystal plane electrodes from various solvents and ionic liquid mixtures. Electrochim Acta 319:895–908. https://doi.org/10.1016/j.electacta.2019.06.179
6. Shpigel N, Levi MD, Sigalov S et al (2016) In situ hydrodynamic spectroscopy for structure characterization of porous energy storage electrodes. Nat Mater 15:570–575. https://doi.org/10.1038/nmat4577
7. Eikerling M, Kornyshev AA, Lust E (2005) Optimized structure of nanoporous carbon-based double-layer capacitors. J Electrochem Soc 152:E24–E33. https://doi.org/10.1149/1.1825379
8. Shpigel N, Sigalov S, Levi MD et al (2018) In situ acoustic diagnostics of particle-binder interactions in battery electrodes. Joule 2:988–1003. https://doi.org/10.1016/j.joule.2018.02.014
9. Lust E, Jänes A, Miidla P, Lust K (1997) Adsorption of pyridine on the (111), (001) and (001) faces of bismuth. J Electroanal

Chem 425:25–37. https://doi.org/10.1016/S0022-0728(96)04962-5
10. Lust K, Väärtnõu M, Lust E (2000) Adsorption of halide anions on bismuth single crystal plane electrodes. Electrochim Acta 45:3543–3554. https://doi.org/10.1016/S0013-4686(00)00432-1
11. Lust E, Jänes A, Lust K, Erlich J (1996) The structure of the electrical double layer at the faces of bismuth, antimony, or cadmium single crystals in surface-inactive electrolytes. Russ J Electrochem 32:552–564
12. Lust E, Jänes A, Lust K et al (1997) Influence of surface pretreatment of bismuth and cadmium electrodes to the electric double layer and adsorption characteristics of organic compounds. Electrochim Acta 42:2861–2879. https://doi.org/10.1016/S0013-4686(97)00107-2
13. Lust E, Jänes A, Lust K, Ehrlich J (1999) Orientation of organic compounds at single-crystal bismuth electrodes. Electrochim Acta 44:4707–4720. https://doi.org/10.1016/S0013-4686(99)00221-2
14. Lust K, Perkson E, Lust E (2000) Kinetics of hydrogen evolution on single crystal bismuth electrodes. Russ J Electrochem 36:1257–1262. https://doi.org/10.1007/BF02757702
15. Conway BE (1999) Electrochemical supercapacitors: scientific fundamentals and technological applications. Springer, New York
16. Kötz R, Carlen M (2000) Principles and applications of electrochemical capacitors. Electrochim Acta 45:2483–2498. https://doi.org/10.1016/S0013-4686(00)00354-6
17. Nikitin A, Gogotsi Y (2004) Nanostructured carbide-derived carbon. Encycl Nanosci Nanotechnol 7:553–574. https://doi.org/10.1166/000000004323036865
18. Gogotsi Y (2006) Nanomaterials handbook. CRC Press, Boca Raton
19. Beguin F, Frackowiak E (2013) Supercapacitors: materials, systems and applications. John Wiley & Sons
20. Frumkin A (1979) Potentsialy Nulevogo Zaryada. Nauka, Moscow
21. Frumkin A (1987) Izbrannye trudy: elektrodnye protsessy. Nauka, Moscow
22. Grahame DC (1947) The electrical double layer and the theory of electrocapillarity. Chem Rev 41:441–501. https://doi.org/10.1021/cr60130a002
23. Damaskin BB, Petrii OA, Batrakov VV (1971) Adsorption of organic compounds on electrodes. Plenum Press, New York
24. Weaver MJ, Anson FC (1975) Simple criteria for distinguishing between inner- and outer-sphere electrode reaction mechanisms. J Am Chem Soc 97:3
25. Hamelin A, Stoicoviciu L, Silva F (1987) The temperature dependence of the double-layer properties of gold faces in perchloric acid solutions: part II. The (110) gold face. J Electroanal Chem Interfacial Electrochem 236:283–294. https://doi.org/10.1016/0022-0728(87)88033-6
26. Tsirlina GA, Petrii OA, Kharkats YuI, Kuznetsov AM (1999) Allowing for charge distributions in reagents (products) when analyzing electrostatic effects in electrochemical kinetics. Russ J Electrochem 35:1210–1217
27. Tsirlina GA, Titova NV, Nazmutdinov RR, Petrii OA (2001) Electroreduction of [Fe(CN)6]3– on a mercury electrode: substantiating activationless character of the process at high overvoltages. Russ J Electrochem 37:15–25. https://doi.org/10.1023/A:1009067309773
28. Fawcett WR, Hromadova M, Tsirlina GA, Nazmutdinov RR (2001) The role of charge distribution in the reactant and product in double layer effects for simple heterogeneous redox reactions. J Electroanal Chem 498:93–104. https://doi.org/10.1016/S0022-0728(00)00279-5
29. Taberna PL, Simon P, Fauvarque JF (2003) Electrochemical characteristics and impedance spectroscopy studies of carbon-carbon supercapacitors. J Electrochem Soc 150:A292–A300. https://doi.org/10.1149/1.1543948
30. Damaskin BB, Stenina EV, Baturina OA, Sviridova LN (1998) Selecting a model of the diffuse layer when describing electroduction of anions in the framework of the slow-discharge theory. Sov Electrochem 34
31. Barsoukov E, Macdonald JR (2005) Impedance spectroscopy: theory, experiment, and applications. Wiley, John & Sons, Incorporated, Hoboken, New Jersey
32. Levich V (1962) Physicochemical hydrodynamics. Prentice-Hall, University of California
33. Conway BE, Bockris JO (1979) Modern aspects of electrochemistry. Springer, US
34. Vetter KJ (1967) Electrochemical kinetics: theoretical and experimental aspects, 1st edn. Academic Press
35. Palm U, Past V, Pullerits R (1967) Иизучение специфической адсорбции ионов на каплевидном висмутовом электроде. Elektrokhimiya 3:376–380
36. Frumkin A, Pärnoja M, Grigorev N, Palm U (1974) Structure of the electric double layer and the zero-change potential on the(111) face of a bi single crystal. Elektrokhimiya 10:1130–1133
37. Pärnoja M, Palm U, Grigoriev N (1975) Adsorption of I-ions on (111) face of bismuth single crystals. Sov Electrochem 11:530–534
38. Vorotyntsev MA, Kornyshev AA (1984) Models to describe collective properties of the metal / solvent interface in electric double-layer theory. Elektrokhimiya 20:3–47
39. Leiva E, Schmickler W (1987) The double layer capacity of jellium with pseudopotentials. J Electroanal Chem Interfacial Electrochem 229:39–50
40. Lipkowski J, Ross PN (1993) Frontiers of electrochemistry, structure of electrified interfaces. Wiley
41. Amokrane S, Badiali JP (1989) A new analysis of the differential capacitance of an ideally polarized electrode. J Electroanal Chem Interfacial Electrochem 266:21–35. https://doi.org/10.1016/0022-0728(89)80212-8
42. Amokrane S, Badiali JP (1991) A new analysis of the differential capacitance of an ideally polarized electrode: part II. Nonaqueous solvents. J Electroanal Chem Interfacial Electrochem 297:377–398. https://doi.org/10.1016/0022-0728(91)80035-O
43. Amokrane S, Badiali JP (1992) Analysis of the capacitance of the metal—solution interface: role of the metal and the metal—solvent coupling. In: Bockris JO, Conway BE, White RE (eds) Modern aspects of electrochemistry. Springer, US, Boston, MA, pp 1–95
44. Ivaništšev V, Nazmutdinov RR, Lust E (2013) A comparative DFT study of the adsorption of H2O molecules at Bi, Hg, and Ga surfaces. Surf Sci 609:91–99. https://doi.org/10.1016/j.susc.2012.11.009
45. Ruzanov A, Karu K, Ivaništšev V et al (2016) Interplay between the hydrophilicity of metal electrodes and their interfacial capacitance. Electrochim Acta 210:615–621. https://doi.org/10.1016/j.electacta.2016.05.110
46. Ruzanov A, Lembinen M, Ers H et al (2018) Density functional theory study of ionic liquid adsorption on circumcoronene shaped graphene. J Phys Chem C 122:2624–2631. https://doi.org/10.1021/acs.jpcc.7b12156
47. Ruzanov A, Lembinen M, Jakovits P et al (2018) On the thickness of the double layer in ionic liquids. Phys Chem Chem Phys 20:10275–10285. https://doi.org/10.1039/C7CP07939G
48. Voroshylova IV, Lembinen M, Ers H et al (2019) On the role of the surface charge plane position at Au(hkl)–BMImPF6

interfaces. Electrochim Acta 318:76–82. https://doi.org/10.1016/j.electacta.2019.05.058
49. Ers H, Lembinen M, Mišin M et al (2020) Graphene–ionic liquid interfacial potential drop from density functional theory-based molecular dynamics simulations. J Phys Chem C 124:19548–19555. https://doi.org/10.1021/acs.jpcc.0c02964
50. Voroshylova IV, Ers H, Docampo-Álvarez B et al (2020) Hysteresis in the MD simulations of differential capacitance at the ionic liquid–Au interface. J Phys Chem Lett 11:10408–10413. https://doi.org/10.1021/acs.jpclett.0c03212
51. Voroshylova IV, Ers H, Koverga V et al (2021) Ionic liquid–metal interface: the origins of capacitance peaks. Electrochim Acta 379:138148. https://doi.org/10.1016/j.electacta.2021.138148
52. Ers H, Voroshylova IV, Pikma P, Ivaništšev VB (2022) Double layer in ionic liquids: temperature effect and bilayer model. J Mol Liq. https://doi.org/10.1016/j.molliq.2022.119747
53. Lust E, Jänes A, Sammelselg V et al (1998) Surface roughness of bismuth, antimony and cadmium electrodes. Electrochim Acta 44:373–383. https://doi.org/10.1016/S0013-4686(98)00084-X
54. Lust E, Jänes A, Sammelselg V, Miidla P (2000) Influence of charge density and electrolyte concentration on the electrical double layer characteristics at rough cadmium electrodes. Electrochim Acta 46:185–191. https://doi.org/10.1016/S0013-4686(00)00572-7
55. Daikhin LI, Kornyshev AA, Urbakh M (1996) Double-layer capacitance on a rough metal surface. Phys Rev E 53:6192–6199. https://doi.org/10.1103/PhysRevE.53.6192
56. Daikhin LI, Kornyshev AA, Urbakh M (1997) Double layer capacitance on a rough metal surface: surface roughness measured by "Debye ruler." Electrochim Acta 42:2853–2860. https://doi.org/10.1016/S0013-4686(97)00106-0
57. Daikhin LI, Kornyshev AA, Urbakh M (1998) Nonlinear Poisson-Boltzmann theory of a double layer at a rough metal/electrolyte interface: a new look at the capacitance data on solid electrodes. J Chem Phys 108:1715–1723. https://doi.org/10.1063/1.475543
58. Lust E, Lust K, Jänes A (1995) Influence of the crystallographic structure of the electrode surface on the structure of the electrical double layer and adsorption of organic molecules. Russ J Electrochem 31:807–821
59. Lust E, Jänes A, Lust K, Väärtnõu M (1997) Electric double layer structure and adsorption of cyclohexanol on single crystal cadmium, antimony and bismuth electrodes. Electrochim Acta 42:771–783. https://doi.org/10.1016/S0013-4686(96)00339-8
60. Romann T, Oll O, Pikma P et al (2014) Surface chemistry of carbon electrodes in 1-ethyl-3-methylimidazolium tetrafluoroborate ionic liquid — an in situ infrared study. Electrochim Acta 125:183–190. https://doi.org/10.1016/j.electacta.2014.01.077
61. Oll O, Romann T, Pikma P, Lust E (2016) Spectroscopy study of ionic liquid restructuring at lead interface. J Electroanal Chem 778:41–48. https://doi.org/10.1016/j.jelechem.2016.08.016
62. Oll O, Romann T, Siimenson C, Lust E (2017) Influence of chemical composition of electrode material on the differential capacitance characteristics of the ionic liquid|electrode interface. Electrochem Commun 82:39–42. https://doi.org/10.1016/j.elecom.2017.07.015
63. Siinor L, Poom J, Siimenson C et al (2014) Electrochemical characteristics pyrolytic graphite | mixture of 1-ethyl-3-methylimidazolium tetrafluoroborate and 1-ethyl-3-methylimidazolium iodide interface. J Electroanal Chem 719:133–137. https://doi.org/10.1016/j.jelechem.2014.01.035
64. Siinor L, Lust K, Lust E (2010) Influence of anion composition and size on the double layer capacitance for Bi(111) | room temperature ionic liquid interface. Electrochem Commun 12:1058–1061. https://doi.org/10.1016/j.elecom.2010.05.025
65. Siimenson C, Lembinen M, Oll O et al (2016) Electrochemical investigation of 1-ethyl-3-methylimidazolium bromide and tetrafluoroborate mixture at Bi (111) electrode interface. J Electrochem Soc 163:H723–H730. https://doi.org/10.1149/2.0111609jes
66. Damaskin BB, Baturina OA, Safonov VA, Lust E, Jänes A (2000) Adsorption parameters of n-hexanol on single-crystal faces of bismuth: a regression analysis of the differential capacitance data and comparing the capacitance and chronocoulometry measurements. Russ J Electrochem 36:673–678
67. Lust E, Jänes A, Pärn T, Nigu P (2003) Influence of nanoporous carbon electrode thickness on the electrochemical characteristics of a nanoporous carbon|tetraethylammonium tetrafluoroborate in acetonitrile solution interface. J Solid State Electrochem 8:224–237. https://doi.org/10.1007/s10008-003-0396-6
68. Lust E, Jänes A, Arulepp M (2004) Influence of solvent nature on the electrochemical parameters of electrical double layer capacitors. J Electroanal Chem 562:33–42. https://doi.org/10.1016/j.jelechem.2003.07.034
69. Arulepp M, Permann L, Leis J et al (2004) Influence of the solvent properties on the characteristics of a double layer capacitor. J Power Sources 133:320–328. https://doi.org/10.1016/j.jpowsour.2004.03.026
70. Jänes A, Thomberg T, Lust E (2007) Synthesis and characterisation of nanoporous carbide-derived carbon by chlorination of vanadium carbide. Carbon 45:2717–2722. https://doi.org/10.1016/j.carbon.2007.09.041
71. Jänes A, Permann L, Arulepp M, Lust E (2004) Electrochemical characteristics of nanoporous carbide-derived carbon materials in non-aqueous electrolyte solutions. Electrochem Commun 6:313–318. https://doi.org/10.1016/j.elecom.2004.01.009
72. Arulepp M, Leis J, Lätt M et al (2006) The advanced carbide-derived carbon based supercapacitor. J Power Sources 162:1460–1466. https://doi.org/10.1016/j.jpowsour.2006.08.014
73. Leis J, Arulepp M, Kuura A et al (2006) Electrical double-layer characteristics of novel carbide-derived carbon materials. Carbon 44:2122–2129. https://doi.org/10.1016/j.carbon.2006.04.022
74. Jänes A, Lust E (2005) Organic carbonate-organic ester-based non-aqueous electrolytes for electrical double layer capacitors. Electrochem Commun 7:510–514. https://doi.org/10.1016/j.elecom.2005.03.004
75. Jänes A, Lust E (2006) Electrochemical characteristics of nanoporous carbide-derived carbon materials in various nonaqueous electrolyte solutions. J Electrochem Soc 153:A113–A116. https://doi.org/10.1149/1.2135212
76. Jänes A, Kurig H, Lust E (2007) Characterisation of activated nanoporous carbon for supercapacitor electrode materials. Carbon 45:1226–1233. https://doi.org/10.1016/j.carbon.2007.01.024
77. Thomberg T, Jänes A, Lust E (2009) Energy and power performance of vanadium carbide derived carbon electrode materials for supercapacitors. J Electroanal Chem 630:55–62. https://doi.org/10.1016/j.jelechem.2009.02.015
78. Jänes A, Thomberg T, Kurig H, Lust E (2009) Nanoscale fine-tuning of porosity of carbide-derived carbon prepared from molybdenum carbide. Carbon 47:23–29. https://doi.org/10.1016/j.carbon.2008.07.010
79. Tallo I, Thomberg T, Kontturi K et al (2011) Nanostructured carbide-derived carbon synthesized by chlorination of tungsten carbide. Carbon 49:4427–4433. https://doi.org/10.1016/j.carbon.2011.06.033
80. Thomberg T, Kurig H, Jänes A, Lust E (2011) Mesoporous carbide-derived carbons prepared from different chromium carbides. Microporous Mesoporous Mater 141:88–93. https://doi.org/10.1016/j.micromeso.2010.11.006

81. Tee E, Tallo I, Kurig H et al (2015) Huge enhancement of energy storage capacity and power density of supercapacitors based on the carbon dioxide activated microporous SiC-CDC. Electrochim Acta 161:364–370. https://doi.org/10.1016/j.electacta.2015.02.106
82. Tallo I, Thomberg T, Kurig H et al (2014) Novel micromesoporous carbon materials synthesized from tantalum hafnium carbide and tungsten titanium carbide. Carbon 67:607–616. https://doi.org/10.1016/j.carbon.2013.10.034
83. Tee E, Tallo I, Thomberg T et al (2016) Supercapacitors based on activated silicon carbide-derived carbon materials and ionic liquid. J Electrochem Soc 163:A1317–A1325. https://doi.org/10.1149/2.0931607jes
84. Tee E, Tallo I, Thomberg T et al (2018) Steam and carbon dioxide co-activated silicon carbide-derived carbons for high power density electrical double layer capacitors. J Electrochem Soc 165:A2357. https://doi.org/10.1149/2.1261810jes
85. Tee E, Tallo I, Lust E et al (2019) Electrical double layer capacitors based on steam and CO2-steam co-activated carbon electrodes and ionic liquid electrolyte. J Electrochem Soc 166:A1558
86. Lust E, Nurk G, Jänes A et al (2002) Electrochemical properties of nanoporous carbon electrodes. Condens Matter Phys 5:307–327
87. Lust E, Nurk G, Jänes A et al (2003) Electrochemical properties of nanoporous carbon electrodes in various nonaqueous electrolytes. J Solid State Electrochem 7:91–105. https://doi.org/10.1007/s10008-002-0316-1
88. Lust E, Liivand K, Vaas I et al (2017) Separators, electrodes, half-cells, and cells of electrical energy storage devices. Patent No US 9951443. 31.12.2015
89. Eskusson J, Jänes A, Kikas A et al (2011) Physical and electrochemical characteristics of supercapacitors based on carbide derived carbon electrodes in aqueous electrolytes. J Power Sources 196:4109–4116. https://doi.org/10.1016/j.jpowsour.2010.10.100
90. Pohl M, Kurig H, Tallo I et al (2017) Novel sol-gel synthesis route of carbide-derived carbon composites for very high power density supercapacitors. Chem Eng J 320:576–587. https://doi.org/10.1016/j.cej.2017.03.081
91. Paalo M, Tallo I, Thomberg T et al (2019) Enhanced power performance of highly mesoporous sol-gel TiC derived carbons in ionic liquid and non-aqueous electrolyte based capacitors. J Electrochem Soc 166:A2887. https://doi.org/10.1149/2.0721913jes
92. Laheäär A, Jänes A, Lust E (2011) Electrochemical properties of carbide-derived carbon electrodes in non-aqueous electrolytes based on different Li-salts. Electrochim Acta 56:9048–9055. https://doi.org/10.1016/j.electacta.2011.05.126
93. Laheäär A, Kurig H, Jänes A, Lust E (2009) LiPF6 based ethylene carbonate–dimethyl carbonate electrolyte for high power density electrical double layer capacitor. Electrochim Acta 54:4587–4594. https://doi.org/10.1016/j.electacta.2009.03.059
94. Laheäär A, Jänes A, Lust E (2012) NaClO4 and NaPF6 as potential non-aqueous electrolyte salts for electrical double layer capacitor application. Electrochim Acta 82:309–313. https://doi.org/10.1016/j.electacta.2012.04.149
95. Väli R, Jänes A, Thomberg T, Lust E (2016) D-glucose derived nanospheric hard carbon electrodes for room-temperature sodium-ion batteries. J Electrochem Soc 163:A1619–A1626. https://doi.org/10.1149/2.0771608jes
96. Väli R, Laheäär A, Jänes A, Lust E (2014) Characteristics of non-aqueous quaternary solvent mixture and Na-salts based supercapacitor electrolytes in a wide temperature range. Electrochim Acta 121:294–300. https://doi.org/10.1016/j.electacta.2013.12.149
97. Väli R, Jänes A, Thomberg T, Lust E (2017) Synthesis and characterization of d-glucose derived nanospheric hard carbon negative electrodes for lithium- and sodium-ion batteries. Electrochim Acta 253:536–544. https://doi.org/10.1016/j.electacta.2017.09.094
98. Jänes A, Eskusson J, Mattisen L, Lust E (2015) Electrochemical behaviour of hybrid devices based on Na2SO4 and Rb2SO4 neutral aqueous electrolytes and carbon electrodes within wide cell potential region. J Solid State Electrochem 19:769–783. https://doi.org/10.1007/s10008-014-2668-8
99. Tõnurist K, Thomberg T, Jänes A et al (2012) Specific performance of electrical double layer capacitors based on different separator materials in room temperature ionic liquid. Electrochem Commun 22:77–80. https://doi.org/10.1016/j.elecom.2012.05.029
100. Anderson E, Grozovski V, Siinor L et al (2014) In situ STM studies of Bi(111)|1-ethyl-3-methylimidazolium tetrafluoroborate + 1-ethyl-3-methylimidazolium iodide interface. Electrochem Commun 46:18–21. https://doi.org/10.1016/j.elecom.2014.05.032
101. Oll O, Siimenson C, Lust K et al (2017) Specific adsorption from an ionic liquid: impedance study of iodide ion adsorption from a pure halide ionic liquid at bismuth single crystal planes. Electrochim Acta 247:910–919. https://doi.org/10.1016/j.electacta.2017.07.034
102. Armand M, Endres F, MacFarlane DR et al (2009) Ionic-liquid materials for the electrochemical challenges of the future. Nat Mater 8:621–629. https://doi.org/10.1038/nmat2448
103. Fedorov MV, Kornyshev AA (2014) Ionic liquids at electrified interfaces. Chem Rev 114:2978–3036. https://doi.org/10.1021/cr400374x
104. Pajkossy T, Jurczakowski R (2017) Electrochemical impedance spectroscopy in interfacial studies. Curr Opin Electrochem 1:53–58. https://doi.org/10.1016/j.coelec.2017.01.006
105. Jänes A, Eskusson J, Thomberg T et al (2016) Ionic liquid-1,2-dimethoxyethane mixture as electrolyte for high power density supercapacitors. J Energy Chem 25:609–614. https://doi.org/10.1016/j.jechem.2016.02.011
106. Romann T, Oll O, Pikma P et al (2015) 4–10 V capacitors with graphene-based electrodes and ionic liquid electrolyte. J Power Sources 280:606–611. https://doi.org/10.1016/j.jpowsour.2015.01.153
107. Romann T, Anderson E, Pikma P et al (2017) Reactions at graphene | tetracyanoborate ionic liquid interface — new safety mechanisms for supercapacitors and batteries. Electrochem Commun 74:38–41. https://doi.org/10.1016/j.elecom.2016.11.016
108. Kruusma J, Tõnisoo A, Pärna R et al (2016) Influence of the negative potential of molybdenum carbide derived carbon electrode on the in situ synchrotron radiation activated X-ray photoelectron spectra of 1-ethyl-3-methylimidazolium tetrafluoroborate. Electrochim Acta 206:419–426. https://doi.org/10.1016/j.electacta.2015.10.060
109. Kruusma J, Tõnisoo A, Pärna R et al (2017) The electrochemical behavior of 1-ethyl-3-methyl imidazolium tetracyanoborate visualized by in situ X-ray photoelectron spectroscopy at the negatively and positively polarized micro-mesoporous carbon electrode. J Electrochem Soc 164:A3393–A3402. https://doi.org/10.1149/2.1861713jes
110. Kruusma J, Tõnisoo A, Pärna R et al (2017) Influence of iodide ions concentration on the stability of 1-ethyl-3-methylimidazolium tetrafluoroboratel molybdenum carbide derived carbon electrode interface. J Electrochem Soc 164:A1110–A1119. https://doi.org/10.1149/2.0641706jes
111. Zhang Y, Zheng JB (2007) Investigation on the electro-oxidation of iodide in the room temperature ionic liquid, 1-butyl-3-methylimidazolium tetrafluoroborate at platinum electrode. Electrochim Acta 52:4082–4086. https://doi.org/10.1016/j.electacta.2006.11.025

112. Tooming T, Thomberg T, Siinor L et al (2014) A type high capacitance supercapacitor based on mixed room temperature ionic liquids containing specifically adsorbed iodide anions. J Electrochem Soc 161:A222–A227. https://doi.org/10.1149/2.014403jes
113. Thomberg T, Lust E, Jänes A (2020) Iodide ion containing ionic liquid mixture based asymmetrical capacitor performance. J Energy Storage 32:101845. https://doi.org/10.1016/j.est.2020.101845
114. Zhao J, Gorbatovski G, Oll O et al (2022) Influence of water on the electrochemical characteristics and nanostructure of Bi(hkl) | ionic liquid interface. Electrochim Acta. https://doi.org/10.1016/j.electacta.2022.140263
115. Rogers EI, Silvester DS, Aldous L et al (2008) Electrooxidation of the iodides [C4mim]I, LiI, NaI, KI, RbI, and CsI in the room temperature ionic liquid [C4mim][NTf2]. J Phys Chem C 112:6551–6557. https://doi.org/10.1021/jp800145k
116. Romann T, Lust E, Oll O (2016) Method of forming a dielectric through electrodeposition on an electrode for a capacitor. Patent No. PCT/EP2015/072399
117. Tõnurist K, Jänes A, Thomberg T et al (2009) Influence of mesoporous separator properties on the parameters of electrical double-layer capacitor single cells. J Electrochem Soc 156:A334–A342
118. Tõnurist K, Thomberg T, Jänes A et al (2013) Influence of separator properties on electrochemical performance of electrical double-layer capacitors. J Electroanal Chem 689:8–20. https://doi.org/10.1016/j.jelechem.2012.11.024
119. Formhals A (1940) Artificial thread and method of producing same. US2187306A
120. Ramakrishna S, Fujihara K, Teo W-E et al (2005) An introduction to electrospinning and nanofibers. World Scientific
121. Andrady AL (2008) Science and technology of polymer nanofibers. John Wiley & Sons
122. Tõnurist K, Thomberg T, Jänes A, Lust E (2013) Specific performance of supercapacitors at lower temperatures based on different separator materials. J Electrochem Soc 160:A449–A457. https://doi.org/10.1149/2.044303jes
123. Tõnurist K, Vaas I, Thomberg T et al (2014) Application of multistep electrospinning method for preparation of electrical double-layer capacitor half-cells. Electrochim Acta 119:72–77. https://doi.org/10.1016/j.electacta.2013.11.155
124. Torop J, Sugino T, Asaka K et al (2012) Nanoporous carbide-derived carbon based actuators modified with gold foil: prospect for fast response and low voltage applications. Sens Actuators B Chem 161:629–634. https://doi.org/10.1016/j.snb.2011.10.079
125. Palmre V, Torop J, Arulepp M et al (2012) Impact of carbon nanotube additives on carbide-derived carbon-based electroactive polymer actuators. Carbon 50:4351–4358. https://doi.org/10.1016/j.carbon.2012.04.071
126. Palmre V, Lust E, Jänes A et al (2011) Electroactive polymer actuators with carbon aerogel electrodes. J Mater Chem 21:2577–2583. https://doi.org/10.1039/C0JM01729A
127. Kaasik F, Tamm T, Hantel MM et al (2013) Anisometric charge dependent swelling of porous carbon in an ionic liquid. Electrochem Commun 34:196–199. https://doi.org/10.1016/j.elecom.2013.06.011
128. Kurig H, Russina M, Tallo I et al (2016) The suitability of infinite slit-shaped pore model to describe the pores in highly porous carbon materials. Carbon 100:617–624. https://doi.org/10.1016/j.carbon.2016.01.061
129. Härmas R, Palm R, Kurig H et al (2021) Carbide-derived carbons: WAXS and Raman spectra for detailed structural analysis. C 7:29. https://doi.org/10.3390/c7010029
130. Palm R, Härmas R, Härk E et al (2021) Study of the structural curvature in Mo2C derived carbons with contrast matched small-angle neutron scattering. Carbon 171:695–703. https://doi.org/10.1016/j.carbon.2020.09.070
131. Mathiesen JK, Väli R, Härmas M et al (2019) Following the in-plane disorder of sodiated hard carbon through operando total scattering. J Mater Chem A 7:11709–11717. https://doi.org/10.1039/C9TA02413A
132. Härk E, Petzold A, Goerigk G et al (2019) Carbide derived carbons investigated by small angle X-ray scattering: inner surface and porosity vs. graphitization. Carbon 146:284–292. https://doi.org/10.1016/j.carbon.2019.01.076
133. Härmas R, Palm R, Russina M et al (2019) Transport properties of H2 confined in carbide-derived carbons with different pore shapes and sizes. Carbon 155:122–128. https://doi.org/10.1016/j.carbon.2019.08.041
134. Koppel M, Palm R, Härmas R et al (2021) In situ observation of pressure modulated reversible structural changes in the graphitic domains of carbide-derived carbons. Carbon 174:190–200. https://doi.org/10.1016/j.carbon.2020.12.025
135. Palm R, Tallo I, Romann T, Kurig H (2015) Methane adsorption on specially designed TiC and Mo2C derived carbons with different pore size and surface morphology. Microporous Mesoporous Mater 218:167–173. https://doi.org/10.1016/j.micromeso.2015.07.016
136. Gogotsi Y, Portet C, Osswald S et al (2009) Importance of pore size in high-pressure hydrogen storage by porous carbons. Int J Hydrog Energy 34:6314–6319. https://doi.org/10.1016/j.ijhydene.2009.05.073
137. Jäger R, Teppor P, Paalo M et al (2021) Synthesis and characterization of cobalt and nitrogen co-doped peat-derived carbon catalysts for oxygen reduction in acidic media. Catalysts 11:715. https://doi.org/10.3390/catal11060715
138. Härk E, Sepp S, Valk P et al (2013) Impact of the various catalysts (Pt, Pt-Ru) deposited onto carbon support to the slow oxygen reduction reaction kinetics. ECS Trans 45:1–11. https://doi.org/10.1149/04521.0001ecst
139. Sepp S, Härk E, Valk P et al (2014) Impact of the Pt catalyst on the oxygen electroreduction reaction kinetics on various carbon supports. J Solid State Electrochem 18:1223–1229. https://doi.org/10.1007/s10008-013-2180-6
140. Grozovski V, Kasuk H, Nerut J et al (2015) Oxygen reduction at shape-controlled platinum nanoparticles and composite catalysts based on (100)Pt nanocubes on microporous–mesoporous carbon supports. ChemElectroChem 2:847–851. https://doi.org/10.1002/celc.201500021
141. Härk E, Jäger R, Lust E (2014) Effect of platinum nanoparticle loading on oxygen reduction at a Pt nanocluster-activated microporous–mesoporous carbon support. Electrocatalysis 6:242–254. https://doi.org/10.1007/s12678-014-0238-6
142. Sepp S, Vaarmets K, Nerut J et al (2016) Performance of polymer electrolyte membrane fuel cell single cells prepared using hierarchical microporous-mesoporous carbon supported Pt nanoparticles activated catalysts. Electrochim Acta 203:221–229. https://doi.org/10.1016/j.electacta.2016.03.158
143. Jäger R, Härk E, Romann T et al (2016) C(Mo2C) and Pt–C(Mo2C) based mixed catalysts for oxygen reduction reaction. J Electroanal Chem 761:89–97. https://doi.org/10.1016/j.jelechem.2015.12.018
144. Jäger R, Härk E, Steinberg V, Lust E (2016) Influence of temperature on the oxygen electroreduction activity at micro-mesoporous carbon support. J Electrochem Soc 163:F284–F290. https://doi.org/10.1149/2.0861603jes
145. Vaarmets K, Sepp S, Nerut J, Lust E (2016) Accelerated durability tests for Pt-nanoclusters modified carbide derived carbons catalysts in acidic solution. ECS Trans 75:899–911. https://doi.org/10.1149/07514.0899ecst
146. Vaarmets K, Nerut J, Sepp S et al (2017) Accelerated durability tests of molybdenum carbide derived carbon based Pt catalysts

for PEMFC. J Electrochem Soc 164:F338–F346. https://doi.org/10.1149/2.1021704jes
147. Vaarmets K, Valk P, Nerut J et al (2017) Rotating disk electrode study of carbon supported Pt-nanoparticles synthesized using microwave-assisted method. ECS Trans 80:743–755. https://doi.org/10.1149/08008.0743ecst
148. Härk E, Jäger R, Kasatkin PE et al (2018) The electrochemical activity of two binary alloy catalysts toward oxygen reduction reaction in 0.1 M KOH. J Solid State Electrochem 22:31–40. https://doi.org/10.1007/s10008-017-3720-2
149. Taleb M, Nerut J, Tooming T et al (2015) Oxygen electroreduction on platinum nanoparticles deposited onto D-glucose derived carbon. J Electrochem Soc 162:F651–F660. https://doi.org/10.1149/2.0231507jes
150. Taleb M, Nerut J, Tooming T et al (2016) Oxygen electroreduction on platinum nanoparticles activated electrodes deposited onto D-glucose derived carbon support in 0.1 M KOH. J Electrochem Soc 163:F1251–F1257. https://doi.org/10.1149/2.1051610jes
151. Sepp S, Nerut J, Vaarmets K et al (2018) Activity and stability of carbide derived carbon supports in PEMFC application. ECS Trans 86:507–517. https://doi.org/10.1149/08613.0507ecst
152. Jäger R, Kasatkin PE, Härk E et al (2018) The effect of N precursors in Fe-N/C type catalysts based on activated silicon carbide derived carbon for oxygen reduction activity at various pH values. J Electroanal Chem 823:593–600. https://doi.org/10.1016/j.jelechem.2018.06.040
153. Jäger R, Kasatkin PE, Teppor P et al (2018) Novel Fe-N/C type catalysts based on carbide derived carbon for oxygen reduction reaction. ECS Trans 85:1229
154. Teppor P, Jäger R, Härk E et al (2020) Exploring different synthesis parameters for the preparation of metal-nitrogen-carbon type oxygen reduction catalysts. J Electrochem Soc 167:054513
155. Teppor P, Jäger R, Härk E et al (2018) ORR activity and stability of Co-N/C catalysts based on silicon carbide derived carbon and the impact of loading in acidic media. J Electrochem Soc 165:F1217
156. Teppor P, Jäger R, Paalo M et al (2020) Peat-derived carbon-based non-platinum group metal type catalyst for oxygen reduction and evolution reactions. Electrochem Commun 113:106700. https://doi.org/10.1016/j.elecom.2020.106700
157. Teppor P, Jäger R, Paalo M et al (2022) Peat as a carbon source for non-platinum group metal oxygen electrocatalysts and AEMFC cathodes. Int J Hydrog Energy 47:16908–16920. https://doi.org/10.1016/j.ijhydene.2022.03.199
158. Valk P, Nerut J, Tallo I et al (2016) Structure and stability of partially chlorinated molybdenum carbide composite materials synthesised via high temperature chlorination. Electrochim Acta 191:337–345. https://doi.org/10.1016/j.electacta.2016.01.048
159. Valk P, Nerut J, Kanarbik R, Lust E (2016) Facile synthesis of high performance platinum-cerium oxide nanocatalysts for methanol oxidation. ECS Trans 75:1005–1012. https://doi.org/10.1149/07514.1005ecst
160. Valk P, Nerut J, Kanarbik R et al (2018) Synthesis and characterization of platinum-cerium oxide nanocatalysts for methanol oxidation. J Electrochem Soc 165:F315–F323. https://doi.org/10.1149/2.0781805jes
161. Valk P, Nerut J, Kanarbik R et al (2019) Synthesis and characterization of platinum-praseodymium oxide nanocatalysts for methanol electrooxidation. J Electrochem Soc 166:F1062. https://doi.org/10.1149/2.0691914jes
162. Sepp S, Nerut J, Vaarmets K et al (2016) Enhanced stability of novel hierarchical carbon supports in PEMFC application. ECS Trans 75:789–799. https://doi.org/10.1149/07514.0789ecst
163. Sepp S, Vaarmets K, Nerut J et al (2017) Enhanced stability of symmetrical polymer electrolyte membrane fuel cell single cells based on novel hierarchical microporous-mesoporous carbon supports. J Solid State Electrochem 21:1035–1043. https://doi.org/10.1007/s10008-016-3448-4
164. Jäger R, Kasatkin PE, Härk E, Lust E (2013) Oxygen reduction on molybdenum carbide derived micromesoporous carbon electrode in alkaline solution. Electrochem Commun 35:97–99. https://doi.org/10.1016/j.elecom.2013.08.001
165. Vaarmets K, Sepp S, Nerut J et al (2013) Electrochemical and physical characterization of Pt–Ru alloy catalyst deposited onto microporous–mesoporous carbon support derived from Mo2C at 600 °C. J Solid State Electrochem 17:1729–1741. https://doi.org/10.1007/s10008-013-2030-6
166. Jäger R, Härk E, Kasatkin PE, Lust E (2014) Investigation of a carbon-supported Pt electrode for oxygen reduction reaction in 0.1M KOH aqueous solution. J Electrochem Soc 161:F861–F867. https://doi.org/10.1149/2.0491409jes
167. Härk E, Steinberg V, Sepp S et al (2013) Electrochemical and physical characterization of Pt activated micromesoporous vanadium carbide derived carbon electrodes in sulfuric acid solution. J Electrochem Soc 160:F923–F930. https://doi.org/10.1149/2.010309jes
168. Vaarmets K, Nerut J, Härk E, Lust E (2013) Electrochemical and physical characterisation of Pt-nanocluster activated molybdenum carbide derived carbon electrodes. Electrochim Acta 104:216–227. https://doi.org/10.1016/j.electacta.2013.04.097
169. Lust E, Härk E, Nerut J, Vaarmets K (2013) Pt and Pt–Ru catalysts for polymer electrolyte fuel cells deposited onto carbide-derived carbon supports. Electrochim Acta 101:130–141. https://doi.org/10.1016/j.electacta.2012.10.024
170. Sepp S, Nerut J, Vaarmets K et al (2014) The impact of Pt-nanocluster deposition and Nafion® content on the oxygen electroreduction kinetics on molybdenum carbide derived carbon synthesized at 1000 °C. ECS Trans 61:37–50. https://doi.org/10.1149/06126.0037ecst
171. Rand DAJ, Dicks AL (2018) Fuel cell systems explained. John Wiley and Sons Ltd, Hoboken, pp 236–261. https://doi.org/10.1002/9781118706992
172. Brett DJL, Atkinson A, Brandon NP, Skinner SJ (2008) Intermediate temperature solid oxide fuel cells. Chem Soc Rev 37:1568–1578. https://doi.org/10.1039/B612060C
173. Minh NQ, Takahashi T (1995) Science and technology of ceramic fuel cells. Elsevier
174. Singhal SC, Kendall K (2003) High-temperature solid oxide fuel cells: fundamentals, design and applications. Elsevier
175. Bidrawn F, Kim G, Aramrueang N et al (2010) Dopants to enhance SOFC cathodes based on Sr-doped LaFeO3 and LaMnO3. J Power Sources 195:720–728. https://doi.org/10.1016/j.jpowsour.2009.08.034
176. Irvine JT, Connor P (2013) Solid oxide fuels cells: facts and figures. Springer
177. Mogensen MB (2020) Materials for reversible solid oxide cells. Curr Opin Electrochem 21:265–273. https://doi.org/10.1016/j.coelec.2020.03.014
178. Kilner JA, Skinner SJ, Brongersma HH (2011) The isotope exchange depth profiling (IEDP) technique using SIMS and LEIS. J Solid State Electrochem 15:861–876. https://doi.org/10.1007/s10008-010-1289-0
179. Lei C, Simpson MF, Virkar AV (2021) Investigation of electrode kinetics of porous La-Sr-Co-Fe-oxide (LSCF) electrodes on yttria-stabilized zirconia (YSZ) electrolyte using alternating current (AC) and direct current (DC) methods. J Electrochem Soc 168:064510
180. Zhang L, Zhu L, Virkar AV (2019) Modeling of oxygen chemical potential distribution in solid oxide electrolyzer cells. J Electrochem Soc 166:F1275
181. Lust E, Möller P, Kivi I et al (2005) Electrochemical characteristics of La0.6Sr0.4CoO3-δ, Pr0.6Sr0.4CoO3-δ and Gd0.6Sr0.4CoO3-δ on Ce0.85Sm0.15O1.925 electrolyte. J Solid State Electrochem 9:882–889. https://doi.org/10.1007/s10008-005-0040-8

182. Lust E, Möller P, Kivi I et al (2005) Optimization of the cathode composition for the intermediate-temperature SOFC. J Electrochem Soc 152:A2306–A2308
183. Nurk G, Küngas R, Kivi I et al (2007) Influence of mesoporosity of the anode on the characteristics of mediumtemperature SOFC single cells. ECS Trans 7:1609
184. Kivi I, Möller P, Kurig H et al (2008) Development of porous cathode powders for SOFC and influence of cathode structure on the oxygen electroreduction kinetics. Electrochem Commun 10:1455–1458. https://doi.org/10.1016/j.elecom.2008.07.029
185. Küngas R, Kivi I, Lust K et al (2009) Statistical method to optimize the medium temperature solid oxide fuel cell electrode materials. J Electroanal Chem 629:94–101. https://doi.org/10.1016/j.jelechem.2009.01.033
186. Lust E, Küngas R, Kivi I et al (2010) Electrochemical and gas phase parameters of cathodes for intermediate temperature solid oxide fuel cells. Electrochim Acta 55:7669–7678. https://doi.org/10.1016/j.electacta.2009.11.007
187. Küngas R, Kim J-S, Vohs JM, Gorte RJ (2011) Restructuring porous YSZ by treatment in hydrofluoric acid for use in SOFC cathodes. J Am Ceram Soc 94:2220–2224
188. Kivi I, Aruväli J, Kirsimäe K et al (2015) Kinetic response of La0.6Sr0.4CoO3-δ lattice parameters to electric potential change in porous cathode at in situ solid oxide fuel cell conditions. J Electrochem Soc 162:F354–F358. https://doi.org/10.1149/2.0821503jes
189. Kivi I, Aruväli J, Kirsimäe K et al (2017) Influence of humidified synthetic air feeding conditions on the stoichiometry of (La1-xSrx)yCoO3−δ and La0.6Sr0.4Co0.2Fe0.8O3−δ cathodes under applied potential measured by electrochemical in situ high-temperature XRD method. J Solid State Electrochem 21:361–369. https://doi.org/10.1007/s10008-016-3379-0
190. Vestli M, Lust E, Nurk G (2015) Characterization of terbium and samarium co-doped ceria films prepared using ultrasonic spray pyrolysis. J Electrochem Soc 162:F812–F820. https://doi.org/10.1149/2.0031508jes
191. Maide M, Korjus O, Vestli M et al (2016) Comparative study of BaY0.1Zr0.9O3-δ protective layers deposited to BaY0.1Ce0.9O3-δ membrane using ultrasonic spray pyrolysis and magnetron sputtering methods. J Electrochem Soc 163:F443–F447. https://doi.org/10.1149/2.0011606jes
192. Vestli M, Nurk G, Lust E (2011) Electrical properties of Tb and Sm Co-doped ceria electrolyte at different oxygen partial pressures. ECS Trans 35:1219–1224. https://doi.org/10.1149/1.3570106
193. Nurk G, Kooser K, Urpelainen S et al (2018) Near ambient pressure X-ray photoelectron — and impedance spectroscopy study of NiO — Ce0.9Gd0.1O2-δ anode reduction using a novel dual-chamber spectroelectrochemical cell. J Power Sources 378:589–596. https://doi.org/10.1016/j.jpowsour.2017.12.080
194. Nurk G, Huthwelker T, Braun A et al (2013) Redox dynamics of sulphur with Ni/GDC anode during SOFC operation at mid- and low-range temperatures: an operando S K-edge XANES study. J Power Sources 240:448–457. https://doi.org/10.1016/j.jpowsour.2013.03.187
195. Kooser K, Käämbre T, Vestli M et al (2020) Operando high-temperature near-ambient pressure X-ray photoelectron spectroscopy and impedance spectroscopy study of Ni−Ce0.9Gd0.1O2−δ solid oxide fuel cell anode. Int J Hydrog Energy 45:25286–25298. https://doi.org/10.1016/j.ijhydene.2020.06.228
196. Nenning A, Opitz AK, Rameshan C et al (2016) Ambient pressure XPS study of mixed conducting perovskite-type SOFC cathode and anode materials under well-defined electrochemical polarization. J Phys Chem C 120:1461–1471. https://doi.org/10.1021/acs.jpcc.5b08596
197. Maide M, Paiste P, Möller P et al (2019) Influence of A-and B-Site modifications of (La1-xSrx) yCr0. 5-zMn0. 5-wNiz+wO3-δ on electrochemical impedance characteristics of reversible solid oxide cell. J Electrochem Soc 166:F1148
198. Korjus O, Aruväli J, Kivi I et al (2018) Simultaneous operando characterization of crystallographic and electrochemical properties of Ni-Ce0. 9Gd0. 1O2-δ solid oxide fuel cell anode. J Electrochem Soc 165:F1043
199. Korjus O, Aruväli J, Paiste P et al (2020) Study of electrochemical and crystallographic changes during initial stabilization of La0.75Sr0.25Cr0.5Mn0.3Ni0.2O3−δ reversible solid oxide cell electrode. Fuel Cells 20:741–752. https://doi.org/10.1002/fuce.202000104
200. Korjus O, Möller P, Kooser K et al (2021) Influence of Ni concentration on electrochemical and crystallographic properties of La0.25Sr0.25Ca04Ti1−xNixO3−δ solid oxide fuel cell anode. J Power Sources 494:229739. https://doi.org/10.1016/j.jpowsour.2021.229739
201. Korjus O, Nurk G, Aruväli J et al (2019) Electrochemical-and crystallographic operando characterization of La0. 75Sr0. 25Cr0. 5Mn0. 3Ni0. 2O3-δ anode infiltrated into Sc0. 2Ce0. 01Zr0. 79O2-δ Electrolyte Scaffold. ECS Trans 91:1683
202. Tamm K, Kivi I, Anderson E et al (2012) Influence of graphite pore forming agents on the structural and electrochemical properties of porous Ni-CGO anode. J Electrochem Soc 159:F849
203. Tamm K, Küngas R, Gorte RJ, Lust E (2013) Solid oxide fuel cell anodes prepared by infiltration of strontium doped lanthanum vanadate into doped ceria electrolyte. Electrochim Acta 106:398–405. https://doi.org/10.1016/j.electacta.2013.05.127
204. Tamm K, Kivi I, Anderson E et al (2011) Optimization of solid oxide fuel cell Ni-CGO anode porosity. ECS Trans 35:1771–1779. https://doi.org/10.1149/1.3570165
205. Tamm K, Raudsepp R, Kanarbik R et al (2013) Investigation of microstructure of Sr-doped lanthanum vanadium oxide anode based on SDC electrolyte. ECS Trans 57:1185–1191. https://doi.org/10.1149/05701.1185ecst
206. Lillmaa K, Maide M, Kanarbik R et al (2016) Electrochemical characteristics and gas composition generated by $La_{0.8}Sr_{0.2}Cr_{0.5}Mn_{0.5}O_{3-\delta}$ cathode at electrolysis and co-electrolysis modes. J Electrochem Soc 163:F3190–F3196. https://doi.org/10.1149/2.0261611jes
207. Irvine JTS, Neagu D, Verbraeken MC et al (2016) Evolution of the electrochemical interface in high-temperature fuel cells and electrolysers. Nat Energy 1:15014. https://doi.org/10.1038/nenergy.2015.14
208. Lust E, Nurk G, Möller P et al (2008) Method for the preparation of a solid oxide fuel cell single cell and the named cell. Patent No. EP-2160785-B1
209. Küngas R, Kivi I, Lust E (2008) Effect of cell geometry on the electrochemical parameters of solid oxide fuel cell cathodes. J Electrochem Soc 156:B345
210. Zhao F, Virkar AV (2005) Dependence of polarization in anode-supported solid oxide fuel cells on various cell parameters. J Power Sources 141:79–95. https://doi.org/10.1016/j.jpowsour.2004.08.057
211. Kivi I, Aruväli J, Kirsimäe K et al (2013) Oxygen stoichiometry in La0.6Sr0.4CoO3−δ and La0.6Sr0.4Co0.2Fe0.8O3−δ cathodes under applied potential as a function of temperature and oxygen partial pressure, measured by electrochemical in situ high-temperature XRD method. J Electrochem Soc 160:F1022. https://doi.org/10.1149/2.072309jes
212. Maide M, Lillmaa K, Nurk G, Lust E (2017) Dependence of syngas composition on microstructure of La0.8Sr0.2Cr0.5Mn0.5O3–δ based cathode for CO2 and H2O co-electrolysis. ECS Trans 78:3275. https://doi.org/10.1149/07801.3275ecst
213. Heinsaar A, Kivi I, Möller P et al (2022) Influence of carbon dioxide and humidity on the stability of (La0. 6Sr0. 4) 0.99 Co1−xTixO3−δ Cathode. J Electrochem Soc 169:014514

214. Siinor L, Lust K, Lust E (2007) Impedance study of adsorption of iodide ions at Bi(001) electrode from the aqueous solutions with constant ionic strength. J Electroanal Chem 601:39–46. https://doi.org/10.1016/j.jelechem.2006.10.031
215. Väärtnõu M, Lust E (2022) Adsorption of iodide ions at the Bi(111) | propylene carbonate + dimethyl carbonate interface. J Electroanal Chem 920:116618. https://doi.org/10.1016/j.jelechem.2022.116618
216. Väärtnõu M, Lust E (2017) Electrical double layer and adsorption of iodide ions at the Bilethylene carbonate interface. J Solid State Electrochem 21:193–201. https://doi.org/10.1007/s10008-016-3358-5
217. Väärtnõu M, Lust E (2014) Electrical double layer and adsorption of iodide ions at the Bilgamma-butyrolactone interface. J Electroanal Chem 733:20–26
218. Väärtnõu M, Lust E (2014) Electrical double layer and adsorption of iodide ions at the Bilacetonitrile interface. J Solid State Electrochem 18:173–180. https://doi.org/10.1007/s10008-013-2253-6
219. Lust E, Lust K, Jänes A (1996) Influence of the surface structure of cadmium electrodes on the electric double layer parameters in aqueous surface-inactive electrolyte solutions. J Electroanal Chem 413:111–121
220. Väärtnõu M, Lust E (2009) Adsorption of tetraethylammonium ions on Cd(0001) single crystal plane from solutions in ethanol. J Electroanal Chem 635:99–104. https://doi.org/10.1016/j.jelechem.2009.08.012
221. Väärtnõu M, Lust E (1999) Calculation of thermodynamic and inner layer characteristics of halide ions adsorbed on bismuth single crystal planes from solutions in methanol. J Electroanal Chem 469:182–188. https://doi.org/10.1016/S0022-0728(99)00225-9
222. Lust E (2018) Zero charge potentials and electrical double layer at solid electrodes. Encyclopedia of interfacial chemistry: surface science and electrochemistry. Elsevier, Amsterdam, pp 316–344
223. Ivaništšev V, Fedorov MV (2014) Interfaces between charged surfaces and ionic liquids: insights from molecular simulations. Electrochem Soc Interface 23:65–69
224. Ivaništšev V, O'Connor S, Fedorov MV (2014) Poly(a)morphic portrait of the electrical double layer in ionic liquids. Electrochem Commun 48:61–64. https://doi.org/10.1016/j.elecom.2014.08.014
225. Coles SW, Mishin M, Perkin S et al (2017) The nanostructure of a lithium glyme solvate ionic liquid at electrified interfaces. Phys Chem Chem Phys 19:11004–11010. https://doi.org/10.1039/C7CP00837F
226. Kislenko SA, Moroz YO, Karu K et al (2018) Calculating the maximum density of the surface packing of ions in ionic liquids. Russ J Phys Chem A 92:999–1005. https://doi.org/10.1134/S0036024418050187
227. Siinor L, Siimenson C, Ivaništšev V et al (2012) Influence of cation chemical composition and structure on the double layer capacitance for Bi(111) | room temperature ionic liquid interface. J Electroanal Chem 668:30–36. https://doi.org/10.1016/j.jelechem.2012.01.005
228. Nurk G, Jänes A, Lust K, Lust E (2001) Adsorption kinetics of 2-methyl-2-butanol on bismuth single crystal planes. J Electroanal Chem 515:17–32. https://doi.org/10.1016/S0022-0728(01)00648-9
229. Jänes A, Nurk G, Lust K et al (2002) Adsorption kinetics of normal-heptanol on the bismuth single crystal planes. Russ J Electrochem 38:8–19. https://doi.org/10.1023/A:1013726109419
230. Kasuk H, Nurk G, Lust K, Lust E (2003) Adsorption kinetics of uracil on bismuth single crystal planes. J Electroanal Chem 550–551:13–31. https://doi.org/10.1016/S0022-0728(03)00140-2
231. Nurk G, Kasuk H, Lust K et al (2003) Adsorption kinetics of dodecyl sulfate anions on the bismuth (01ŧ) plane. J Electroanal Chem 553:1–19. https://doi.org/10.1016/S0022-0728(03)00200-6
232. Kasuk H, Nurk G, Lust K, Lust E (2005) Adsorption of uracil on bismuth single crystal planes. J Electroanal Chem 580:128–134. https://doi.org/10.1016/j.jelechem.2005.03.017
233. Kallip S, Grozovski V, Kasuk H, Lust E (2006) Atomic surface structure and adsorption of camphor and thiourea on Bi(111) electrode surface. ECS Trans 3:155–168
234. Grozovski V, Kasuk H, Kallip S, Lust E (2014) Adsorption of thiourea on Bi(111) electrode surface. J Electroanal Chem 712:103–112. https://doi.org/10.1016/j.jelechem.2013.11.006
235. Pikma P, Grozovski V, Kasuk H, Lust E (2014) In situ STM studies of electrochemically polished Cd(0001) electrode in aqueous electrolyte solutions. Surf Sci 628:86–91. https://doi.org/10.1016/j.susc.2014.05.009
236. Pikma P, Siinor L, Selberg S, Lust E (2015) In situ STM studies of electrochemically polished Cd(0001) electrode in 1-ethyl-3-methylimidazolium tetrafluoroborate. ECS Trans 66:41–47. https://doi.org/10.1149/06627.0041ecst
237. Pikma P, Siinor L, Oll O, Lust E (2015) Formation of 2,2′-bipyridine adlayers at Sb(111)ionic liquid + 2,2′-bipyridine solution interface. Electrochem Commun 61:61–65. https://doi.org/10.1016/j.elecom.2015.08.012
238. Kallip S, Kasuk H, Grozovski V et al (2008) Adsorption of camphor and 2,2′-bipyridine on Bi(1 1 1) electrode surface. Electrochim Acta 53:4035–4045. https://doi.org/10.1016/j.electacta.2007.10.010
239. Grozovski V, Ivaništšev V, Kasuk H et al (2014) Balance of the interfacial interactions of 4,4′-bipyridine at Bi(111) surface. Electrochim Acta 120:86–95. https://doi.org/10.1016/j.electacta.2013.12.047
240. Gorbatovski G, Oll O, Kasuk H et al (2019) In situ scanning tunneling microscopy study of bipyridine adsorption at semimetallic Sb(111) plane. Electrochem Commun 105:106500. https://doi.org/10.1016/j.elecom.2019.106500
241. Ers H, Siinor L, Siimenson C et al (2022) Order beyond a monolayer: the story of two self-assembled 4,4′-bipyridine layers on the Sb(111) | ionic liquid interface. Electrochim Acta 421:140468. https://doi.org/10.1016/j.electacta.2022.140468
242. Pikma P, Kasuk H, Oll O et al (2015) Adsorption of 4,4′−bipyridine on the Cd(0001) single crystal electrode surface. Electrochim Acta 180:965–976. https://doi.org/10.1016/j.electacta.2015.08.003
243. Romann T, Grozovski V, Lust E (2007) Formation of the bismuth thiolate compound layer on bismuth surface. Electrochem Commun 9:2507–2513. https://doi.org/10.1016/j.elecom.2007.07.029
244. Hurwitz HD (1965) Direct determination of the surface excess of specifically adsorbed ions on mercury. J Electroanal Chem 10:35–41. https://doi.org/10.1016/0022-0728(65)85013-6
245. Dutkiewicz E, Parsons R (1966) The adsorption of iodide ion from aqueous KI + KF of constant ionic strength. J Electroanal Chem 11:100–110. https://doi.org/10.1016/0022-0728(66)80069-4
246. Grahame DC, Parsons R (1961) Components of charge and potential in the inner region of the electrical double layer: aqueous potassium chloride solutions in contact with mercury at 25°. J Am Chem Soc 83:1291–1296. https://doi.org/10.1021/ja01467a009
247. Lust K, Lust E (2003) Influence of geometrical structure of the anions on the adsorption parameters at the Bi(0 0 1) electrode. J Electroanal Chem 552:129–139. https://doi.org/10.1016/S0022-0728(03)00014-7
248. Väärtnõu M, Lust E (1999) Adsorption of iodide ions on bismuth single crystal planes from solutions in methanol. Electrochim Acta 44:2437–2444. https://doi.org/10.1016/S0013-4686(98)00376-4
249. Väärtnõu M, Lust E (2001) Adsorption of iodide ions on bismuth single crystal planes from solutions in ethanol. Electrochim Acta 47:997–1005. https://doi.org/10.1016/S0013-4686(01)00798-8

250. Väärtnõu M, Lust E (2012) Electrical double layer and adsorption of iodide ions at the Bilpropylene carbonate interface. J Electroanal Chem 686:63–68. https://doi.org/10.1016/j.jelechem.2012.09.019
251. Väärtnõu M, Pärsimägi P, Lust E (1996) Adsorption of Cl- and Br- ions on the (111) plane of a bismuth single crystal from solutions in 2-propanol. J Electroanal Chem 407:227–231. https://doi.org/10.1016/0022-0728(95)04492-2
252. Väärtnõu M, Lust E (2008) Adsorption of iodide ions on the Cd(0001) single crystal plane in ethanol. J Electroanal Chem 614:1–7. https://doi.org/10.1016/j.jelechem.2007.10.025
253. Väärtnõu M, Nerut J, Lust E (2011) Adsorption of iodide ions on the Cd(0001) single crystal plane in methanol. J Solid State Electrochem 15:1893–1899. https://doi.org/10.1007/s10008-010-1209-3
254. Kurig H, Vestli M, Tõnurist K et al (2012) Influence of room temperature ionic liquid anion chemical composition and electrical charge delocalization on the supercapacitor properties. J Electrochem Soc 159:A944–A951. https://doi.org/10.1149/2.022207jes
255. Väärtnõu M, Pärsimägi P, Lust E (1995) Adsorption of Cl− and Br− ions on the (001) plane of a bismuth single crystal from solutions in 2-propanol. J Electroanal Chem 385:115–119. https://doi.org/10.1016/0022-0728(94)03755-R
256. Kolotyrkin YM, Alexeyev YV, Popov YA (1975) Double layer model taking into account the specific adsorption of ions: application to the process of hydrogen adsorption on lead in the presence of iodide ion. J Electroanal Chem Interfacial Electrochem 62:135–149. https://doi.org/10.1016/0022-0728(75)80032-5
257. Damaskin BB (1977) Model of the dense part of the double layer in the absence of specific adsorption. J Electroanal Chem Interfacial Electrochem 75:359–370. https://doi.org/10.1016/S0022-0728(77)80094-6
258. Palm UV, Damaskin BB (1977) Structure of the electrical double layer and adsorption phenomena on a bismuth electrode. Itogi Nauki Tekhniki 12:99–143
259. Schmickler W, Guidelli R (2014) The partial charge transfer. Electrochim Acta 127:489–505. https://doi.org/10.1016/j.electacta.2014.02.057
260. Valette G, Hamelin A, Parsons R (1978) Specific adsorption on silver single crystals in aqueous solutions. Z Für Phys Chem 113:71–89. https://doi.org/10.1524/zpch.1978.113.1.071
261. Bange K, Straehler B, Sass JK, Parsons R (1987) The interaction of Br with Ag (110): comparison of electrochemical and gas-phase adsorption measurements. J Electroanal Chem Interfacial Electrochem 229:87–98. https://doi.org/10.1016/0022-0728(87)85132-X
262. Schmickler W, Guidelli R (1987) Ionic adsorption and the surface dipole potential. J Electroanal Chem Interfacial Electrochem 235:387–392. https://doi.org/10.1016/0022-0728(87)85223-3
263. Nazmutdinov RR, Spohr E (1994) Partial charge transfer of the iodide ion near a water/metal interface. J Phys Chem 98:5956–5961. https://doi.org/10.1021/j100074a023
264. Shi Z, Lipkowski J (1996) Chloride adsorption at the Au(111) electrode surface. J Electroanal Chem 403:225–239. https://doi.org/10.1016/0022-0728(95)04313-6
265. de Levie R (2004) The electrosorption valency and partial charge transfer. J Electroanal Chem 562:273–276. https://doi.org/10.1016/j.jelechem.2003.08.027
266. Vorotyntsev MA (1988) Specific adsorption from electrolyte solutions. Itogi Nauki i Tekhniki Ser Elektrokhimiya 26:3–39
267. Thomberg T, Nerut J, Lust E (2004) The kinetics of electroreduction of peroxodisulfate anion on electrochemically polished Cd(0 0 0 1) plane. Electrochim Acta 49:1271–1279. https://doi.org/10.1016/j.electacta.2003.09.049
268. Thomberg T (2000) Electroreduction of peroxodisulfate anion at a Cd(0001) single-crystal plane electrode. J Electroanal Chem 485:89–93. https://doi.org/10.1016/S0022-0728(00)00089-9
269. Jäger R, Härk E, Möller P et al (2004) The kinetics of electroreduction of hexaamminecobalt (III) cation on Bi planes in aqueous HClO4 solutions. J Electroanal Chem 566:217–226. https://doi.org/10.1016/j.jelechem.2003.11.030
270. Thomberg T, Nerut J, Lust E (2006) Impedance spectroscopy data for S2O82-anions electroreduction kinetics at Cd(0 0 0 1) plane electrode. J Electroanal Chem 586:237–246. https://doi.org/10.1016/j.jelechem.2005.10.001
271. Thomberg T, Nerut J, Lust K et al (2008) Impedance spectroscopy data for S2O82- anion electroreduction at Bi (111) plane. Electrochim Acta 53:3337–3349
272. Härk E, Lust E (2006) Electroreduction of hexaamminecobalt (III) cation on Bi (hkl) electrodes from weakly acidified LiClO4 solutions. J Electrochem Soc 153:E104
273. Härk E, Lust K, Jänes A, Lust E (2009) Electrochemical impedance study of hydrogen evolution on Bi(001) electrode in the HClO4 aqueous solutions. J Solid State Electrochem 13:745–754
274. Thomberg T, Nerut J, Jäger R et al (2005) The kinetics of electroreduction of peroxodisulfate ions on single crystal cadmium and bismuth electrodes. J Electroanal Chem 582:130–143. https://doi.org/10.1016/j.jelechem.2005.01.004
275. Härk E, Jäger R, Lust K et al (2012) The kinetics of electroreduction of europium(III) cations at bismuth single-crystal electrode. J Solid State Electrochem 16:921–926. https://doi.org/10.1007/s10008-011-1443-3
276. Nerut J, Möller P, Lust E (2004) Electroreduction of hexacyanoferrate(III) anions on electrochemically polished Cd(0 0 0 1) plane. Electrochim Acta 49:1597–1604. https://doi.org/10.1016/j.electacta.2003.11.021
277. Frumkin AN, Nikolaeva-Fedorovich NV, Berezina NP, Keis KhE (1975) The electroreduction of the S2O82− anion. J Electroanal Chem Interfacial Electrochem 58:189–201. https://doi.org/10.1016/S0022-0728(75)80352-4
278. Samec Z, Bittner AM, Doblhofer K (1997) Origin of electrocatalysis in the reduction of peroxodisulfate on gold electrodes. J Electroanal Chem 432:205–214. https://doi.org/10.1016/S0022-0728(97)00204-0
279. Samec Z, Krischer K, Doblhofer K (2001) Reduction of peroxodisulfate on gold(111) covered by surface oxides: inhibition and coupling between two oxide reduction processes. J Electroanal Chem 499:129–135. https://doi.org/10.1016/S0022-0728(00)00499-X
280. Fawcett WR, Fedurco M, Kováčová Z (1994) Double-layer effects associated with surface reconstruction on a Au (100) electrode. J Electrochem Soc 141:L30. https://doi.org/10.1149/1.2054828
281. Hromadová M, Fawcett WR (2000) Studies of double-layer effects at single-crystal gold electrodes. 1. The reduction kinetics of hexaamminecobalt(III) ion in aqueous solutions. J Phys Chem A 104:4356–4363. https://doi.org/10.1021/jp994136z
282. Nazmutdinov RR, Pobelov IV, Tsirlina GA, Petrii OA (2000) Nature of the 'current pit' in concentrated solutions: part I. Microscopic modelling of the interaction of Pt(II) aquachlorocomplexes with a mercury electrode. J Electroanal Chem 491:126–138. https://doi.org/10.1016/S0022-0728(00)00250-3
283. Tsirlina GA, Kharkats YuI, Nazmutdinov RR, Petrii OA (1999) Effect of the reagent orientation at the electrode-solution interface on the electrochemical kinetics. Russ J Electrochem 35:19–28
284. Ers H, Nerut J, Lust E, Pikma P (2021) Long-term stability of Cd (0001) single crystall ionic liquid interface—the effect of I-addition. J Electroanal Chem 903:115826. https://doi.org/10.1016/j.jelechem.2021.115826
285. Anderson E, Grozovski V, Siinor L et al (2015) Comparative in situ STM, cyclic voltammetry and impedance spectroscopy study of Bi(111) | 1-ethyl-3-methylimidazolium

tetrafluoroborate interface. J Electroanal Chem 758:201–208. https://doi.org/10.1016/j.jelechem.2015.08.036
286. Siimenson C, Siinor L, Lust K, Lust E (2015) Electrochemical characterization of iodide ions adsorption kinetics at Bi(111) electrode from three-component ionic liquids mixtures. ECS Electrochem Lett 4:H62–H65. https://doi.org/10.1149/2.0011512eel
287. Siimenson C, Siinor L, Lust K, Lust E (2014) The electrochemical characteristics of the mixture of 1-ethyl-3-methylimidazolium tetrafluoroborate and 1-ethyl-3-methylimidazolium iodide. J Electroanal Chem 730:59–64. https://doi.org/10.1016/j.jelechem.2014.07.035
288. Ferrari AC, Robertson J (2000) Interpretation of Raman spectra of disordered and amorphous carbon. Phys Rev B - Condens Matter Mater Phys 61:14095–14107. https://doi.org/10.1103/PhysRevB.61.14095
289. Ferrari AC (2007) Raman spectroscopy of graphene and graphite: disorder, electron–phonon coupling, doping and nonadiabatic effects. Solid State Commun 143:47–57. https://doi.org/10.1016/j.ssc.2007.03.052
290. Lust E, Jänes A, Arulepp M (2004) Influence of electrolyte characteristics on the electrochemical parameters of electrical double layer capacitors. J Solid State Electrochem 8:488–496. https://doi.org/10.1007/s10008-003-0458-9
291. Lust R, Nerut J, Kasak K, Mander Ü (2020) Enhancing nitrate removal from waters with low organic carbon concentration using a bioelectrochemical system—a pilot-scale study. Water. https://doi.org/10.3390/w12020516
292. Kawashima Y, Katagiri G (1995) Fundamentals, overtones, and combinations in the Raman spectrum of graphite. Phys Rev B 52:10053–10059. https://doi.org/10.1103/PhysRevB.52.10053
293. Jagiello J, Thommes M (2004) Comparison of DFT characterization methods based on N2, Ar, CO2, and H2 adsorption applied to carbons with various pore size distributions. Carbon 42:1227–1232. https://doi.org/10.1016/j.carbon.2004.01.022
294. Jagiello J, Ania C, Parra JB, Cook C (2015) Dual gas analysis of microporous carbons using 2D-NLDFT heterogeneous surface model and combined adsorption data of N2 and CO2. Carbon 91:330–337. https://doi.org/10.1016/j.carbon.2015.05.004
295. Jagiello J, Olivier JP (2013) 2D-NLDFT adsorption models for carbon slit-shaped pores with surface energetical heterogeneity and geometrical corrugation. Carbon 55:70–80. https://doi.org/10.1016/j.carbon.2012.12.011
296. Tallo I, Thomberg T, Kurig H et al (2013) Supercapacitors based on carbide-derived carbons synthesised using HCl and Cl2 as reactants. J Solid State Electrochem 17:19–28. https://doi.org/10.1007/s10008-012-1850-0
297. Sadezky A, Muckenhuber H, Grothe H et al (2005) Raman microspectroscopy of soot and related carbonaceous materials: spectral analysis and structural information. Carbon 43:1731–1742. https://doi.org/10.1016/j.carbon.2005.02.018
298. Ribeiro-Soares J, Oliveros ME, Garin C et al (2015) Structural analysis of polycrystalline graphene systems by Raman spectroscopy. Carbon 95:646–652. https://doi.org/10.1016/j.carbon.2015.08.020
299. Thomberg T, Tooming T, Romann T et al (2013) High power density supercapacitors based on the carbon dioxide activated D-glucose derived carbon electrodes and acetonitrile electrolyte. J Electrochem Soc 160:A1834–A1841. https://doi.org/10.1149/2.091310jes
300. Tooming T, Thomberg T, Kurig H et al (2015) High power density supercapacitors based on the carbon dioxide activated d-glucose derived carbon electrodes and 1-ethyl-3-methylimidazolium tetrafluoroborate ionic liquid. J Power Sources 280:667–677. https://doi.org/10.1016/j.jpowsour.2015.01.157
301. Härmas M, Thomberg T, Romann T et al (2017) Carbon for energy storage derived from granulated white sugar by hydrothermal carbonization and subsequent zinc chloride activation. J Electrochem Soc 164:A1866–A1872. https://doi.org/10.1149/2.0681709jes
302. Härmas M, Palm R, Thomberg T et al (2020) Hydrothermal and peat-derived carbons as electrode materials for high-efficient electrical double-layer capacitors. J Appl Electrochem 50:15–32. https://doi.org/10.1007/s10800-019-01364-5
303. Adamson A, Väli R, Paalo M et al (2020) Peat-derived hard carbon electrodes with superior capacity for sodium-ion batteries. RSC Adv 10:20145–20154. https://doi.org/10.1039/D0RA03212C
304. Zhao J, Gorbatovski G, Oll O et al (2019) Effect of alkali and halide ion doping on the energy storage characteristics of ionic liquid based supercapacitors. Electrochim Acta 319:82–87. https://doi.org/10.1016/j.electacta.2019.06.176
305. Härmas M, Thomberg T, Kurig H et al (2016) Microporous–mesoporous carbons for energy storage synthesized by activation of carbonaceous material by zinc chloride, potassium hydroxide or mixture of them. J Power Sources 326:624–634. https://doi.org/10.1016/j.jpowsour.2016.04.038
306. Pohl M, Tallo I, Jänes A et al (2018) Increasing the stability of very high potential electrical double layer capacitors by operando passivation. J Power Sources 402:53–61. https://doi.org/10.1016/j.jpowsour.2018.09.018
307. Jänes A, Thomberg T, Eskusson J, Lust E (2013) Fluoroethylene carbonate as co-solvent for propylene carbonate based electrical double layer capacitors. J Electrochem Soc 160:A1025. https://doi.org/10.1149/2.016308jes
308. Jänes A, Eskusson J, Thomberg T, Lust E (2014) Electrochemical double layer capacitors based on propylene carbonate solution operating from- 45 °C to 100 °C. J Electrochem Soc 161:A712–A717
309. Gogotsi Y, Nikitin A, Ye H et al (2003) Nanoporous carbide-derived carbon with tunable pore size. Nat Mater 2:591–594. https://doi.org/10.1038/nmat957
310. Dash RK, Nikitin A, Gogotsi Y (2004) Microporous carbon derived from boron carbide. Microporous Mesoporous Mater 72:203–208. https://doi.org/10.1016/j.micromeso.2004.05.001
311. Dash RK, Yushin G, Gogotsi Y (2005) Synthesis, structure and porosity analysis of microporous and mesoporous carbon derived from zirconium carbide. Microporous Mesoporous Mater 86:50–57. https://doi.org/10.1016/j.micromeso.2005.05.047
312. Yushin G, Dash R, Jagiello J et al (2006) Carbide-derived carbons: effect of pore size on hydrogen uptake and heat of adsorption. Adv Funct Mater 16:2288–2293. https://doi.org/10.1002/adfm.200500830
313. Chmiola J, Largeot C, Taberna P-L et al (2008) Desolvation of ions in subnanometer pores and its effect on capacitance and double-layer theory. Angew Chem Int Ed 47:3392–3395. https://doi.org/10.1002/anie.200704894
314. Simon P, Gogotsi Y (2008) Materials for electrochemical capacitors. Nat Mater 7:845–854. https://doi.org/10.1038/nmat2297
315. Huang P, Lethien C, Pinaud S et al (2016) On-chip and free-standing elastic carbon films for micro-supercapacitors. Science 351:691–695. https://doi.org/10.1126/science.aad3345
316. Naguib M, Barsoum MW, Gogotsi Y (2021) Ten years of progress in the synthesis and development of MXenes. Adv Mater 33:2103393. https://doi.org/10.1002/adma.202103393
317. Chmiola J, Largeot C, Taberna PL et al (2010) Monolithic carbide-derived carbon films for micro-supercapacitors. Science 328:480–483. https://doi.org/10.1126/science.1184126
318. Palm R, Kurig H, Tonurist K et al (2013) Influence of different organic solvent additives on 1-ethyl-3-methylimidazolium tetrafluoroborate electrolyte based electrical double layer capacitors. J Electrochem Soc 160:A1741

319. Palm R, Kurig H, Tonurist K et al (2012) Electrical double layer capacitors based on 1-ethyl-3-methylimidazolium tetrafluoroborate with small addition of acetonitrile. Electrochim Acta 85:139–144. https://doi.org/10.1016/j.electacta.2012.08.030
320. Kruusma J, Tõnisoo A, Pärna R et al (2014) In situ XPS studies of electrochemically positively polarized molybdenum carbide derived carbon double layer capacitor electrode. J Electrochem Soc 161:A1266–A1277. https://doi.org/10.1149/2.0641409jes
321. Romann T, Lust E, Oll O (2016) Method of forming a dielectric through electrodeposition on an electrode for a capacitor
322. Bouaziz N, Ben Manaa M, Aouaini F, Ben Lamine A (2019) Investigation of hydrogen adsorption on zeolites A, X and Y using statistical physics formalism. Mater Chem Phys 225:111–121. https://doi.org/10.1016/j.matchemphys.2018.12.024
323. Palm R, Kurig H, Aruväli J, Lust E (2018) NaAlH4/microporous carbon composite materials for reversible hydrogen storage. Microporous Mesoporous Mater 264:8–12. https://doi.org/10.1016/j.micromeso.2017.12.027
324. Härk E, Jäger R, Tallo I et al (2017) Influence of chemical composition and amount of intermixed ionomer in the catalyst on the oxygen reduction reaction characteristics. J Solid State Electrochem. https://doi.org/10.1007/s10008-017-3521-7
325. Jäger R, Härk E, Kasatkin P et al (2017) Carbide derived carbon supported Pt nanoparticles with optimum size and amount for efficient oxygen reduction reaction kinetics. J Electrochem Soc 164:F448
326. Kasatkin PE, Härk E, Jäger R, Lust E (2015) Oxygen reduction reaction in alkaline solution: influence of catalyst loading and carbon support characteristics. ECS Trans 64:115–123. https://doi.org/10.1149/06445.0115ecst
327. Koutecky J, Levich V (1958) The use of a rotating disk electrode in the studies of electrochemical kinetics and electrolytic processes. Zh Fiz Khim 32:1565–1575
328. Paulus UA, Schmidt TJ, Gasteiger HA, Behm RJ (2001) Oxygen reduction on a high-surface area Pt/Vulcan carbon catalyst: a thin-film rotating ring-disk electrode study. J Electroanal Chem 495:134–145. https://doi.org/10.1016/S0022-0728(00)00407-1
329. Bard AJ, Faulkner LR (2001) Electrochemical methods: fundamentals and applications. Wiley, New York
330. Sharma S, Pollet BG (2012) Support materials for PEMFC and DMFC electrocatalysts—a review. J Power Sources 208:96–119. https://doi.org/10.1016/j.jpowsour.2012.02.011
331. Gara M, Compton RG (2011) Activity of carbon electrodes towards oxygen reduction in acid: a comparative study. New J Chem 35:2647–2652. https://doi.org/10.1039/C1NJ20612E
332. Laanemäe J, Jäger R, Teppor P et al (2022) (Digital) Oxygen reduction reaction on waste tire derived carbon material and synthesized non-platinum group metal catalysts in alkaline solution. ECS Trans 108:39
333. Härk E, Jäger R, Tallo I et al (2015) Different carbide derived nanoporous carbon supports and electroreduction of oxygen. ECS Trans 66:69–80. https://doi.org/10.1149/06624.0069ecst
334. Härk E, Nerut J, Vaarmets K et al (2013) Electrochemical impedance characteristics and electroreduction of oxygen at tungsten carbide derived micromesoporous carbon electrodes. J Electroanal Chem 689:176–184. https://doi.org/10.1016/j.jelechem.2012.09.039
335. Nguyen HQV, Nerut J, Kasuk H et al (2022) Oxygen reduction reaction on chromium carbide-derived carbons. Russ J Electrochem 58:781–797. https://doi.org/10.1134/S1023193522090130
336. Lust E, Nurk G, Möller P et al (2003) Electrochemical impedance characteristics of some medium temperature semicells for SOFC. ECS Proc 2003:1176
337. Möller P, Kanarbik R, Kivi I et al (2013) Influence of microstructure on the electrochemical behavior of LSC cathodes for intermediate temperature SOFC. J Electrochem Soc 160:F1245. https://doi.org/10.1149/2.037311jes
338. Lust E, Nurk G, Kivi I et al (2008) Influence of cathode porosity on the characteristics of medium-temperature SOFC single cells. ECS Trans 12:293
339. Kanarbik R, Möller P, Kivi I et al (2011) Development of purification methods of rare earth compounds for preparation of more cost effective solid oxide fuel cell cathodes. ECS Trans 35:2227. https://doi.org/10.1149/1.3570217
340. Gross MD, Vohs JM, Gorte RJ (2007) Recent progress in SOFC anodes for direct utilization of hydrocarbons. J Mater Chem 17:3071–3077. https://doi.org/10.1039/B702633A
341. Tao S, Irvine JTS (2003) A redox-stable efficient anode for solid-oxide fuel cells. Nat Mater 2:320–323. https://doi.org/10.1038/nmat871
342. Park J-S, Hasson ID, Gross MD et al (2011) A high-performance solid oxide fuel cell anode based on lanthanum strontium vanadate. J Power Sources 196:7488–7494. https://doi.org/10.1016/j.jpowsour.2011.05.028
343. Nurk G, Vestli M, Möller P et al (2015) Mobility of Sr in gadolinia doped ceria barrier layers prepared using spray pyrolysis, pulsed laser deposition and magnetron sputtering methods. J Electrochem Soc 163:F88–F96. https://doi.org/10.1149/2.0531602jes

Authors and Affiliations

Piret Pikma[1] · Heigo Ers[1] · Liis Siinor[1] · Jinfeng Zhao[1] · Ove Oll[1] · Tavo Romann[1] · Vitali Grozovski[1] · Carolin Siimenson[1] · Mart Väärtnõu[1] · Maarja Paalo[1] · Riinu Härmas[1] · Karmen Lust[1] · Thomas Thomberg[1] · Alar Jänes[1] · Jaak Nerut[1] · Rutha Jäger[1] · Peeter Valk[1] · Indrek Kivi[1] · Martin Maide[1] · Priit Möller[1] · Rait Kanarbik[1] · Gunnar Nurk[1] · Enn Lust[1]

✉ Enn Lust
enn.lust@ut.ee

[1] Institute of Chemistry, University of Tartu, Ravila 14A, Tartu 50411, Estonia